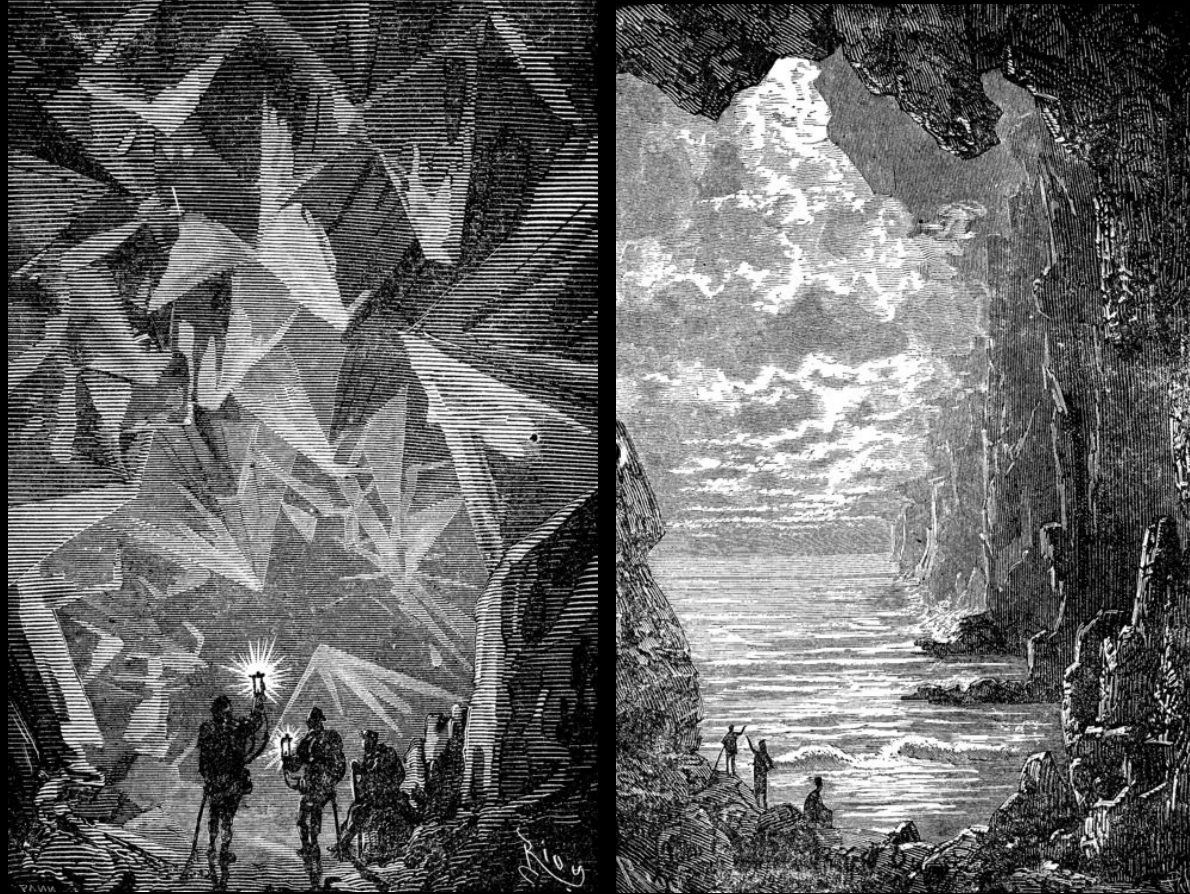


Mineral Physics 6

# Effects of Water



Mainak Mookherjee

Florida State University

07-19-2018



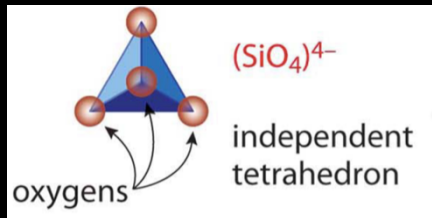
Cooperative Institute for  
Dynamic Earth Research



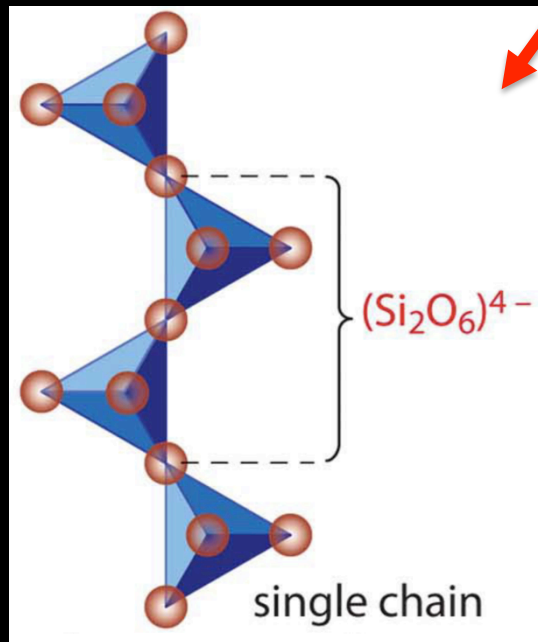
# Water & the Solid Earth

- Why bother?
  - influence in melting processes
    - (*Chemical differentiation/heterogeneity*)
  - Does water affect elastic property
    - Can we use it for mapping mantle hydration (?)
  - Does water (hydrogen) affect transport property?
- How is water transported to deep Earth?
  - Subduction zones- *hydrous minerals*
- Where is water stored in the deep Earth?
  - Bulk mantle- *nominally anhydrous minerals*

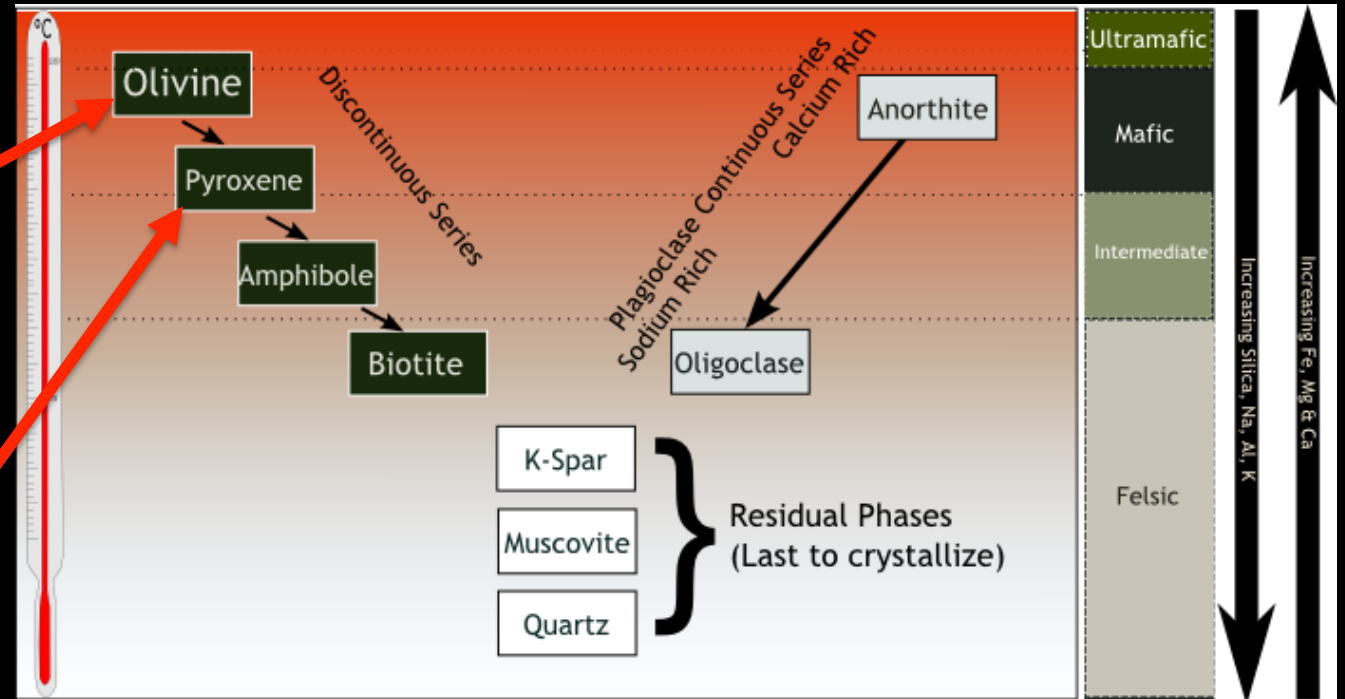
# Hydrous & Nominally anhydrous minerals



e.g.,  $\text{Mg}_2\text{SiO}_4$



e.g.,  $\text{Mg}_2\text{Si}_2\text{O}_6$  or  $\text{MgSiO}_3$  (enstatite)  
 $(\text{Ca,Mg})\text{Si}_2\text{O}_6$

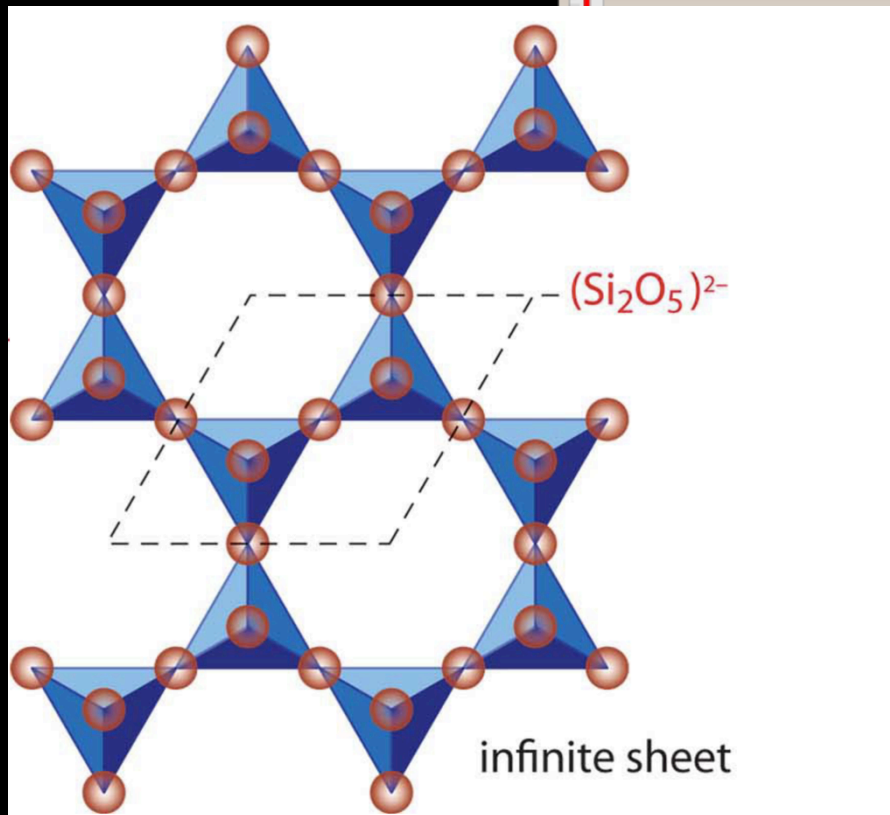
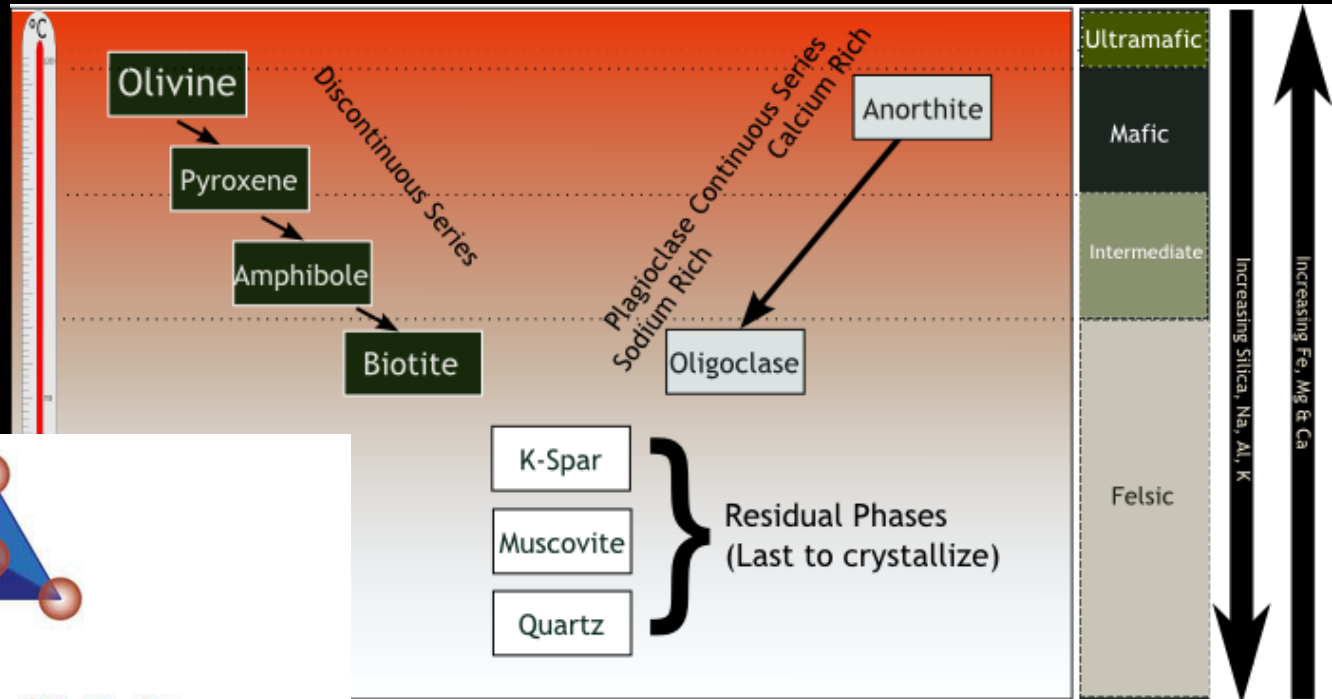


Bowen's Reaction series

## Nominally anhydrous phases (NAMs)

Hydrogen occur as defects  
hence concentrations vary  
between ppm to few wt %  
Stable at normal mantle  
geothermal gradients

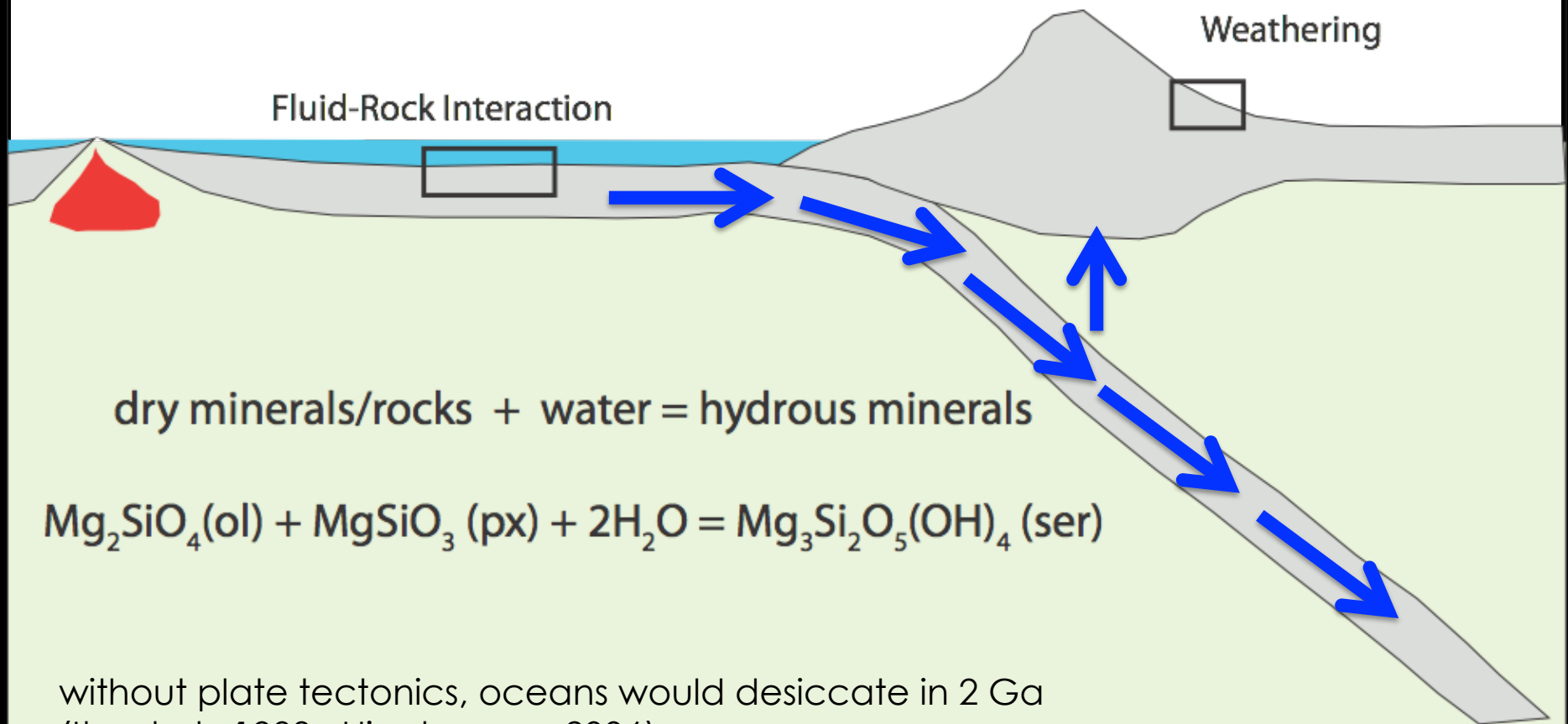
# Hydrous & Nominally anhydrous minerals



## Bowen's Reaction series

e.g., tri-octahedral T-O:  
 Serpentine  $(\text{Mg}_3)^{6+} [\text{Si}_2\text{O}_5]^{2-} (\text{OH})_4$   
 tri-octahedral T-O-T:  
 Talc  $[\text{Si}_2\text{O}_5]^{2-} (\text{Mg}_3)^{6+} [\text{Si}_2\text{O}_5]^{2-} (\text{OH})_2$   
 tri-octahedral T-O-T-I:  
 K- $[\text{Si,AlO}_5]^{3-} (\text{Mg}_3)^{6+} [\text{Si}_2\text{O}_5]^{2-} (\text{OH})_2$

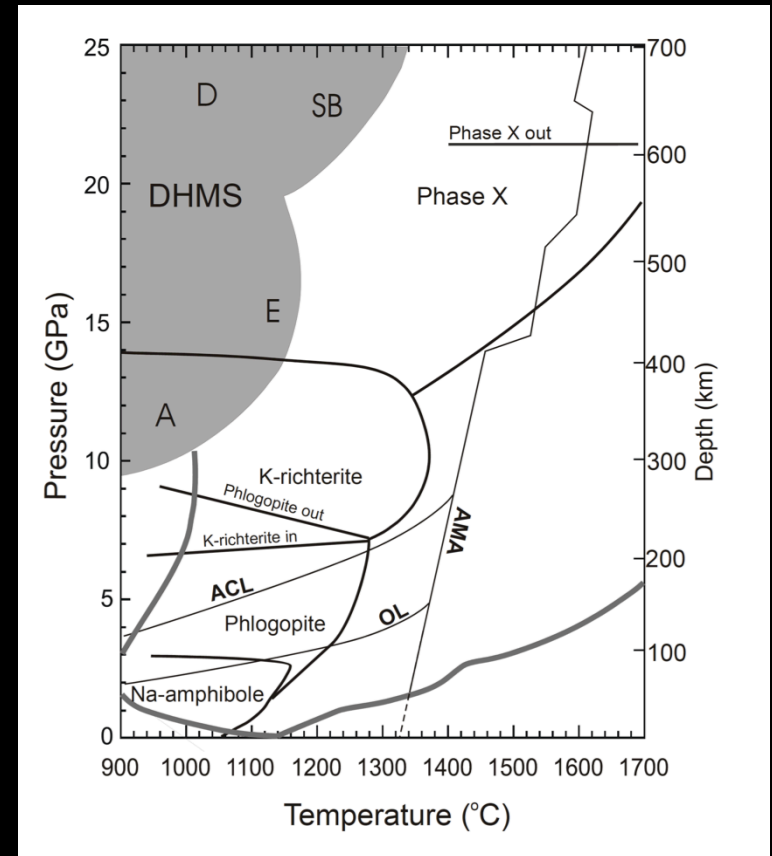
# Hydrous & Nominally anhydrous minerals



without plate tectonics, oceans would desiccate in 2 Ga  
(Ito et al., 1983 ; Hirschmann, 2006)

# Hydrous Phases: Transporter of water

- Several wt % H<sub>2</sub>O
- Hydrogen atoms are in distinct crystallographic sites
- Limited thermal stability  
(Frost, 2006; Kawamoto, 2006; Smyth, 2006)
- Low Pressures:
  - layered crystal structures ( e.g., micas)
  - extreme elastic anisotropy  
( e.g., Bezacier et al., 2010; Mookherjee & Stixrude, 2009)
  - enhanced electrical conductivity on dehydration  
(e.g., Manthilake et al., 2015; 2016)
- High Pressures:
  - denser hydrous phase, Si in six-fold coordination
  - thermodynamically stable in colder slab
  - high-temperature stability (alumina content?)



Frost 2006

AMA: Av. Mantle Adiabats

OL: Oceanic Lithosphere

ACL: Archean Cratonic Lithosphere

# Hydrous Phases: Transporter of water

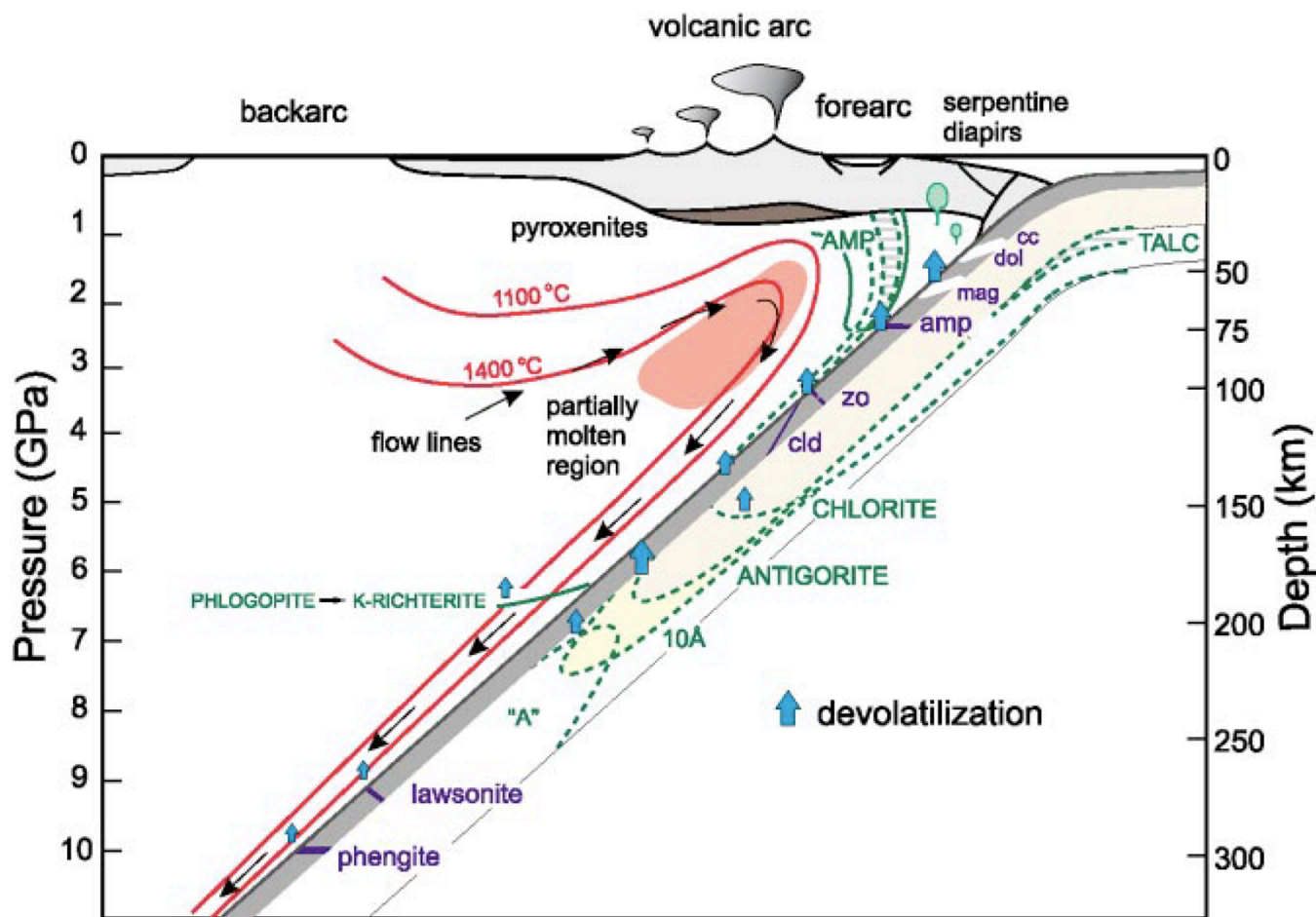


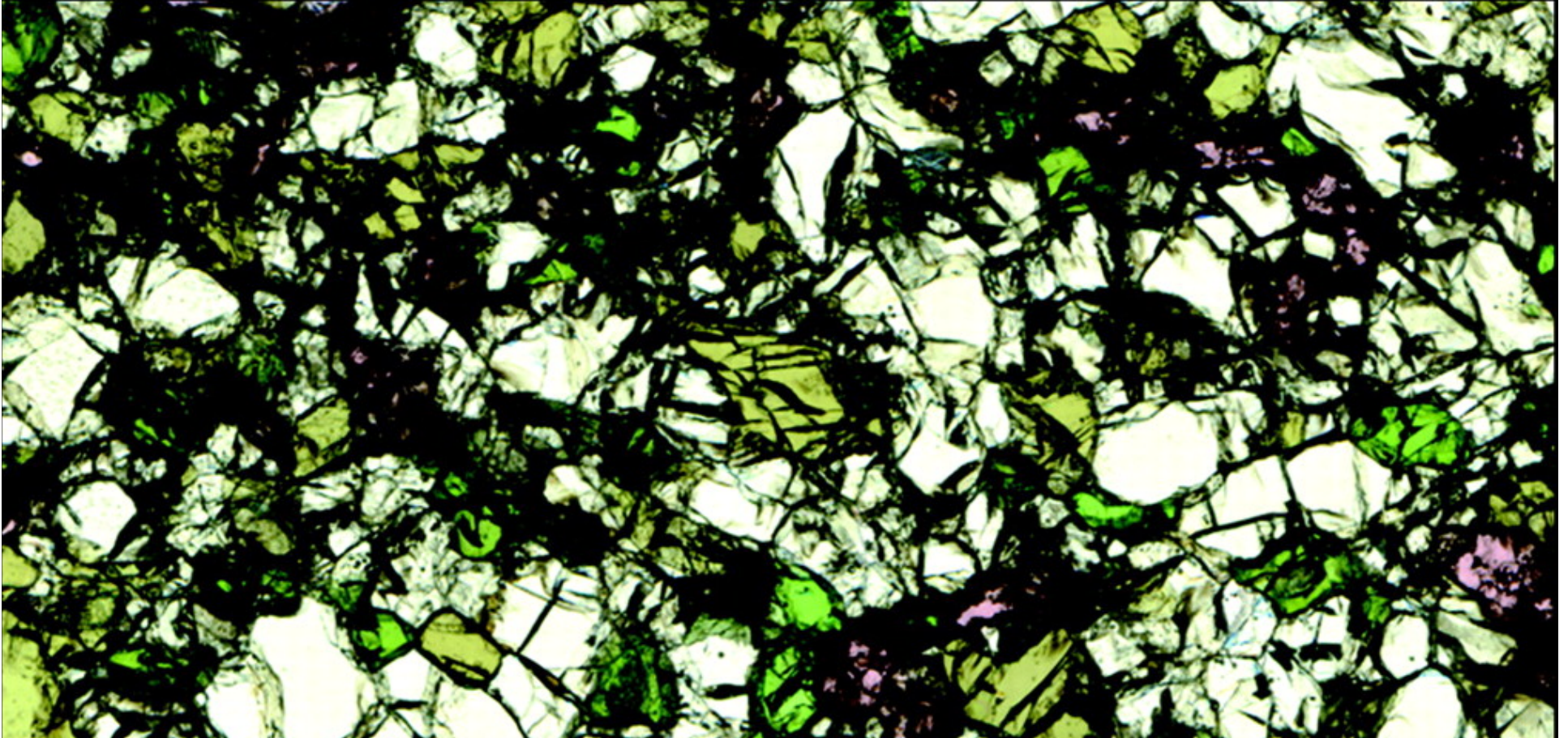
**Figure 1** Schematic arrangements of major processes governing subduction zone dynamics. Mineral labels represent the potential stability fields of volatile-bearing phases. The location of partially molten region is constrained by seismic tomography (Zhao 2000). Modified from Schmidt & Poli 1998.

*Poli & Schmidt 2002*

# Nominally Anhydrous Minerals

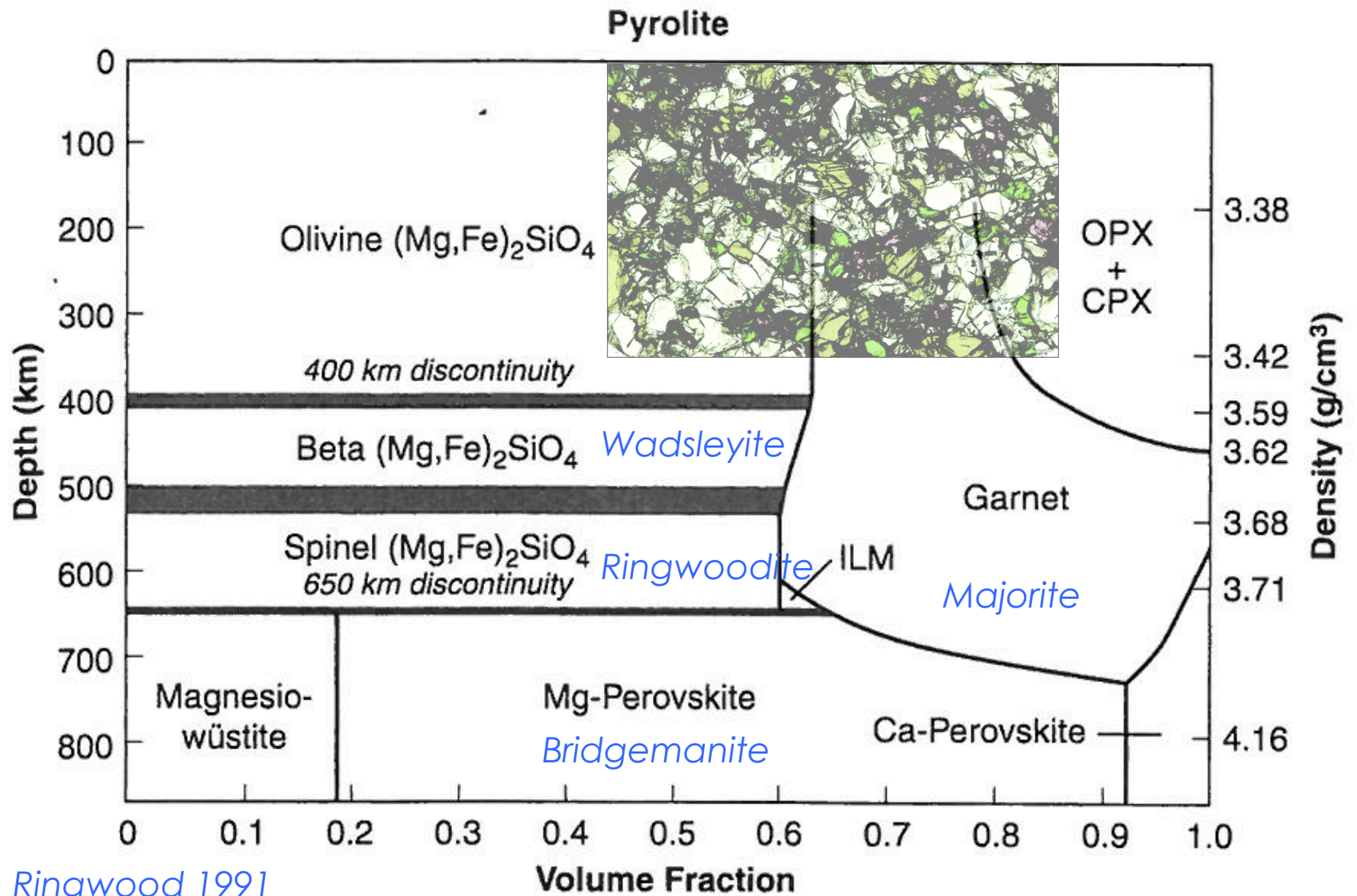
1. Natural Observations
2. Thermodynamic Model
3. Water Solubility Experiments
4. Physical Properties

# Peridotite-Mineralogy



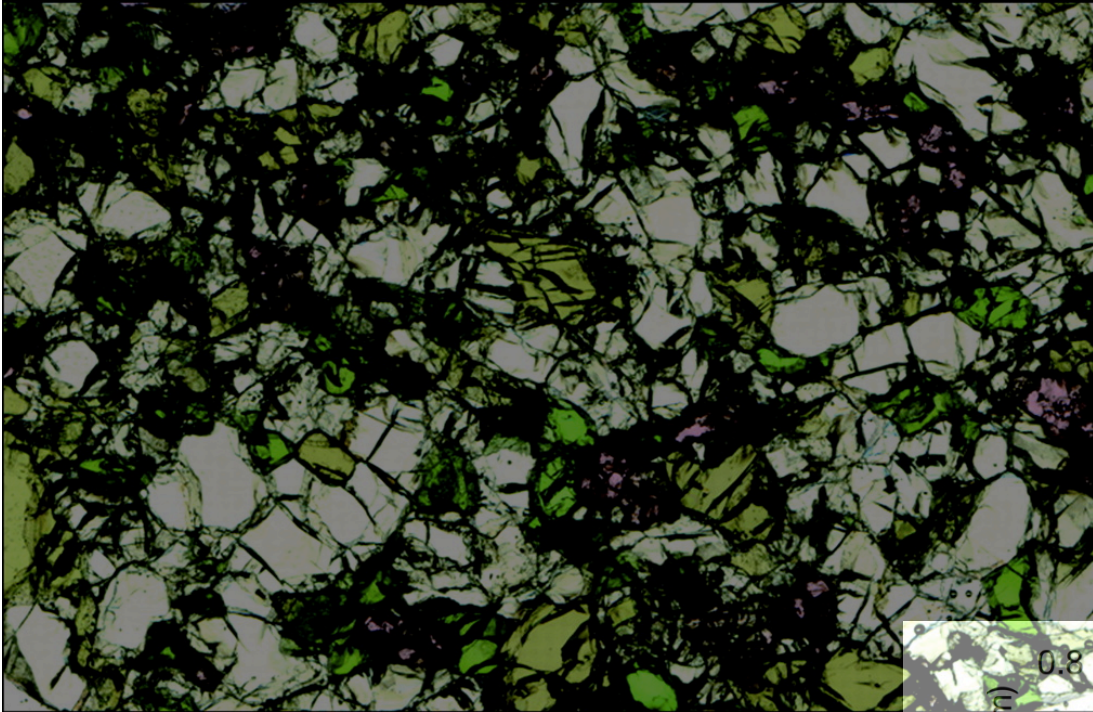
Pali-Aike garnet-herzolite xenolith derived from Earth's uppermost mantle. Transmitted light photomicrograph with mineral assemblage: olivine (transparent-pale green), diopside (bright green), orthopyroxene (brown-green), and garnet (pink). Horizontal field of view is 20 mm.  
*Demouchy et al., 2006*

# Mineralogy of the upper mantle



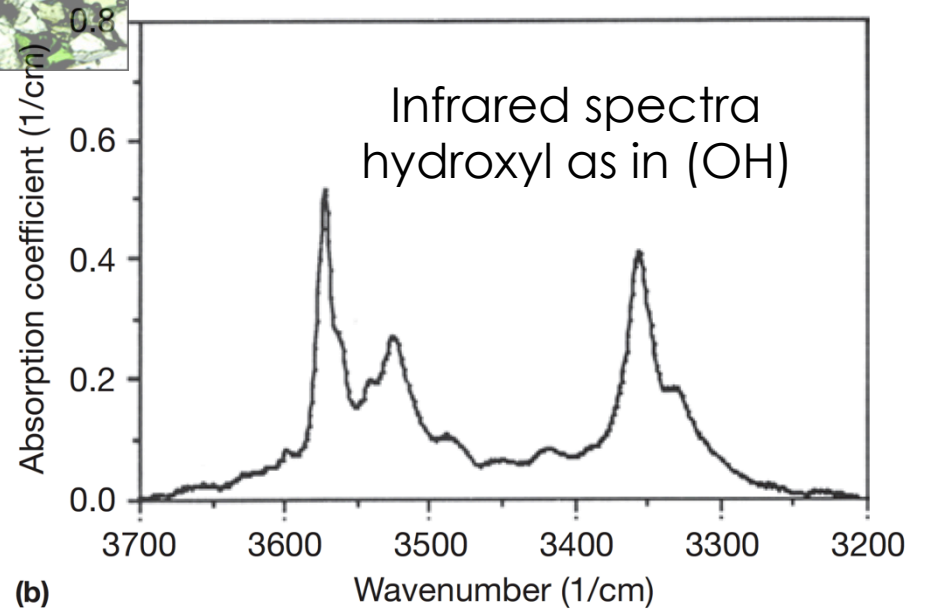
Ringwood 1991

# Nominally Anhydrous Mineral- Olivine

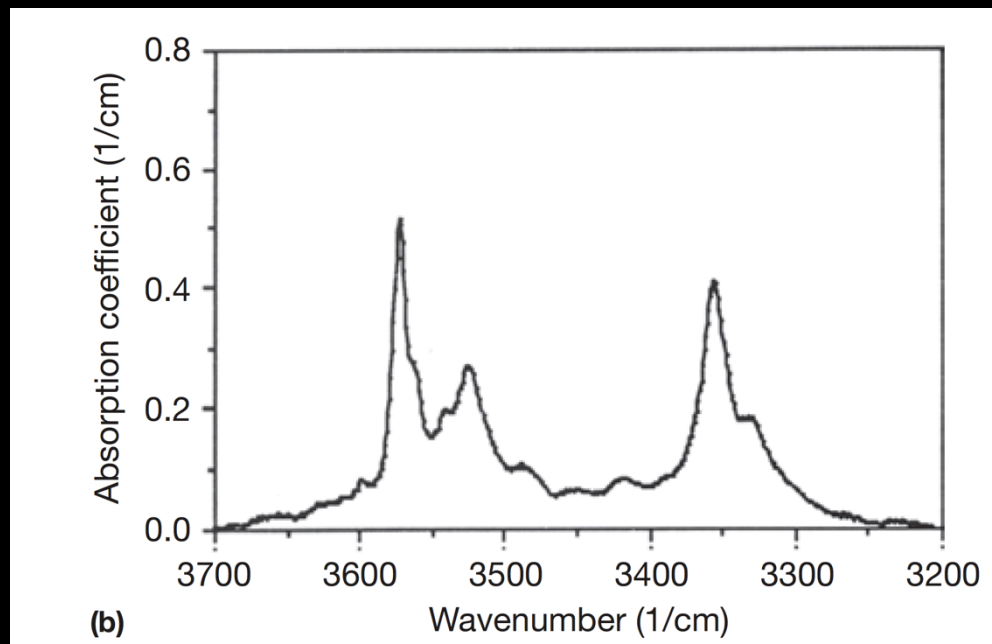
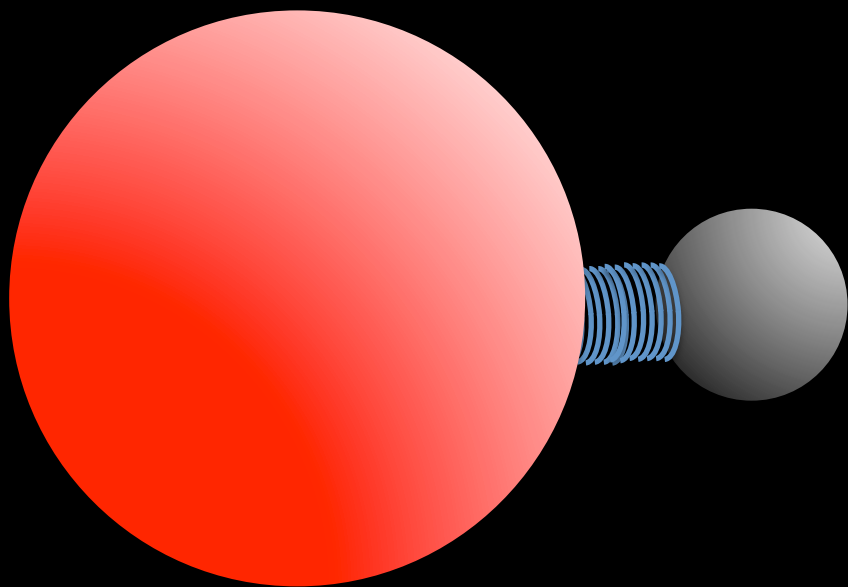


*stoichiometry~*  
 $(\text{Mg,Fe})_2\text{SiO}_4$

*No (OH) in stoichiometry~*  
 $(\text{Mg,Fe})_2\text{SiO}_4$



# Infrared Spectra and hydroxyl (OH) stretch



$$\bar{\nu} = \frac{1}{2\pi c} \sqrt{\frac{k}{\mu}}$$

$$\bar{\nu}$$

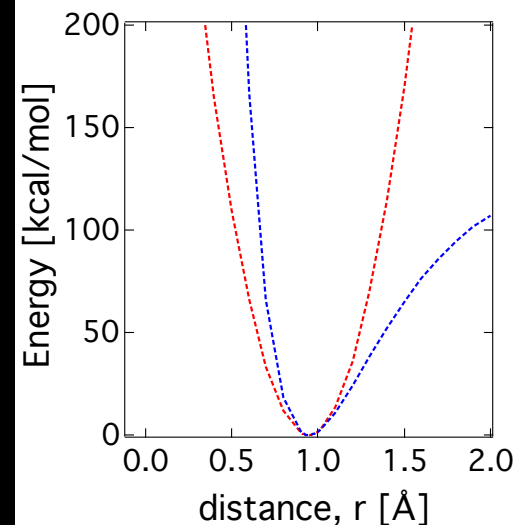
energy/frequency

$$\mu$$

reduced mass

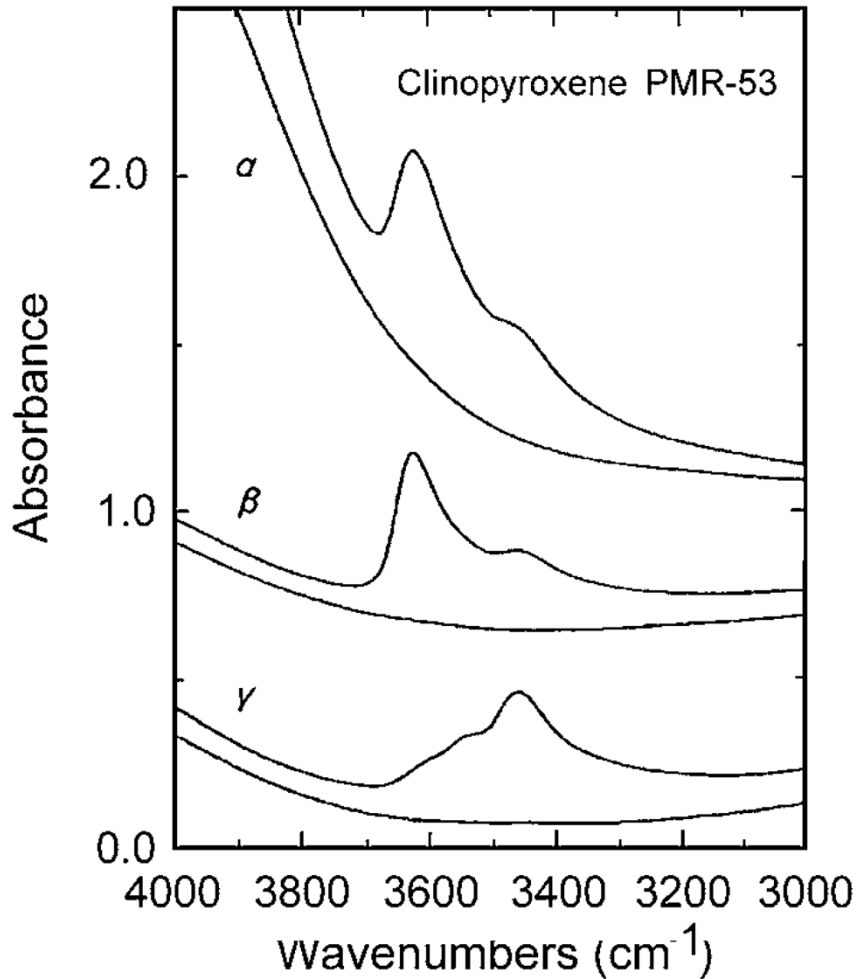
$$k$$

bond spring constant



number of vibrations that would occur in the time that light travels one cm

# Determination of Water



Rossmann (2006)

$$A(\nu) = \epsilon \times c \times t$$

A = Absorbance measured using FTIR

t = thickness of sample (cm)

$\epsilon$  = molar absorption coefficient  
(cm<sup>-2</sup> per mol<sub>H<sub>2</sub>O</sub>/l)

c = concentration

## Beer-Lambert law

# Determination of Water

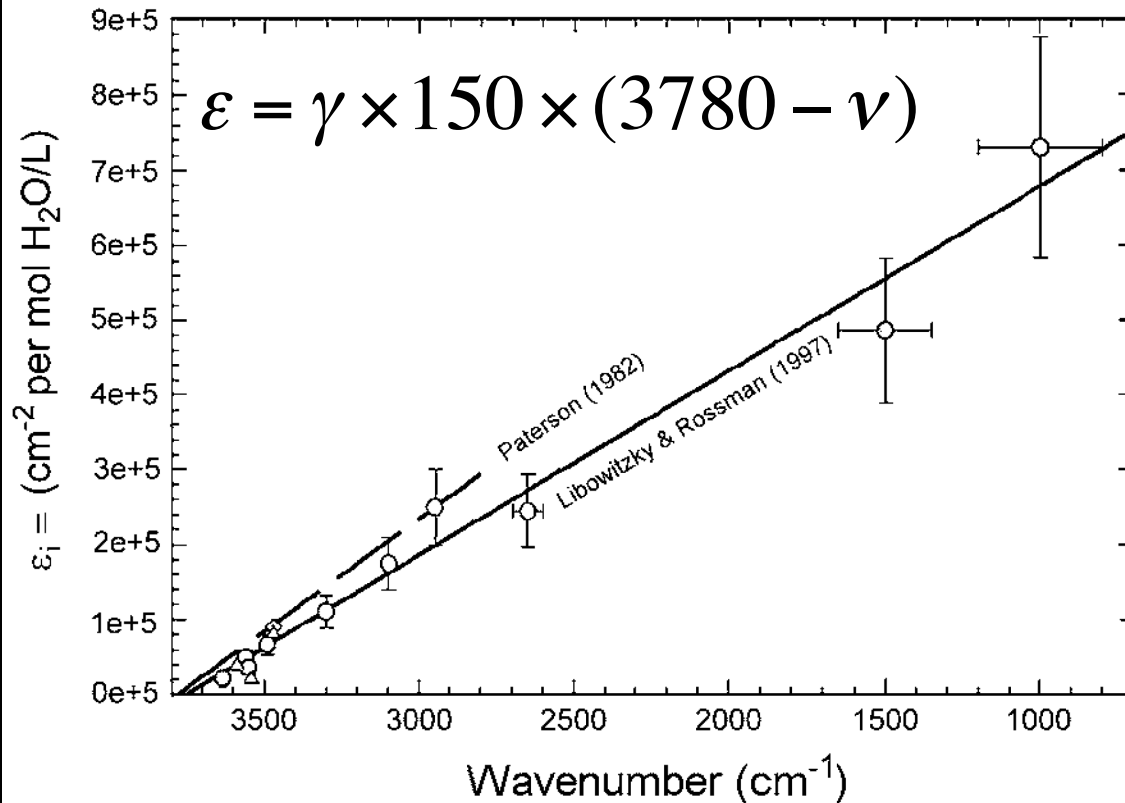


**Figure 2.** The correlation of the integrated molar absorption coefficient of OH stretching vs. wavenumber. Circles are experimental data points for stoichiometric minerals. The correlation of Paterson (1982) is shown for comparison. This means that if all things are equal, the Paterson trend underestimates the OH content. From Libowitzky and Rossman (1997).

$\gamma$  = geometric factor accounts for the anisotropy of the crystal based on an assumption that O-H bonds are oriented in a single direction

Various ways of expressing water contents: H/ $10^6$  Si, ppm, wt %:

for olivine  $\text{Fo}_{90}$ : 1 ppm wt  $\text{H}_2\text{O}$  = 16.35 H/ $10^6$  Si; for opx: 1 ppm wt  $\text{H}_2\text{O}$  = 11.49 H/ $10^6$  Si; for cpx: 1 ppm wt  $\text{H}_2\text{O}$  = 11.61 H/ $10^6$  Si.

Paterson 1982; Rossman 2006, Demouchy et al., 2015

# Determination of Water

$$A(\nu) = \varepsilon \times c \times t$$

Beer-Lambert law

$$\varepsilon = \gamma \times 150 \times (3780 - \nu)$$

$\gamma$  = geometric factor accounts for the anisotropy of the crystal based on an assumption that O-H bonds are oriented in a single direction  
B = density factor

$$C_{OH} = \frac{B}{\gamma \times 150} \int \frac{A(\nu)}{(3780 - \nu)} d\nu$$

# Determination of Water

SIMS (please refer to Rita's talk on volatiles)

NRA (Nuclear Reaction Analysis)

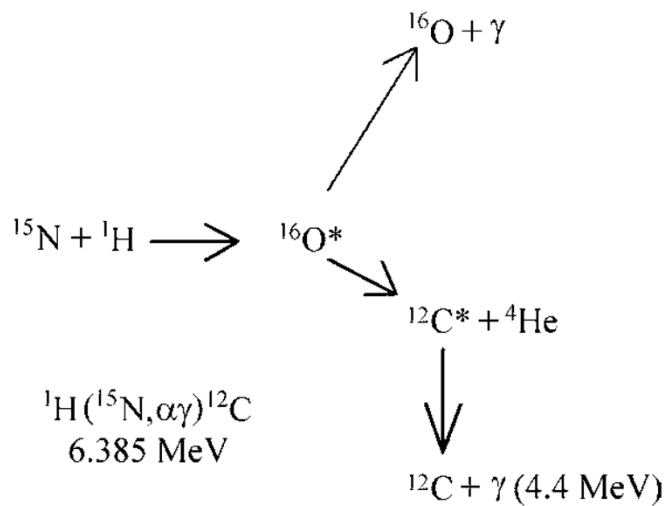
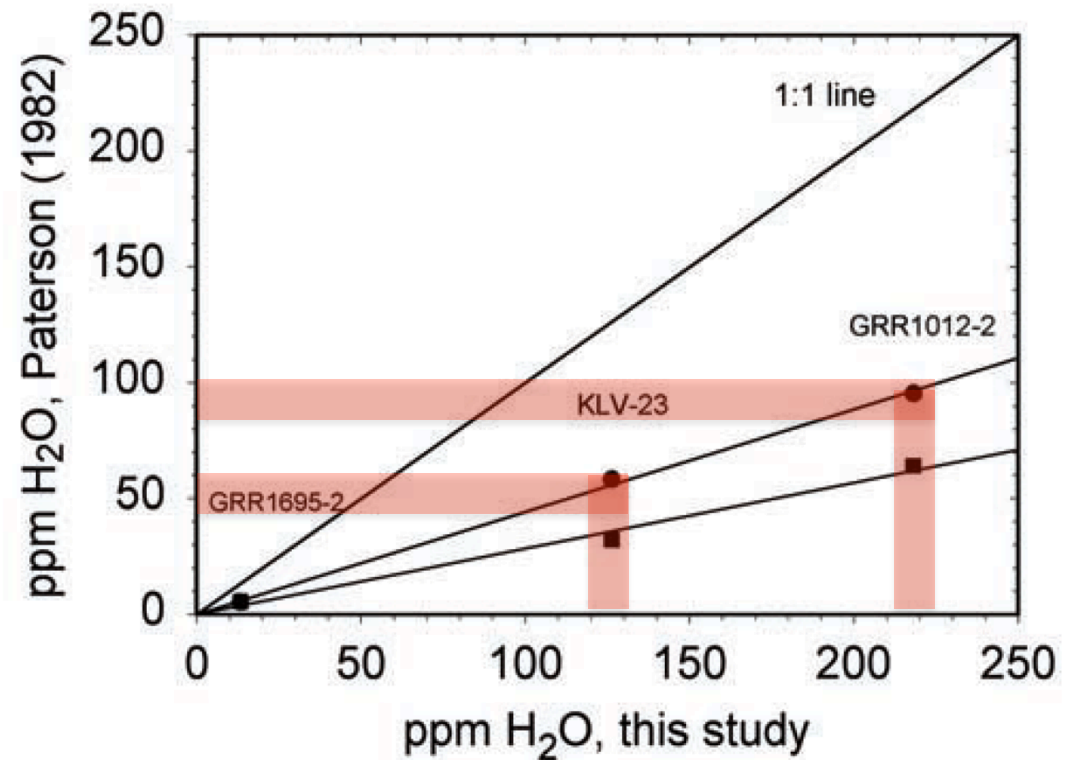


**Figure 8.** The nuclear reaction scheme in the  ${}^{15}\text{N}$  nuclear reaction method. The reaction of  ${}^{15}\text{N}$  and  ${}^1\text{H}$  produce  ${}^{16}\text{O}$  in a nuclear excited state. A decay path of oxygen produces  ${}^{12}\text{C}$ , which comes to the ground nuclear state with the emission of a 4.44 MeV gamma ray that is the analytical signal.



# Water in the deep Earth

*estimates from natural samples*

Water in volcanic rocks-

- Mid-ocean ridge basalt – 20-200 ppm
- Ocean islands: ~1000 ppm
- Island arc volcanoes: wt % or more

What is our current estimate of the water content of the mantle?

- 25 % MORB + 75 % OIB ~ 1.5 (+/- 0.8) Ocean
- 75 % MORB + 25 % OIB ~ 0.7 (+/- 0.4) Ocean
- 90 % MORB + 10 % OIB ~ 0.5 (+/- 0.3) Ocean

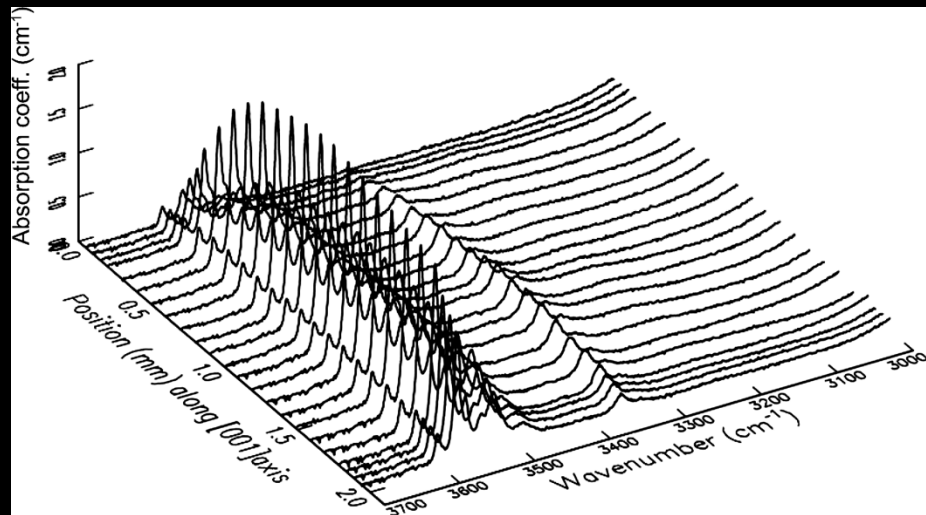
Mass of ocean ~  $1.4 \times 10^{21}$  kg

*(Please recall from Rita's talk on volatiles)*

*Hirschmann 2006*

# Natural Sample *challenges (?)*

1. Hydrogen diffusion in minerals are very fast ( $\sim 10^{-10}$  m<sup>2</sup>/s).
2. It is possible that water from olivine is lost during ascent. Often the water content recorded in natural crystals are not representative of the mantle.
3. Need for laboratory based experiments to determine hydrogen content at conditions relevant for the Earth's interior.

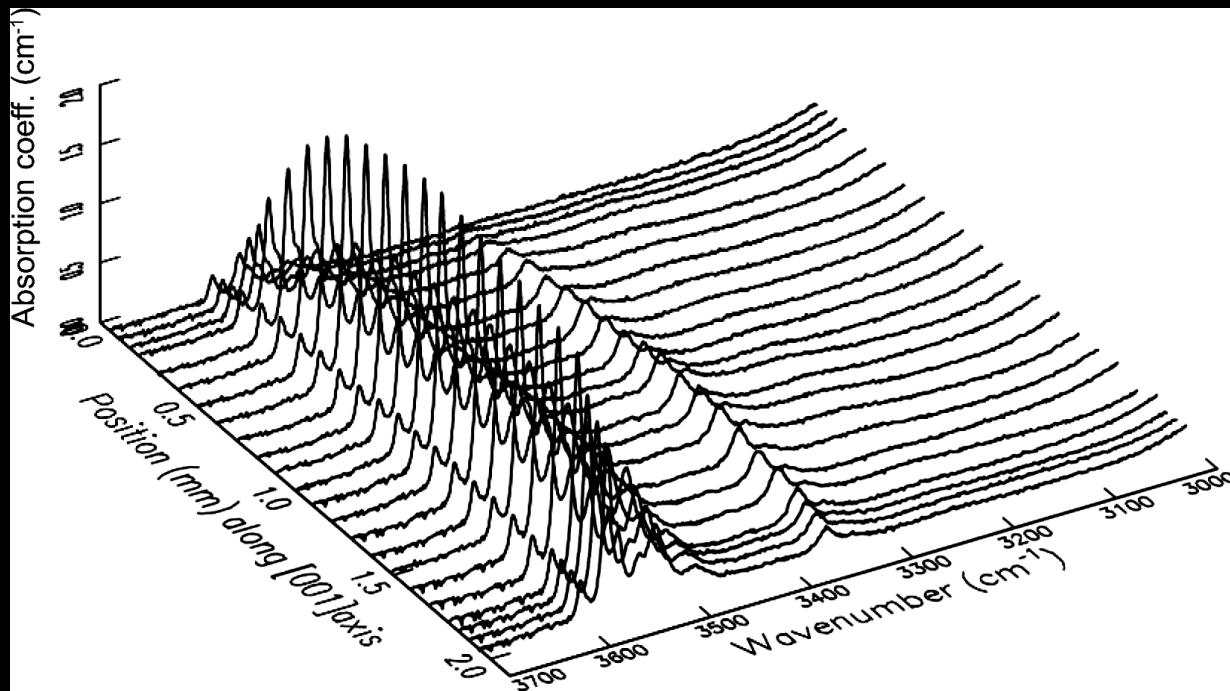


*Demouchy et al., 2006*

If magma transporting olivine xenocrysts was undersaturated in OH, then the olivine may have lost most of its original OH during its residence in the magma. Olivines from xenoliths in basalts, like San Carlos, may have had one or two orders of magnitude greater OH abundance prior to being stopped off into the basaltic magma. Alternatively, the olivines transported in the vapor-rich kimberlites may have even gained OH from the magma, and certainly should have lost less of their original OH content than would the olivines from basalt. Thus the abundance of OH in olivines in the mantle may be quite different from the abundances which we can measure in olivines of mantle origin. The measured abundances in crystals from volumi-

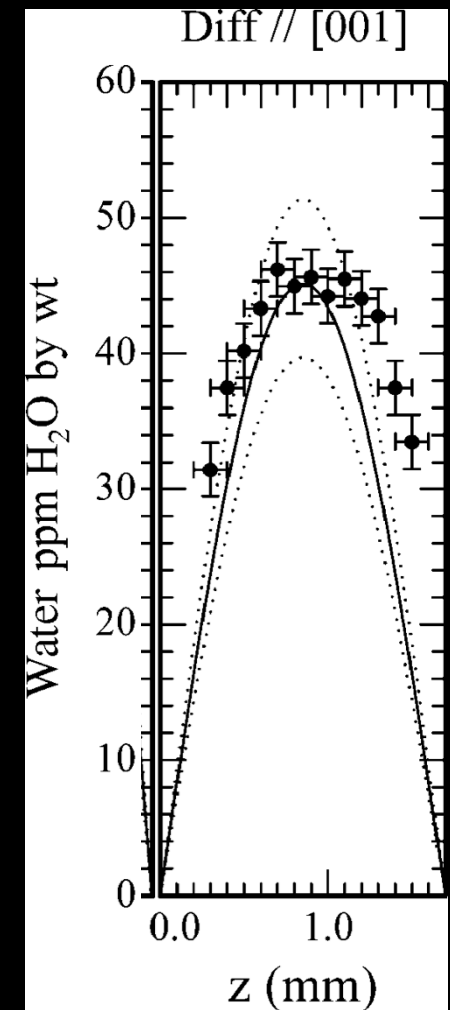
*Miller et al., 1987*

# Hydrogen Diffusion: Natural Sample



*Demouchy et al., 2006*

$$C_{OH}(x) = C_0 \left[ \operatorname{erfc} \frac{x}{\sqrt{Dt}} - \operatorname{erfc} \frac{X-x}{\sqrt{Dt}} \right]$$



2. Thermodynamics  
*Defects*  
&  
solubility of water (hydrogen)

# Solubility of water: NAMs

- Water solubility is the equilibrium water content of a mineral coexisting with an aqueous fluid phase.
- Water solubility is the equilibrium water content of a mineral coexisting with a hydrous melt in a phase assemblage that buffers the compositions of all coexisting phases in such a way that the composition of each phase only depends on pressure and temperature.

# Law of mass action

For a reaction



The equilibrium constant is defined as

$$K = \frac{[A]^a [B]^b}{[C]^c [D]^d}$$

$$\Delta G = -RT \ln(K)$$

$$K = \exp\left(-\frac{\Delta G}{RT}\right)$$

Please recall:  
Lars's lecture  
(thermodynamics)  
Zhicheng's lecture  
(melting):  
Chrystle's lecture  
 $\mu = RT \ln X$

# Fugacity

*Fugacity ~ partial pressure*

$$d\mu = -sdT + vdP$$

$\mu$

*molar free energy (chemical potential)*

$s$

*molar entropy*

$v$

*molar volume*

$id$

*ideal gas*

*Please recall:  
Chrystle's lecture*

$$PV_{id} = nRT$$

$$v_{id} = \frac{RT}{P}$$

# Fugacity

$$PV_{id} = nRT$$

$$v_{id} = \frac{RT}{P}$$

$$d\mu = -sdT + vdP$$

At constant T,  $dT=0$

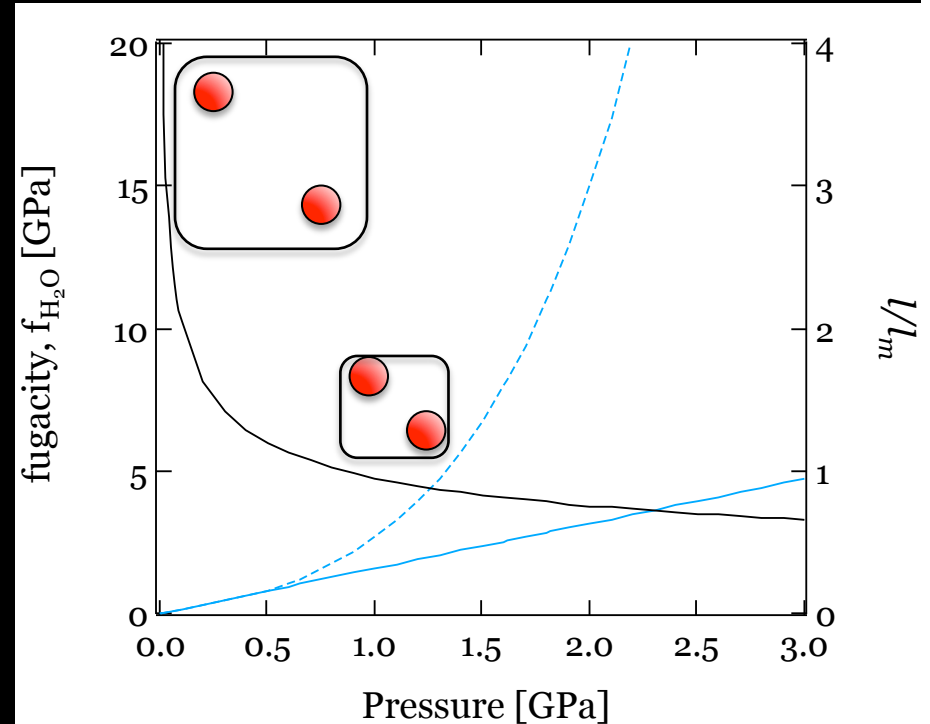
$$\mu = \int_{P_0}^P \frac{RT}{P} dP = RT \ln \left( \frac{P}{P_0} \right)$$

Please recall Lars's lecture on thermodynamics  
Zhicheng's lecture on melting:  $\mu = RT \ln X$

# Fugacity

*At low pressure with large separation between individual gas molecules, an ideal gas behavior may be approximated.*

*As the separation distance between the molecules decreases, significant deviation from ideal gas behavior is likely to occur.*



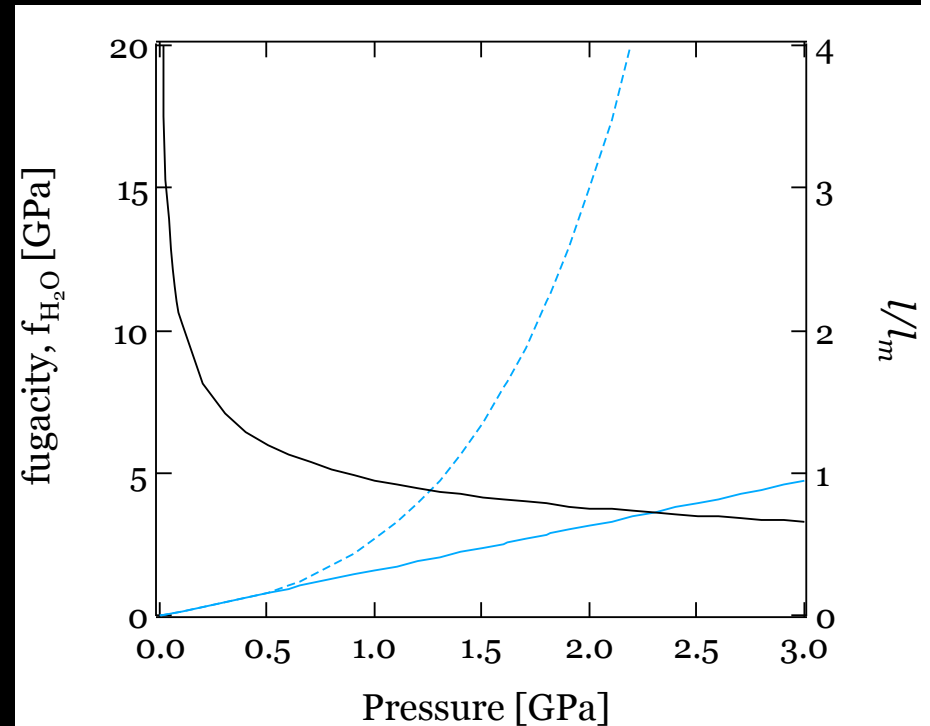
$$\textit{ideal} : [RT \ln(P / P_0)]$$

$$\textit{real} : [RT \ln(f / P)]$$

# Fugacity

*At low pressure with large separation between individual gas molecules, an ideal gas behavior may be approximated.*

*As the separation distance between the molecules decreases, significant deviation from ideal gas behavior is likely to occur.*



$$d\mu = RT \ln(f)$$

$$\lim_{P \rightarrow 0} \frac{f}{P} = 1$$

# Fugacity and Equation of state

$$v(P, T) = \frac{RT}{P} - \frac{a(T)R\sqrt{T}}{(RT + b(T)P) \times (RT + 2b(T)P)} + b(T)P + c(T)\sqrt{P} + d(T)P$$

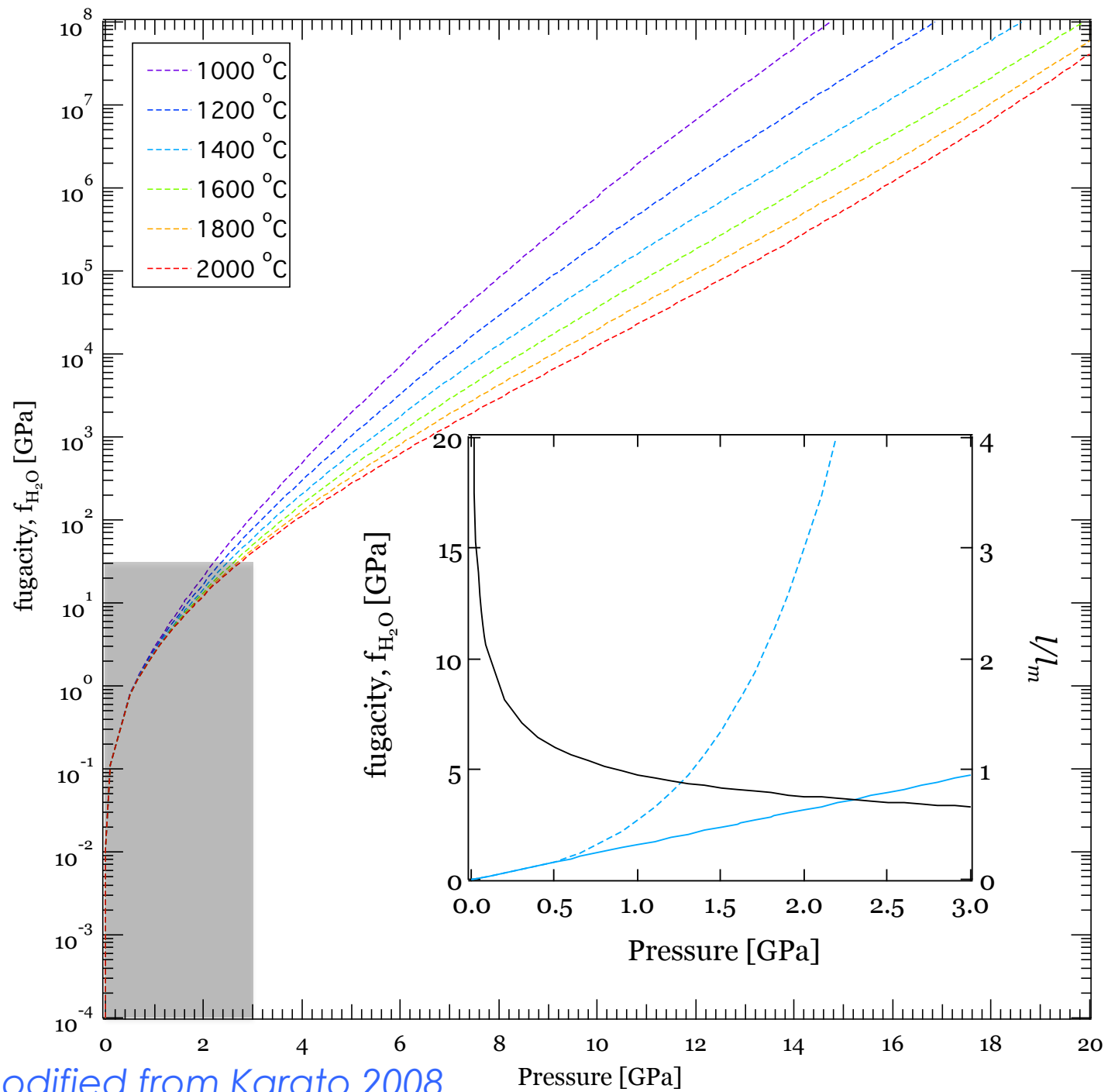
$$m = m_0 + m_1T + m_2T^2; m = a, b, c, d$$

$$\log \frac{f(P, T)}{P} = \frac{1}{RT} \int_0^P v(P, T) dP$$

Frost & Wood (1997)

Table 3. Coefficients for Eqn. 4.

	CO <sub>2</sub>	H <sub>2</sub> O
a <sub>0</sub>	5.373 × 10 <sup>7</sup>	5.3957 × 10 <sup>8</sup>
a <sub>1</sub>	5.6829 × 10 <sup>4</sup>	-6.362 × 10 <sup>5</sup>
a <sub>2</sub>	-40.45	236.81
b <sub>0</sub>	42.88	27.732
b <sub>1</sub>	—	-2.0179 × 10 <sup>-2</sup>
b <sub>2</sub>	—	9.2125 × 10 <sup>-6</sup>
c <sub>0</sub>	-0.238	-0.1244
c <sub>1</sub>	3.618 × 10 <sup>-5</sup>	1.79 × 10 <sup>-4</sup>
c <sub>2</sub>	—	-7.8587 × 10 <sup>-8</sup>
d <sub>0</sub>	3.707 × 10 <sup>-4</sup>	2.186 × 10 <sup>-4</sup>
d <sub>1</sub>	1.198 × 10 <sup>-9</sup>	-3.6836 × 10 <sup>-7</sup>
d <sub>2</sub>	-1.0464 × 10 <sup>-11</sup>	1.6127 × 10 <sup>-10</sup>



*modified from Karato 2008*

# Kröger Vink Notation

$+ive = \bullet$

$-2ive = ''$

$neutral = x$

$M = metal$

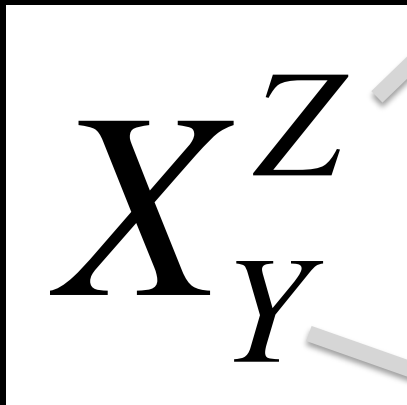
$Si = silicon$

$i = interstitial$

*effective charge*

*defect  
species*

*site*



# Kröger Vink Notation



*Ferric iron  $Fe^{3+}$  in metal site i.e.,  $MO_6$  octahedral site of a mineral*



*Ferrous iron  $Fe^{2+}$  in metal site i.e.,  $MO_6$  octahedral site of a mineral, why neutral? Since it replaces  $Mg^{2+}$  and hence no charge imbalance is created*

# Kröger Vink Notation

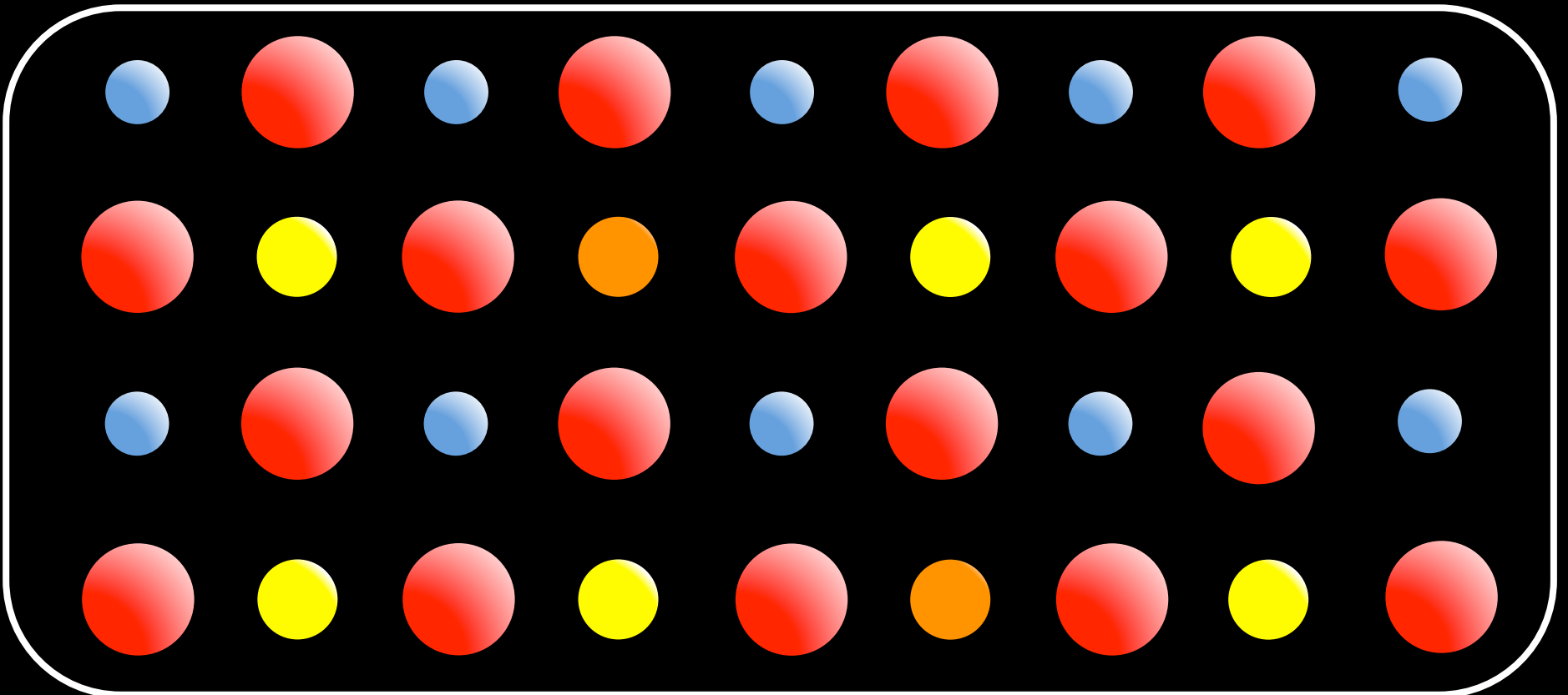
$$h^{\bullet}$$

*Electron hole with a +ive charge*

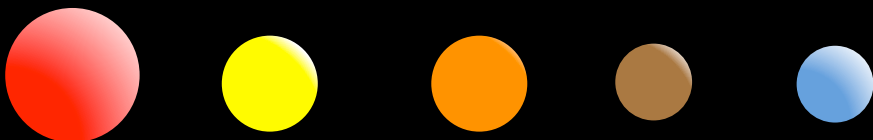
$$V_M''$$

*Vacancy in metal site which would have otherwise been occupied by  $Mg^{2+}$  or  $Fe^{2+}$ . So it has -2ive effective charge with respect to perfect lattice*

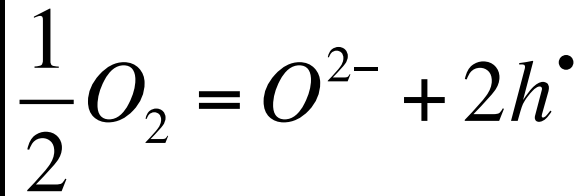
# Point defect of Fe bearing system: effect of fugacity ( $f_{O_2}$ )



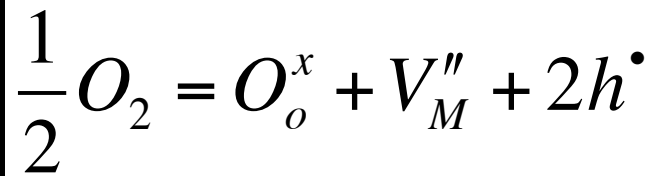
$O^{2-}$   $Mg^{2+}$   $Fe^{2+}$   $Fe^{3+}$   $Si^{4+}$



# Defects/vacancy: effect of $f_{O_2}$



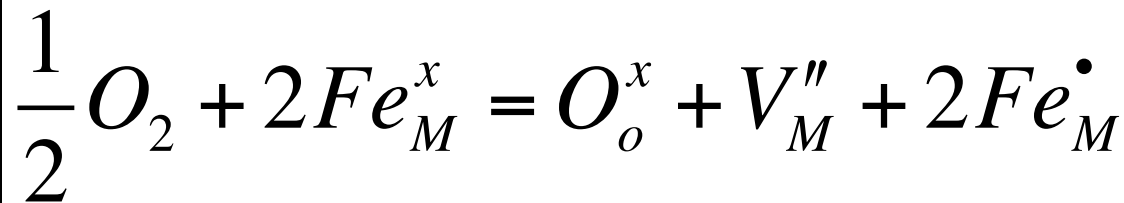
A mineral surface interacts with  $O_2$ .



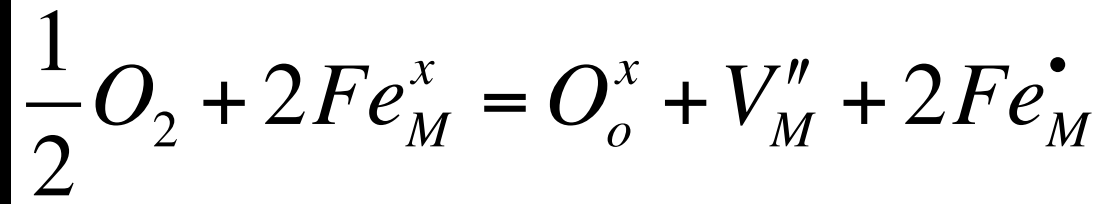
It may generate a vacancy inside the mineral through the following series of reactions.



oxidation of Fe site, i.e.,  
 $Fe^{2+}$  to  $Fe^{3+}$



# Defects/vacancy: effect of $f_{O_2}$



$$K = \frac{[Fe_M^\bullet]^2 [V_M'']}{[f_{O_2}]^{1/2}}$$

$$[Fe_M^x] \sim 1$$

$$[O_o^x] \sim 1$$

# Charge Neutrality

*Electrostatic interaction energy is large. Charge neutrality must be maintained*

*Concentration of all positively charged defects*

=

*Concentration of all negatively charged defects*

$$[Fe_M^\bullet] + [h^\bullet] + 2[V_o^{\bullet\bullet}] + \dots \equiv [e'] + 2[V_M''] + 4[V_{Si}'''] + \dots$$

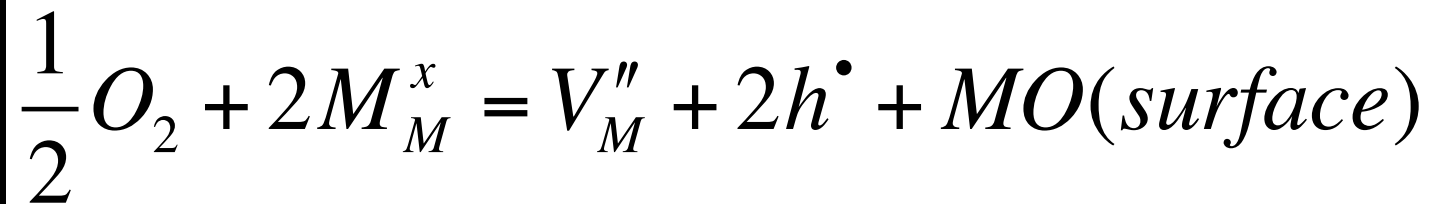
$$2[V_M''] = [Fe_M^\bullet] \equiv [h^\bullet]$$

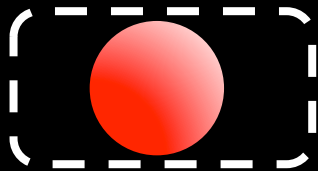
# Point defects: *effect of oxide activity*

*Oxide activity is controlled by the presence of secondary phases.*

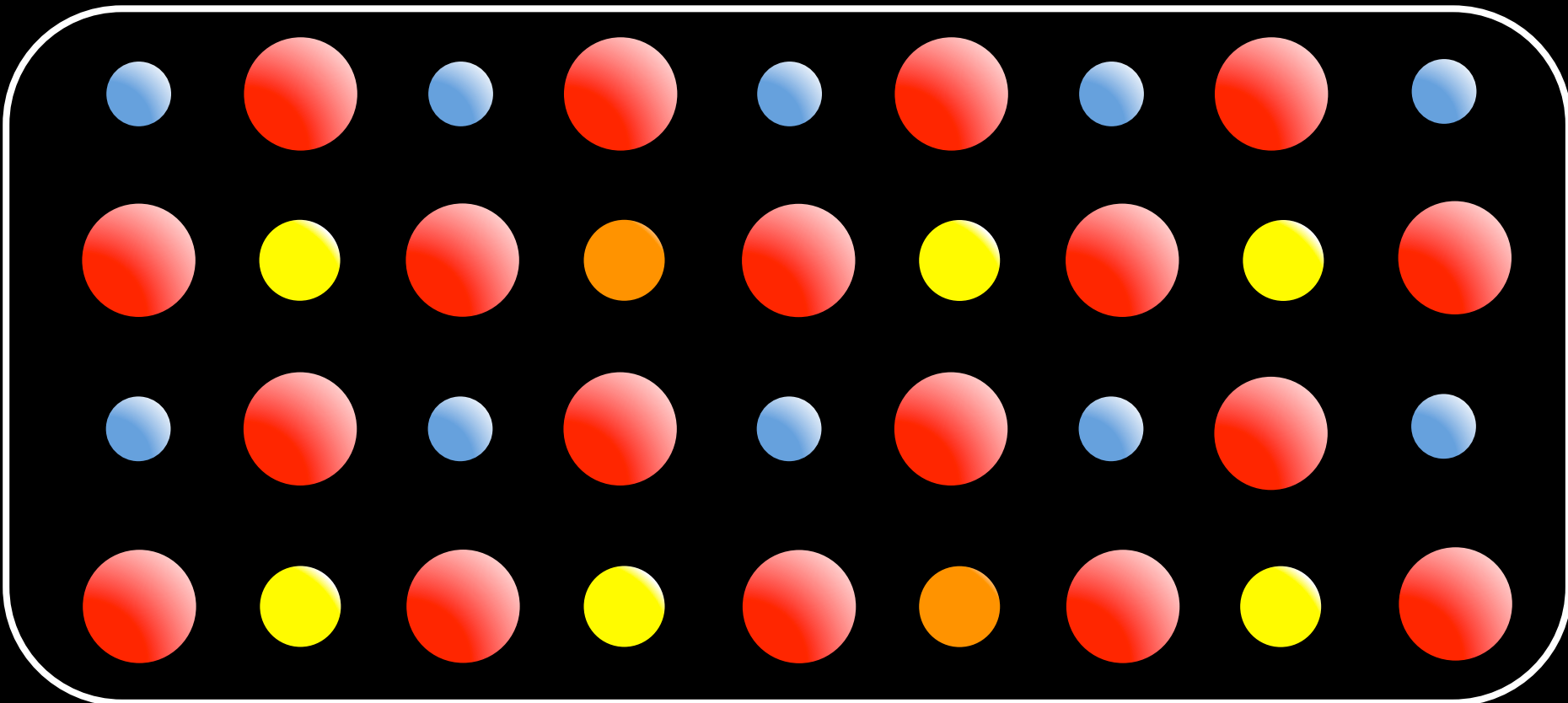
*For example, when olivine ( $Mg_2SiO_4$ ) co-exists with pyroxene ( $MgSiO_3$ ) then the activity of MgO is low.*

*olivine Mg:Si:: 2:1 surrounded by pyroxene Mg:Si::1:1*



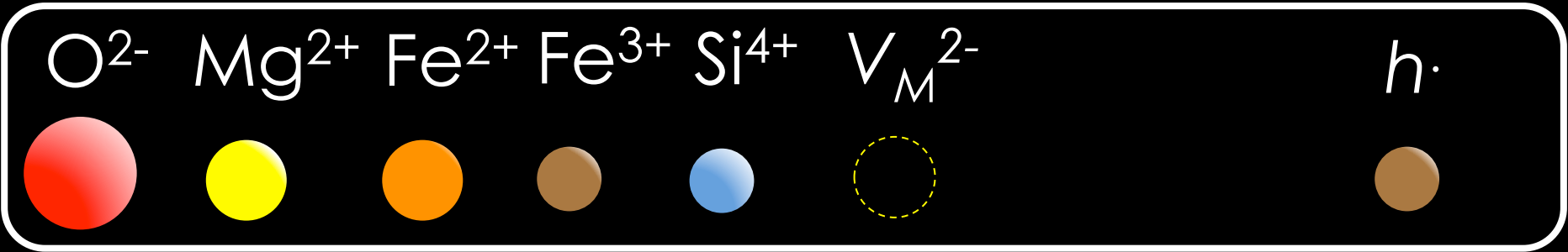
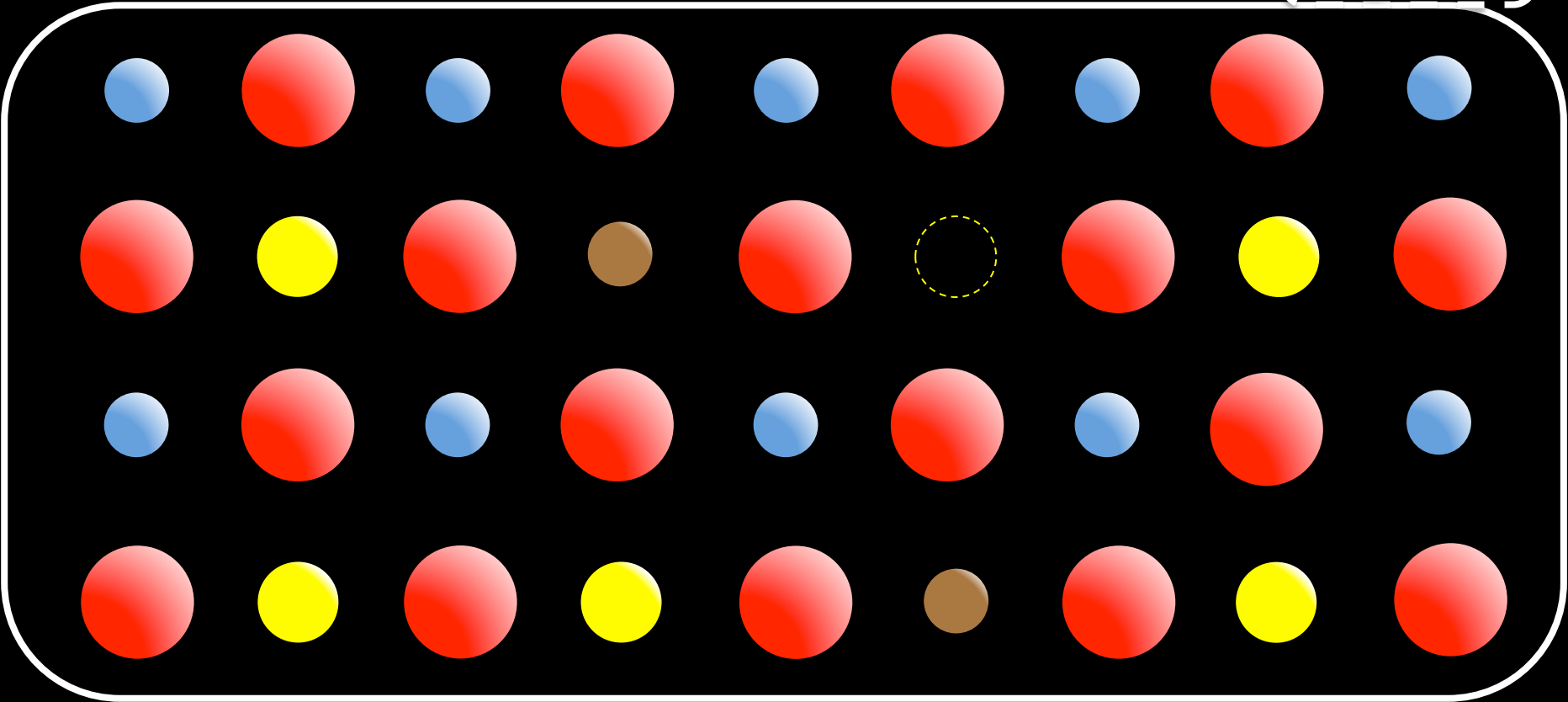
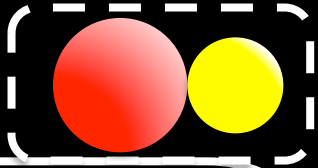


+



$O^{2-}$   $Mg^{2+}$   $Fe^{2+}$   $Fe^{3+}$   $Si^{4+}$

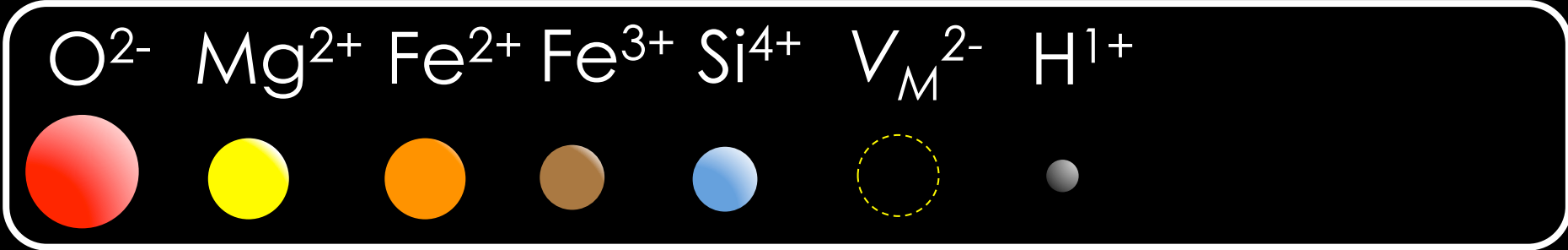
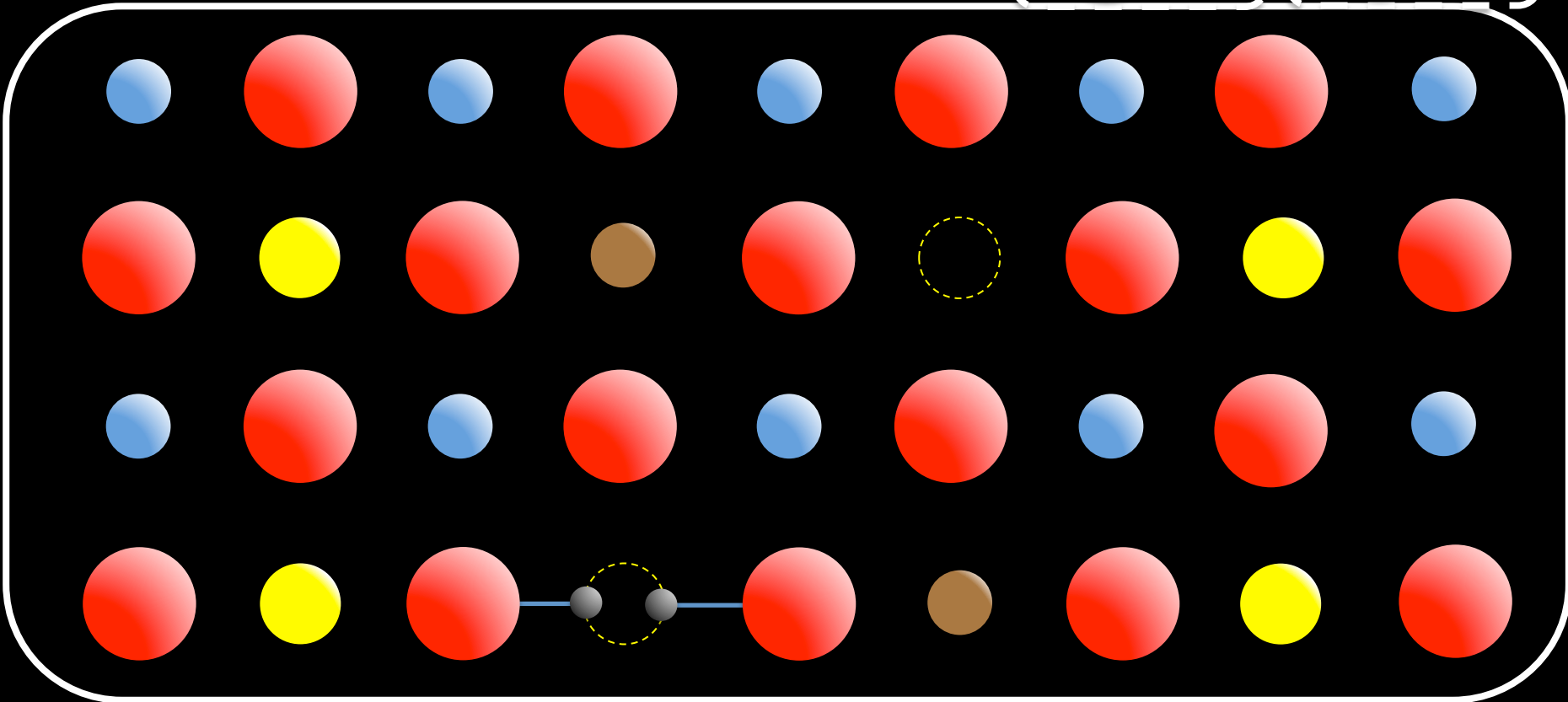
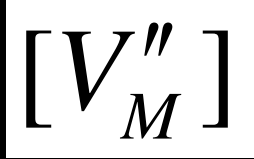


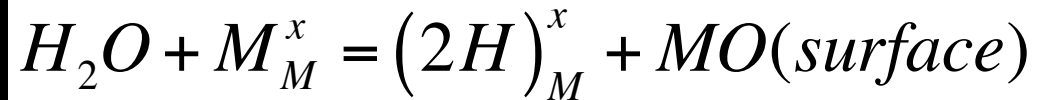


# Defects/vacancy: effect of $f_{O_2}$

$$[Fe_M^\bullet] \propto f_{O_2}^p a_{MO}^q K^r$$

$$2[V_M''] \propto f_{O_2}^p a_{MO}^q K^r$$



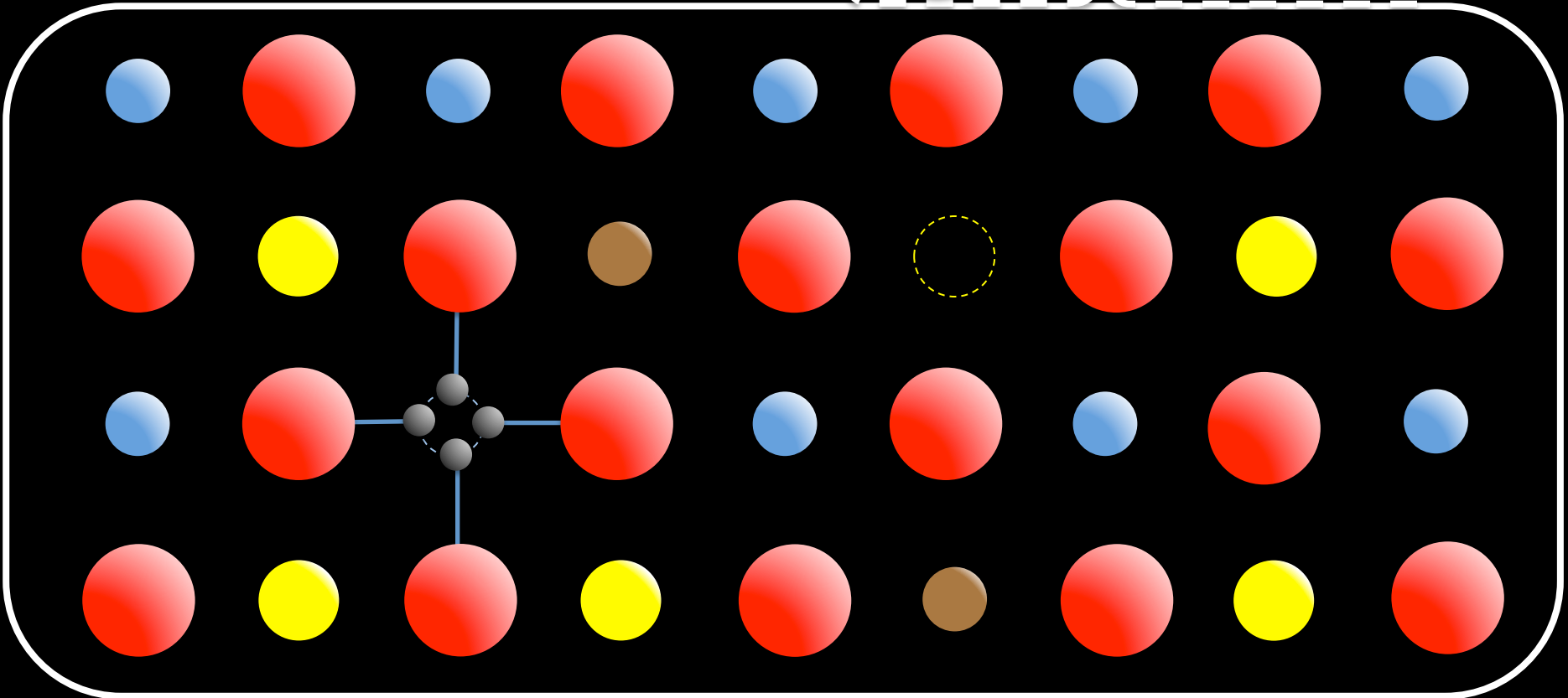


$$M = Mg, Fe$$

$$K(T, P) = \frac{[(2H)_M^x] \times a_{MeO}}{f_{H_2O}}$$

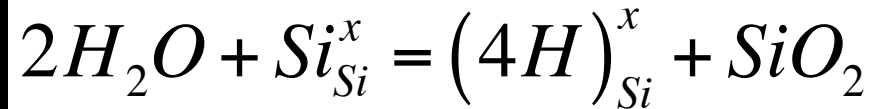
$$K(T, P) = \exp\left[-\frac{\Delta H + P\Delta v_{MO} - T\Delta S}{RT}\right]$$

$$[(2H)_M^x] = f_{H_2O} \times a_{MO}^{-1} \times \exp\left[-\frac{\Delta H + P\Delta v_{MO} - T\Delta S}{RT}\right]$$



$O^{2-}$     $Mg^{2+}$     $Fe^{2+}$     $Fe^{3+}$     $Si^{4+}$     $V_M^{2-}$     $V_{Si}^{4-}$     $H^{1+}$     $h\cdot$





$$K(T, P) = \frac{[(4H)_{Si}^x] \times a_{SiO_2}}{f_{H_2O}^2}$$

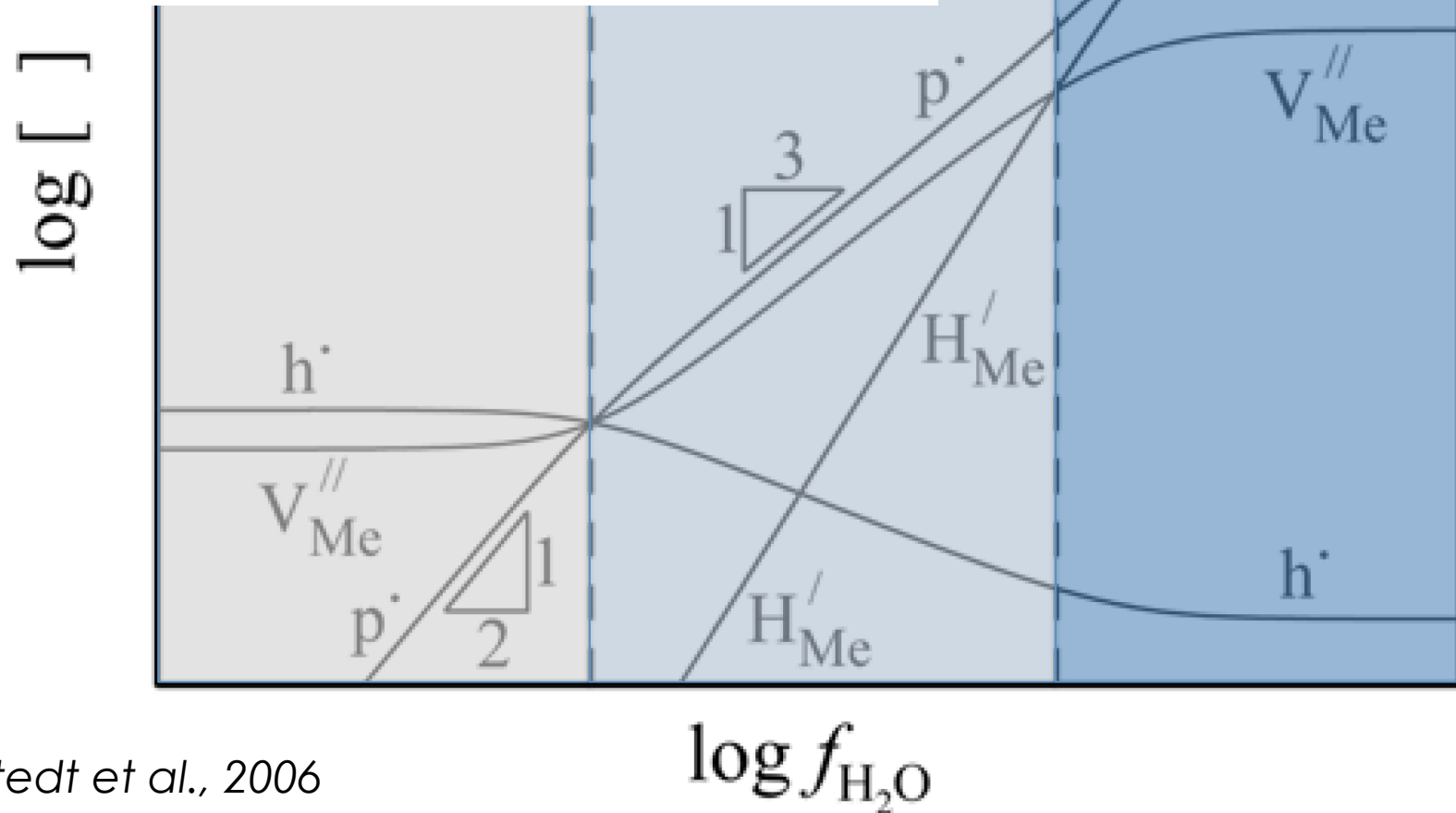
$$K(T, P) = \exp \left[ -\frac{\Delta H + P\Delta v_{SiO_2} - T\Delta S}{RT} \right]$$

$$[(4H)_{Si}^x] = f_{H_2O}^2 \times a_{SiO_2}^{-1} \times \exp \left[ -\frac{\Delta H + P\Delta v_{SiO_2} - T\Delta S}{RT} \right]$$

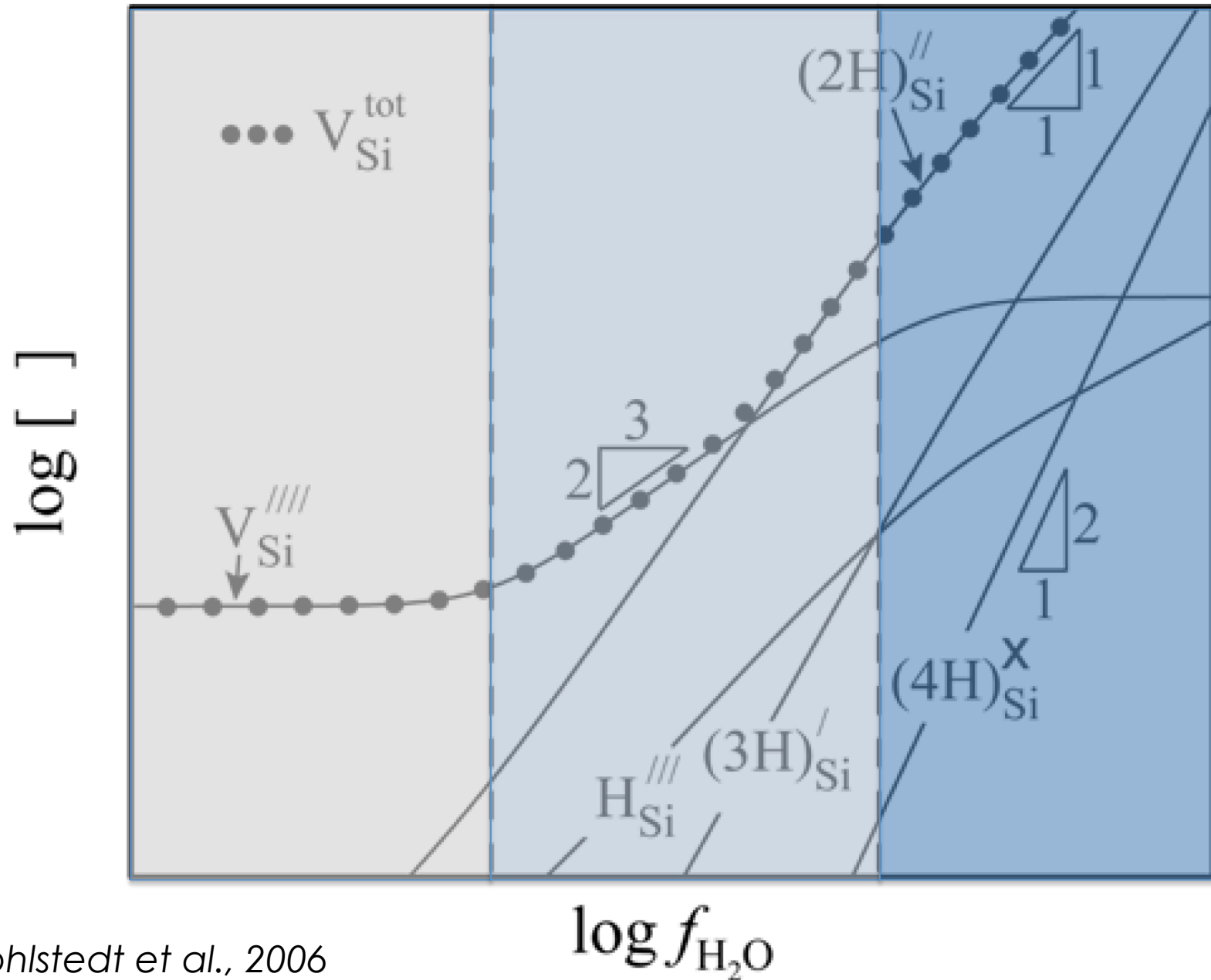
$$[h^{\bullet}] = 2[V_{Me}^{//}] \quad [p^{\bullet}] = 2[V_{Me}^{//}] \quad [p^{\bullet}] = [H_{Me}^{\prime}]$$

Thermodynamic provides a framework for understanding defects but does not tells us about the magnitude defect concentration (experiments).

**Defect concentration in Logarithmic scale.**



$$[h'] = 2[V_{Me}^{//}] \quad [p'] = 2[V_{Me}^{//}] \quad [p'] = [H_{Me}']$$



# 3. Water Solubility Experiments

# High P-T Experiments

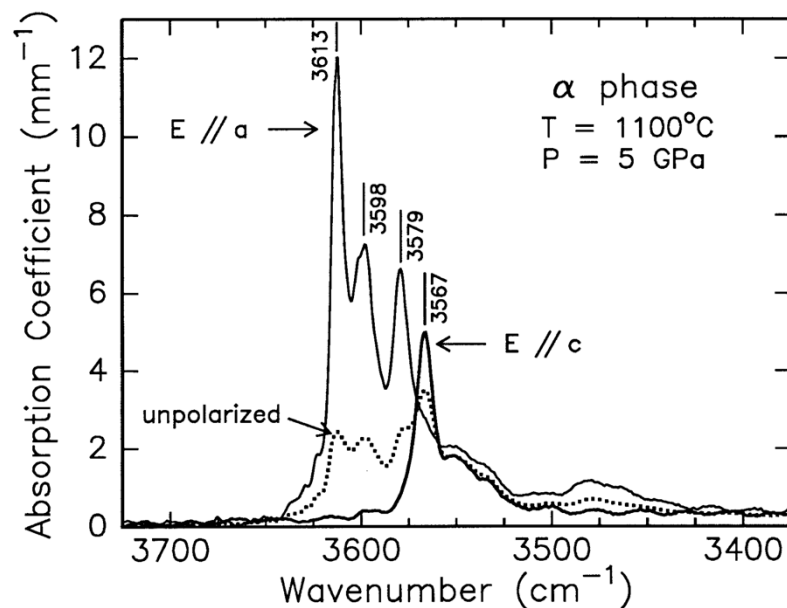


**Fig. 6** Unpolarized and two polarized FTIR spectra obtained on a sample hydrothermally annealed in the  $\alpha$  field at 5 GPa and 1100 °C. Four dominant absorption peaks are labeled

*Kohlstedt et al., 1996*

# Olivine

please recall  
thermodynamic  
model  
 $\log [ ]$  vs.  $\log f_{\text{H}_2\text{O}}$

Kohlstedt et al., 1996

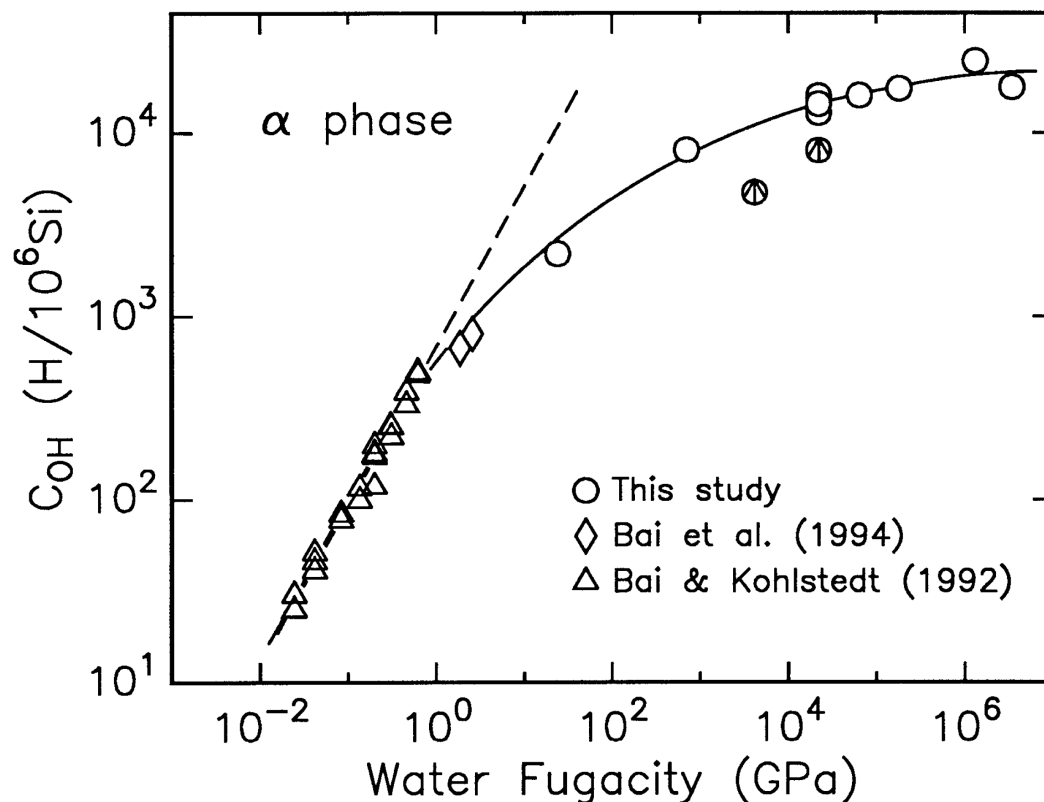


**Fig. 5** Log-log plot of OH solubility versus water fugacity. *Circles* are data obtained in the present study; *circles containing arrows* denote runs in which no water was present at the end of the hydrothermal anneal. The data at 8 GPa have been separated along the vertical axis so that all three points are visible. *Triangles* are results from gas-medium experiments of Bai and Kohlstedt (1992), combined with more recent results from our laboratory. *Diamonds* are data from solid-medium experiments of Bai, Bai and Kohlstedt (1994, private communication). The *dashed line* is a linear least squares fit to the data of Bai and Kohlstedt (1992). The *curved line* is calculated from Eq. 16 with  $A(T) = 1.1 \text{ H}/10^6\text{Si}$  at  $1100^\circ\text{C}$  and  $\Delta V_{\text{H}_2\text{O}} = 10.6 \times 10^{-6} \text{ m}^3/\text{mol}$  with the  $f_{\text{H}_2\text{O}}$  calculated from Pitzer and Sterner (1994), as described in the Discussion section

please recall  
thermodynamic  
model  
 $\log [ ]$  vs.  $\log f_{H_2O}$

$$C_{water} = A f_{H_2O}^n \times \exp \left[ -\frac{\Delta H + P\Delta v}{RT} \right]$$

$$\log C_{water} \propto n \log f_{H_2O}$$

Kohlstedt et al., 1996

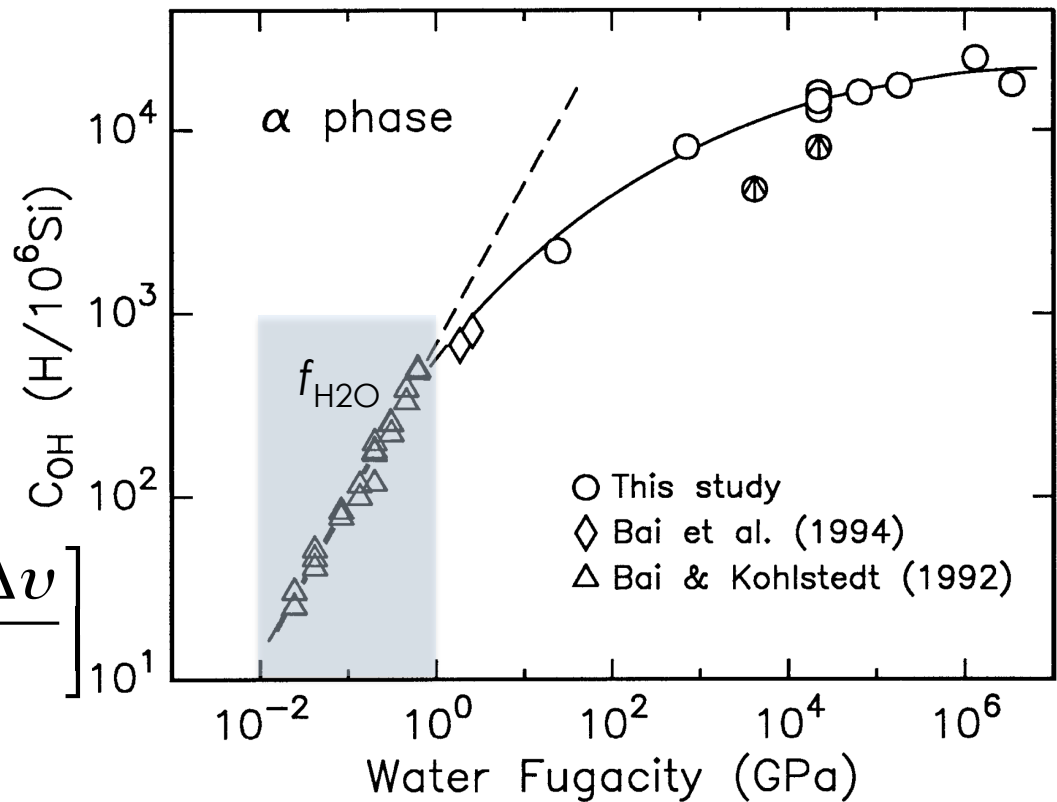


**Fig. 5** Log-log plot of OH solubility versus water fugacity. *Circles* are data obtained in the present study; *circles containing arrows* denote runs in which no water was present at the end of the hydrothermal anneal. The data at 8 GPa have been separated along the vertical axis so that all three points are visible. *Triangles* are results from gas-medium experiments of Bai and Kohlstedt (1992), combined with more recent results from our laboratory. *Diamonds* are data from solid-medium experiments of Bai, Bai and Kohlstedt (1994, private communication). The *dashed line* is a linear least squares fit to the data of Bai and Kohlstedt (1992). The *curved line* is calculated from Eq. 16 with  $A(T) = 1.1 \text{ H}/10^6 \text{ Si}$  at 1100 °C and  $\Delta V_{\{ \}} = 10.6 \times 10^{-6} \text{ m}^3/\text{mol}$  with the  $f_{H_2O}$  calculated from Pitzer and Sterner (1994), as described in the Discussion section

please recall  
thermodynamic  
model  
 $\log [ ]$  vs.  $\log f_{\text{H}_2\text{O}}$

$$C_{\text{water}} = A f_{\text{H}_2\text{O}}^n \times \exp \left[ -\frac{\Delta H + P\Delta v}{RT} \right]$$

$$\log \left( \frac{C_{\text{water}}}{f_{\text{H}_2\text{O}}^n} \right) \propto \left[ -\frac{P\Delta v}{RT} \right]$$

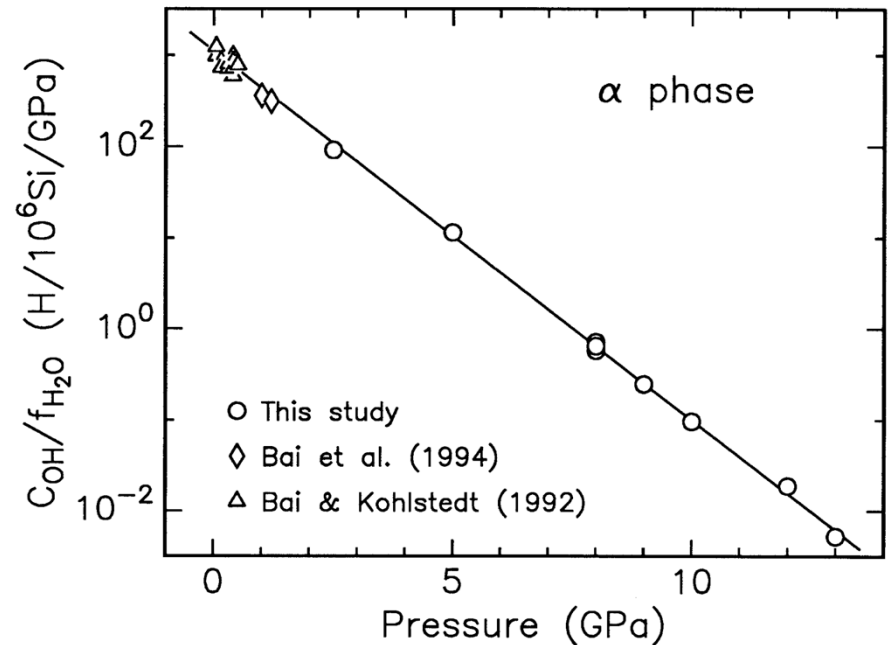
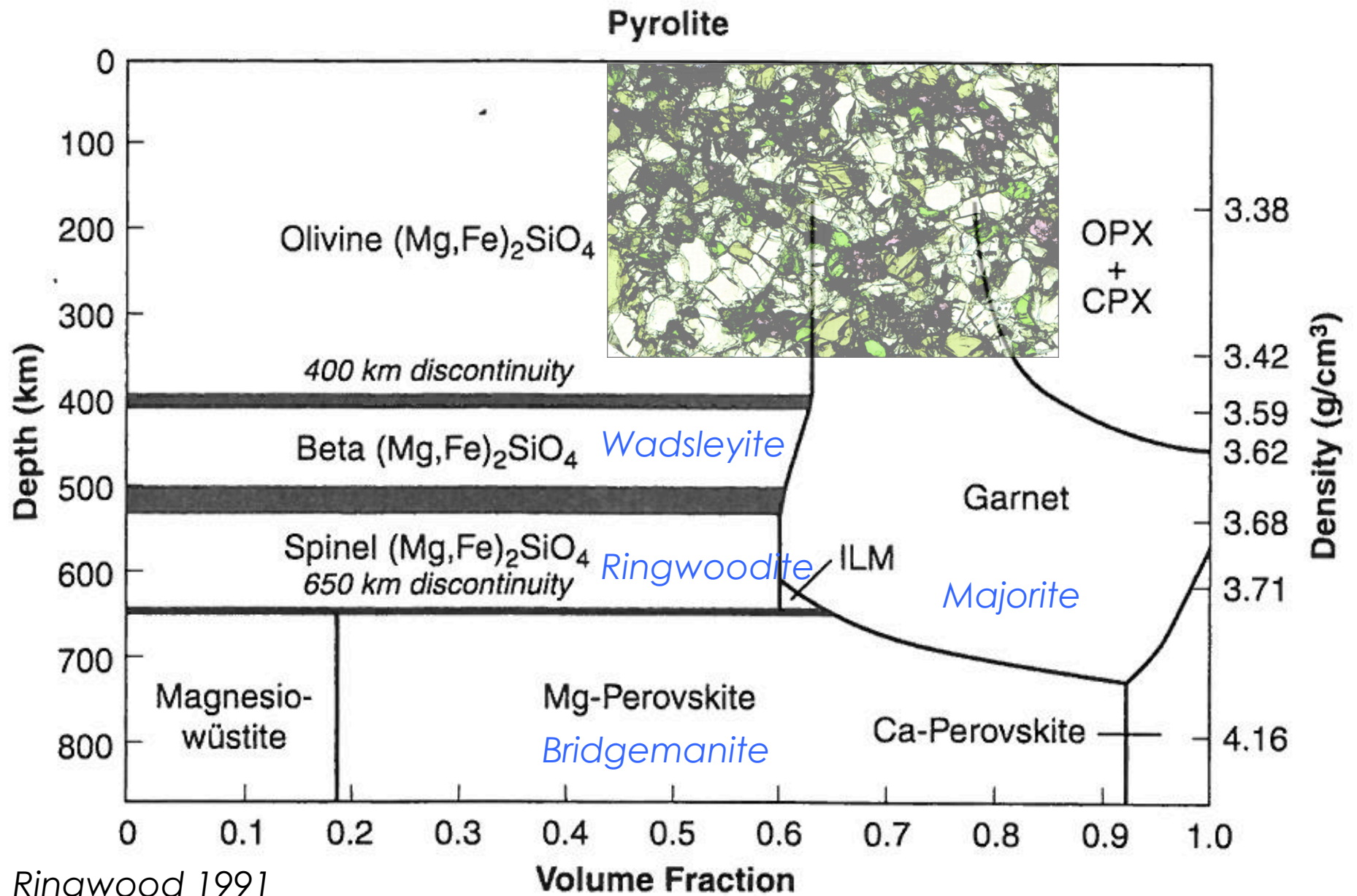


**Fig. 11** Semi-log plot of OH concentration divided by water fugacity versus confining pressure for samples annealed in the  $\alpha$ -stability field. The molar volume change resulting from the incorporation of hydroxyl into the olivine structure is calculated from the slope of the linear least-squares fit of these data, as illustrated in Eqs. 15 and 16. The three data points at 8 GPa have been separated for clarity; the low-pressure data are plotted so as not to overlie one another. See the caption for Fig. 5 for additional information

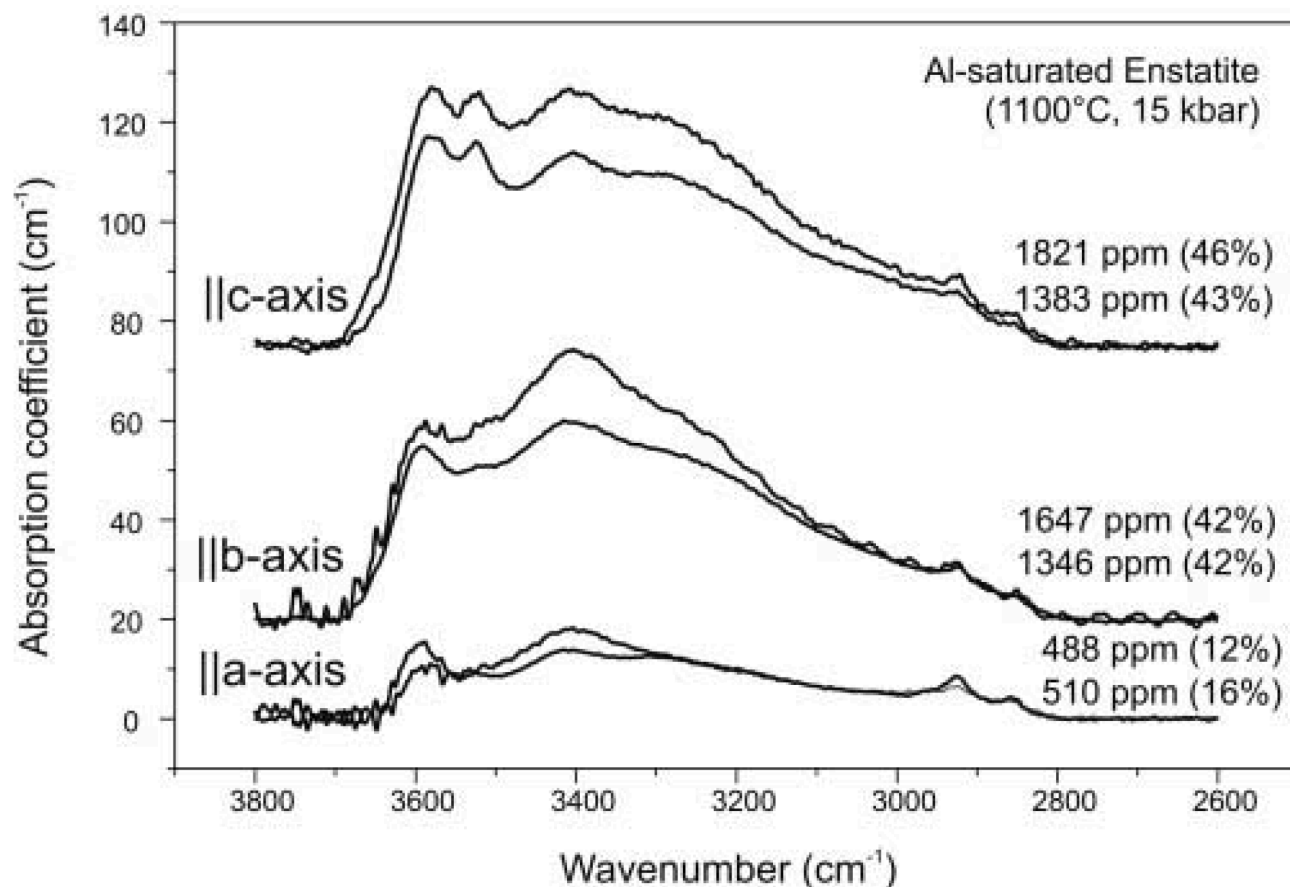
# Mineralogy of the upper mantle



Ringwood 1991

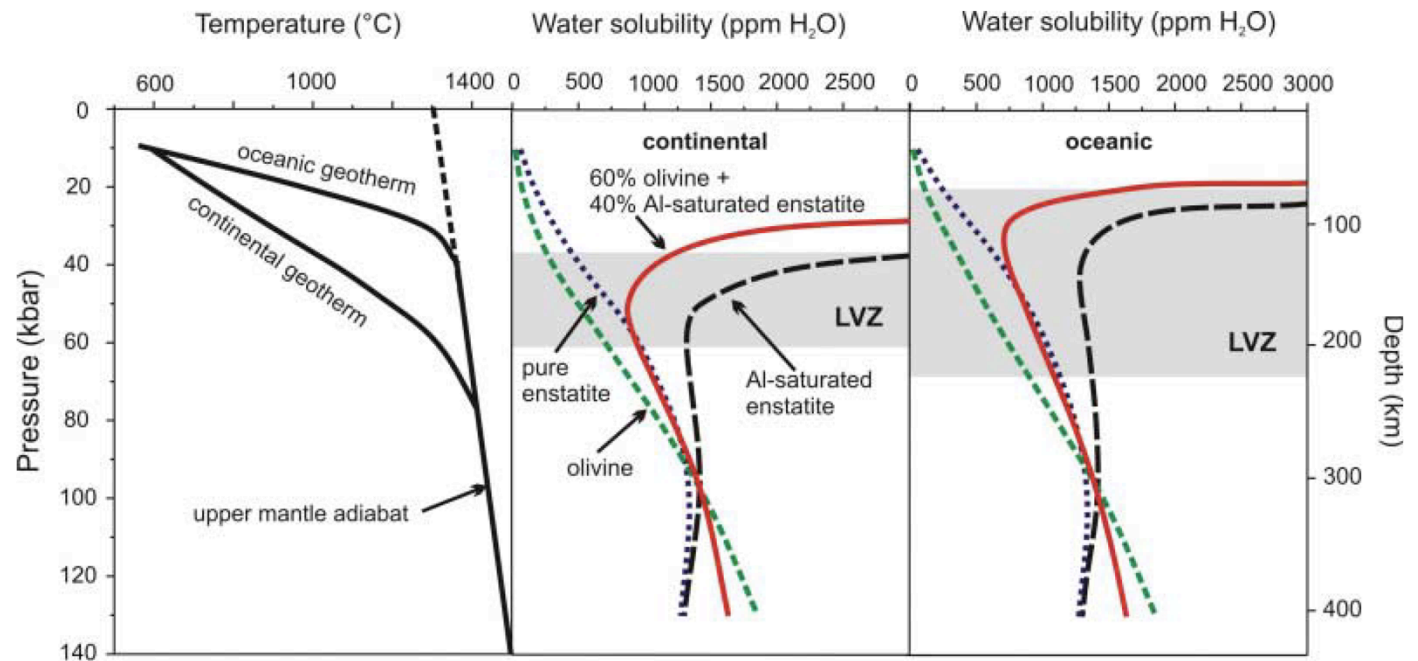
# Pyroxene (aluminous enstatite)

**Fig. 1.** Polarized infrared spectra of two aluminum-saturated enstatite crystals synthesized at 1100°C and 15 kbar. Water contents (in ppm) correspond to the absorbances measured parallel to the three crystallographic axes. Bulk water contents are obtained by adding these values. Numbers in parentheses denote percentage of total water observed in each of the three directions of polarization. The spectra shown here and in Fig. 2 were obtained from the raw data by subtracting a linear baseline defined by the points at 3800  $\text{cm}^{-1}$  and 2800  $\text{cm}^{-1}$ . The two weak features between 2800  $\text{cm}^{-1}$  and 3000  $\text{cm}^{-1}$  could be due to organic surface contamination. However, they persisted after repolishing and they may therefore be intrinsic to the sample.



# Pyroxene (aluminous enstatite)

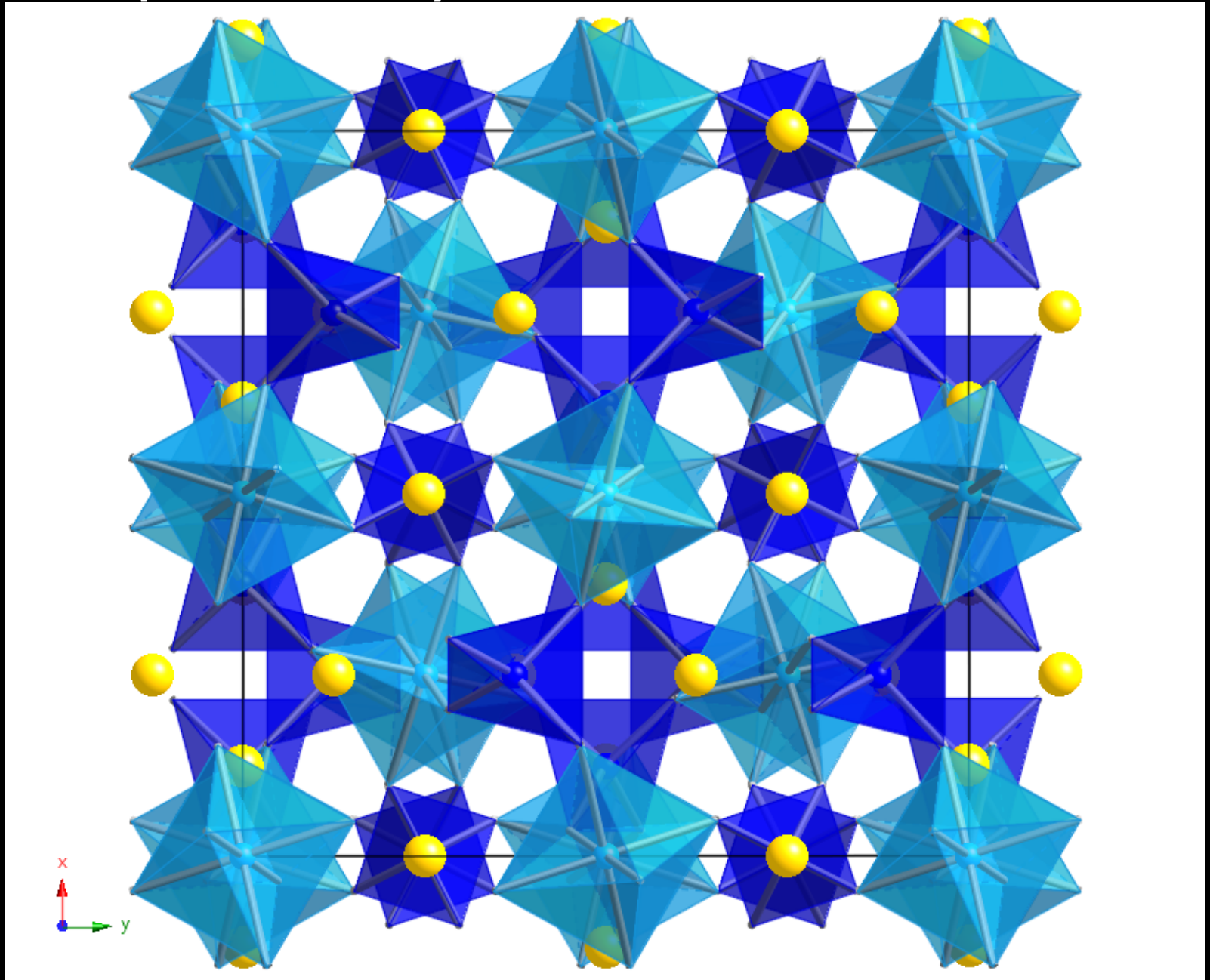
**Fig. 4.** Water solubility (in ppm by weight) in upper-mantle minerals as a function of depth for a typical continental shield and oceanic geotherm (26). The typical position of the low-velocity zone (LVZ) below continental shields and below oceans is shaded in gray. Water solubility in olivine is according to Kohlstedt *et al.* (7). Water solubility in aluminum-saturated enstatite was calculated from Eqs. 1 and 2. Recently (27), it was suggested that the infrared extinction coefficient of water in olivine may be considerably smaller than previously thought. If this new calibration were applied, the water solubility in olivine would increase by a factor of about 2.5. This would somewhat sharpen the minimum in the bulk water solubility curves shown above and move them to higher water contents. It would not, however, change the general shape of the curves or the position of the inferred boundaries of the asthenosphere. The effect of using different experimental data for water solubility in olivine as well as the effect of changing the ratio of orthopyroxene to olivine is further discussed in (21).



Lars's lecture: temperature effect could explain lowering of  $V_s$ ; if melt is induced does it wet grain boundaries?

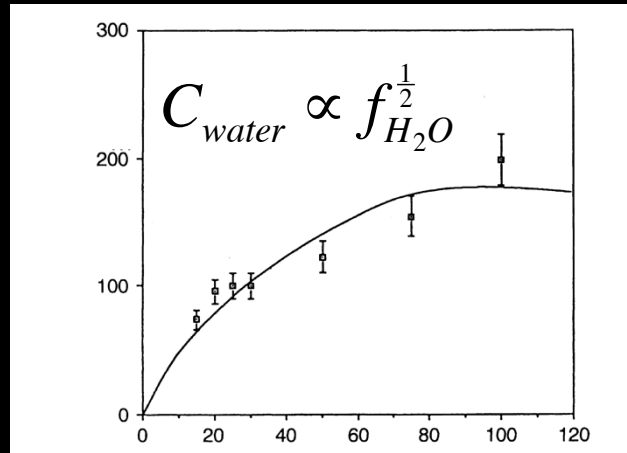
Mierdel *et al.*, 2007

# Garnet (Pyrope)



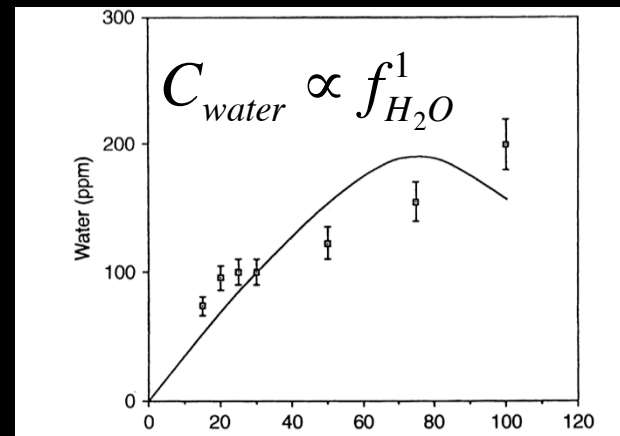


# Solubility of water- Pyrope: Which site?



*Interstitial or coupled substitution*

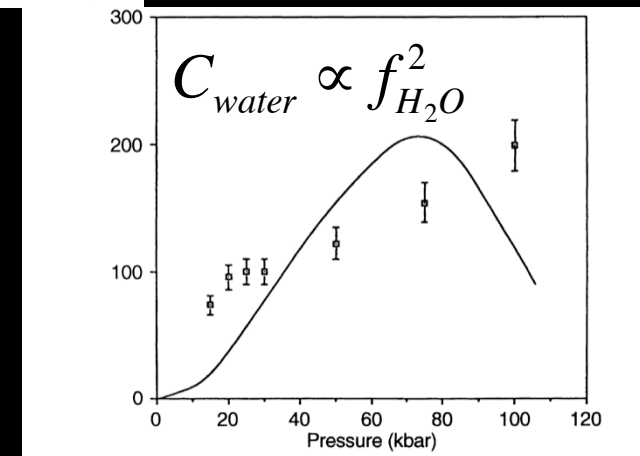
*Mg site*



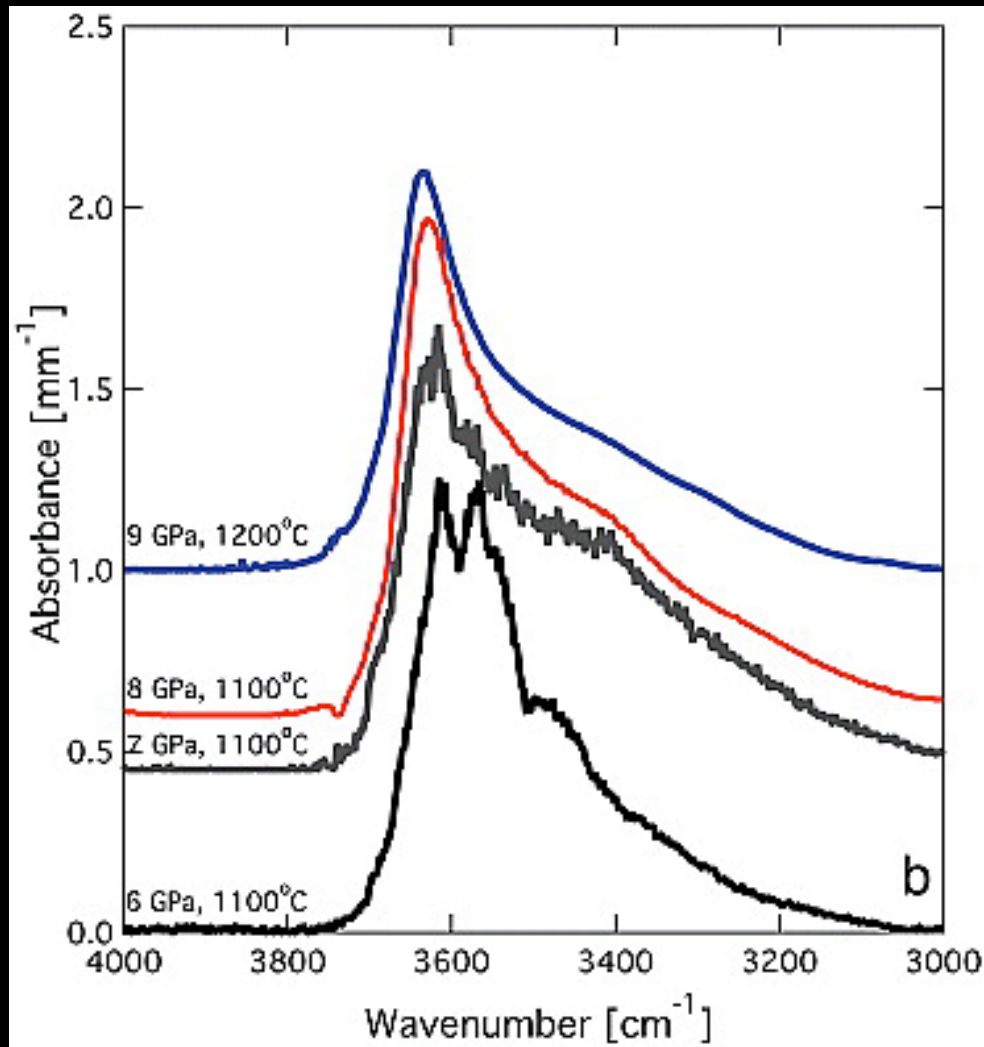
$$C_{water} = A f_{H_2O}^n \times \exp \left[ -\frac{\Delta H + P \Delta v}{RT} \right]$$

*Si site: "hydrogarnet"*

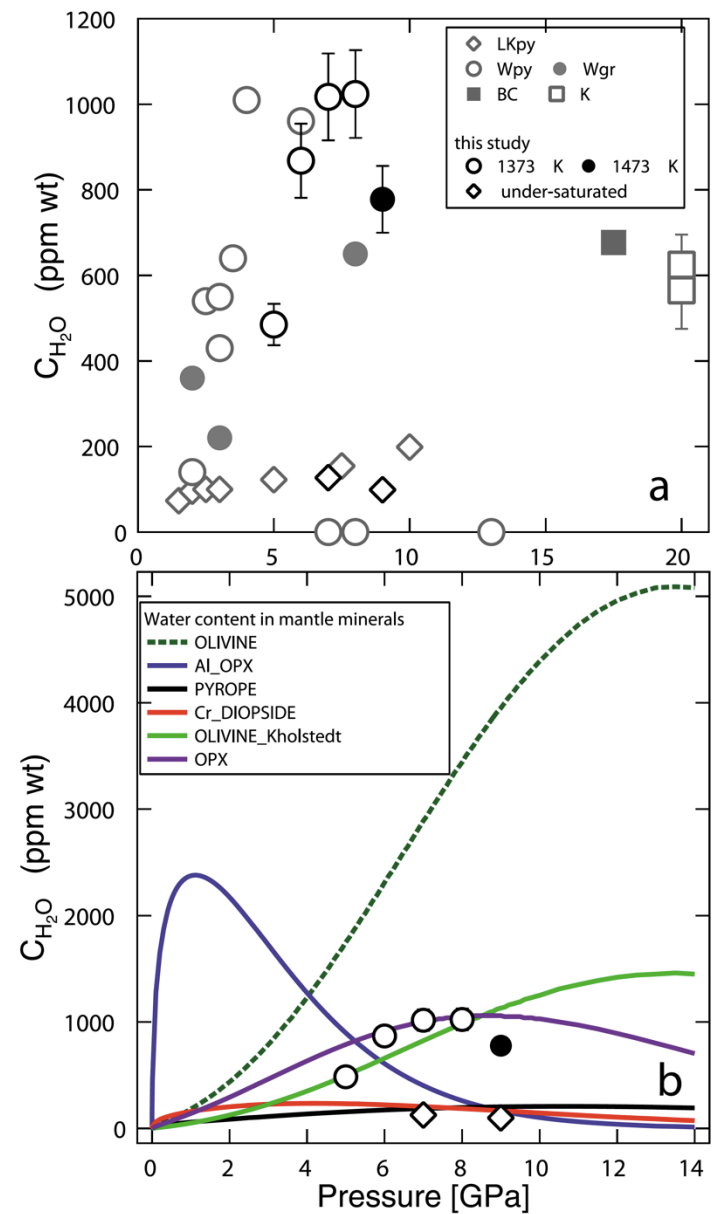
*Lu and Keppler (1997)*



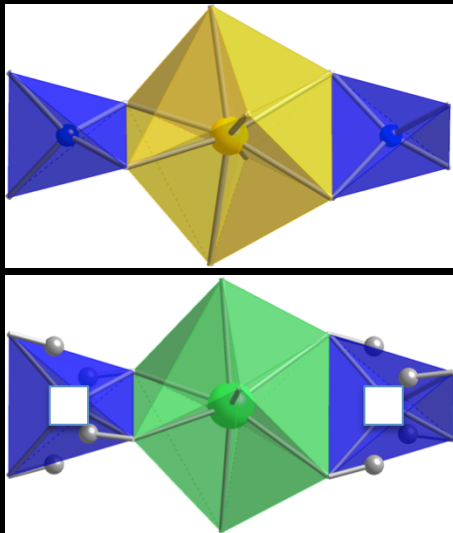
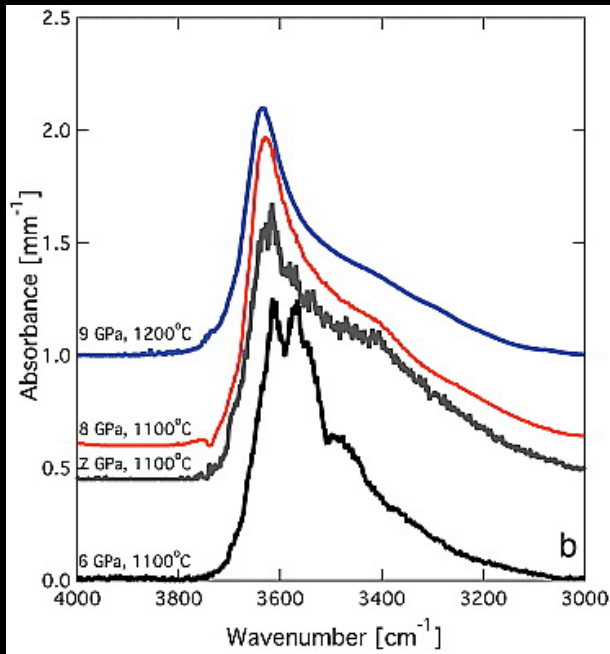
# Solubility of water: Garnet



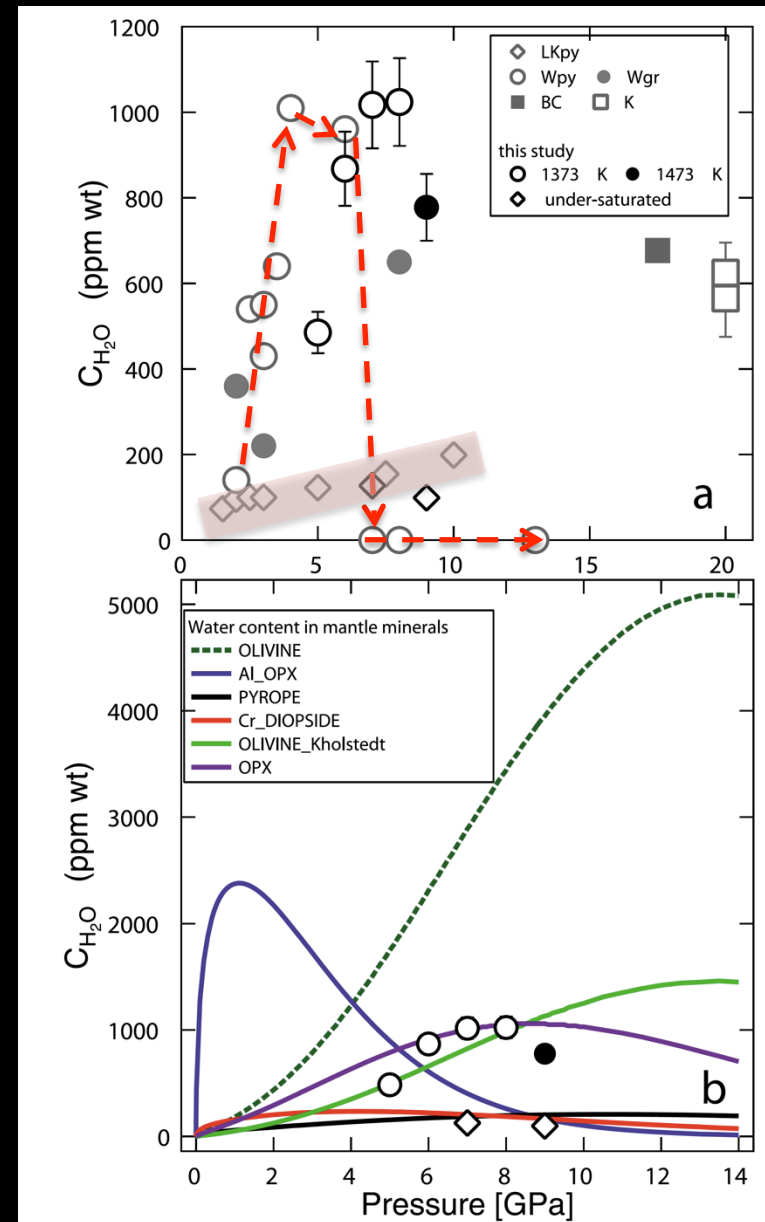
Mookherjee & Karato (2010)



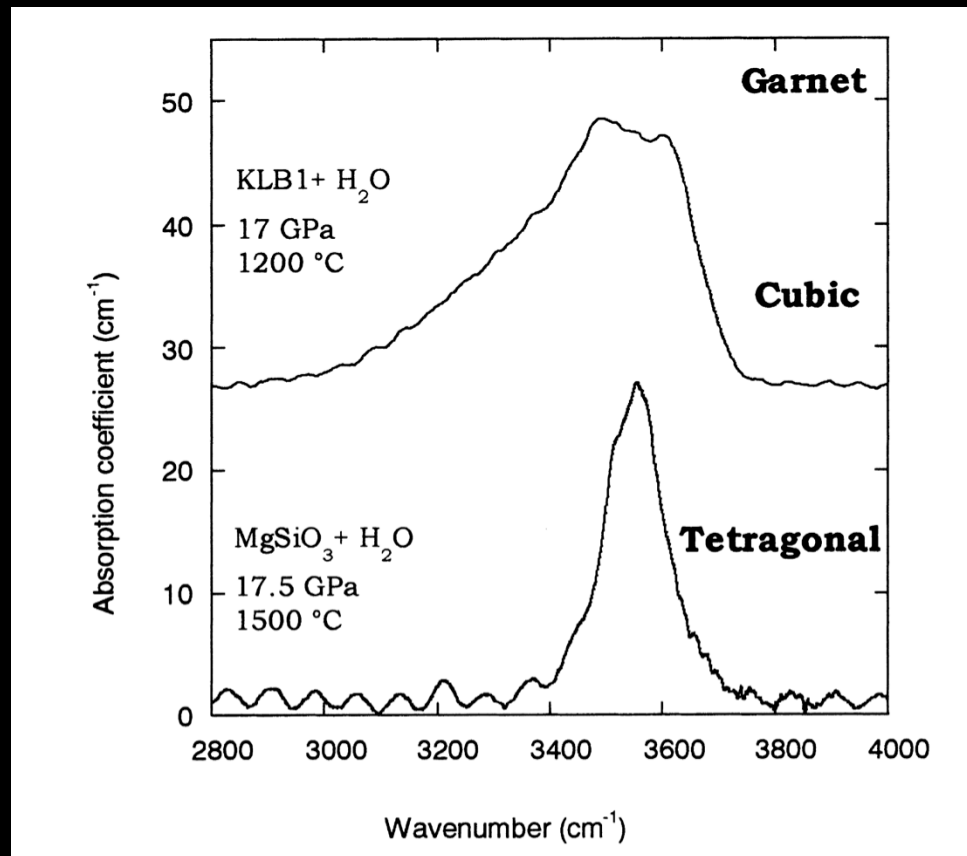
# Solubility of water: Garnet



Mookherjee & Karato (2010)

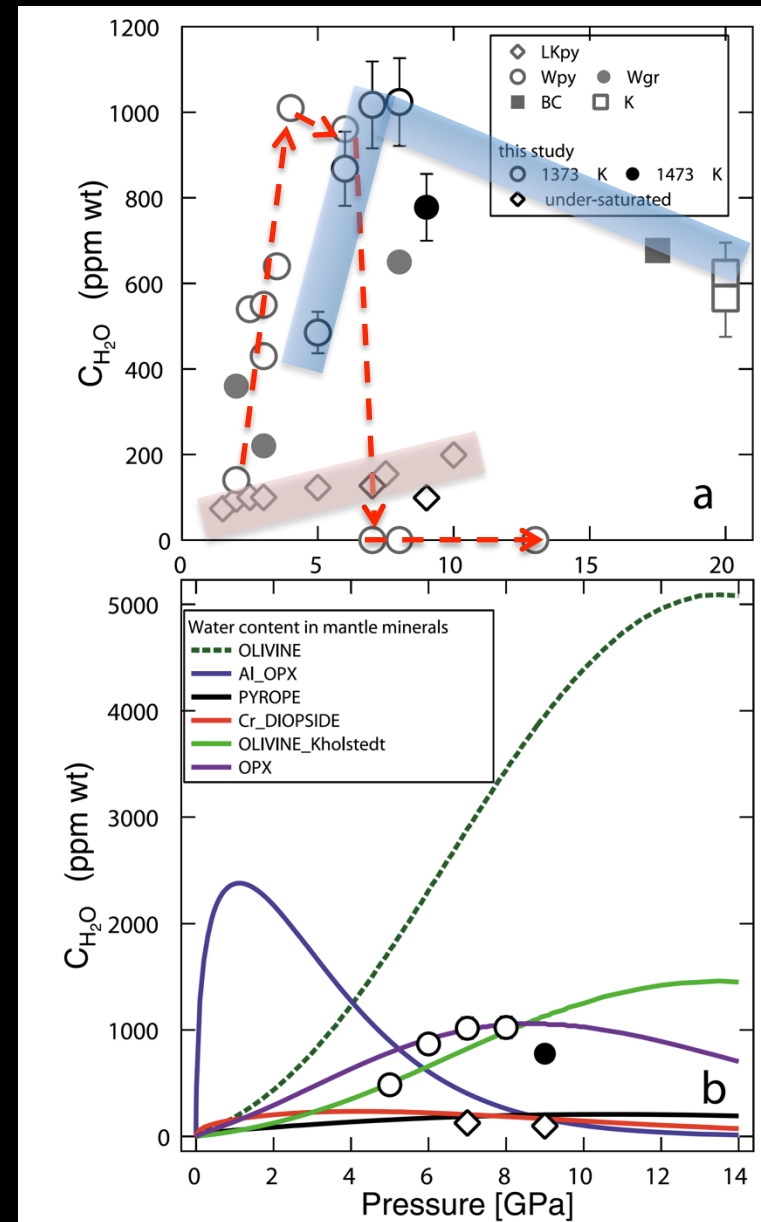


# Solubility of water: Garnet (majorite)

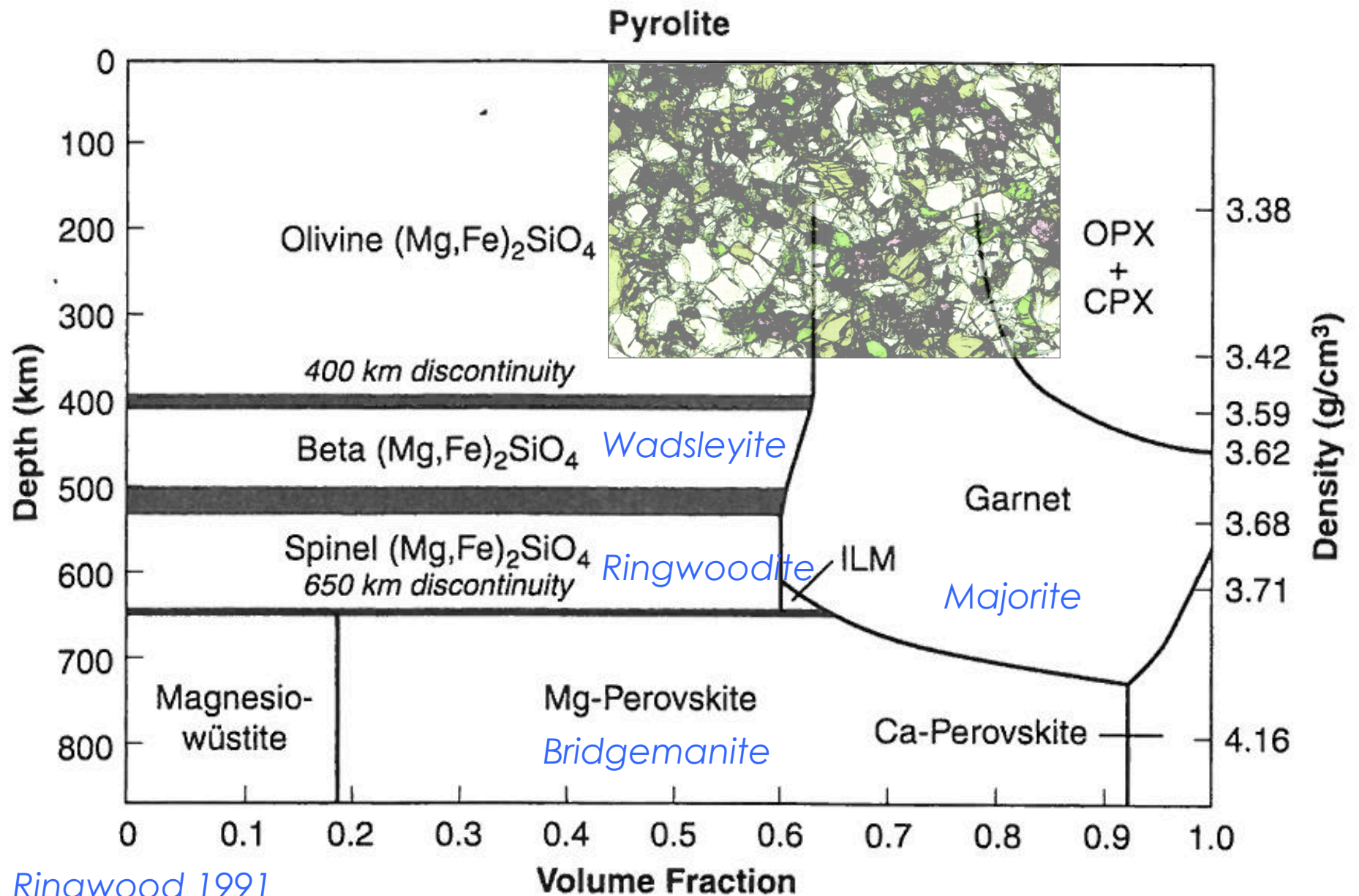


Majorite:  
Bolfan-Casanova et al. 2000

Mookherjee & Karato (2010)



# Mineralogy of the Transition Zone



Ringwood 1991

# NAMs Transition Zone: Wadsleyite

Tetrahedral units share corners  
Dimers: *sorosilicates*

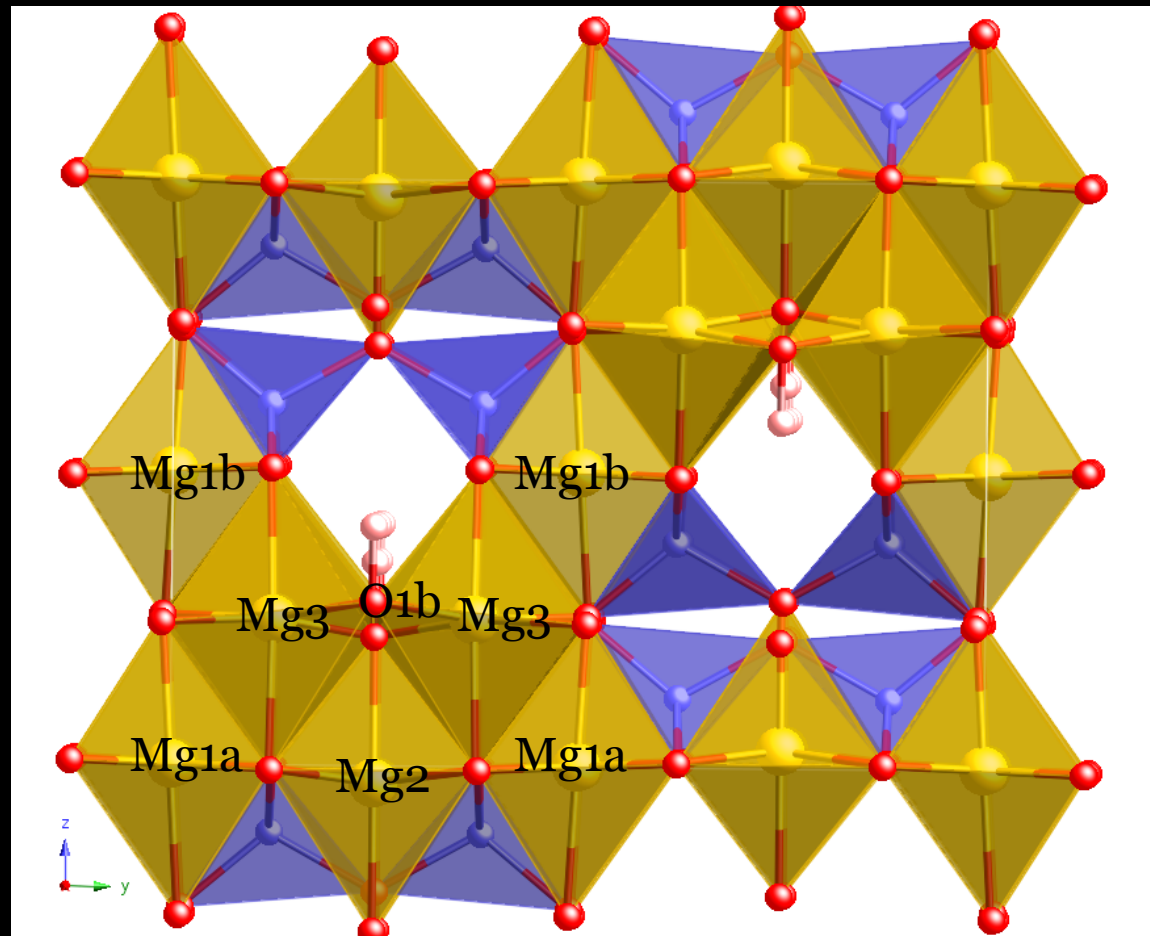
*Underbonded oxygen (O1b)*  
O1b forms bond with 5 Mg ions, Mg2, and four Mg3.

Mg has 2+ charge and bonds to 6 Oxygen ions.

Hence, O1b received 2/6 electrons from each of five Mg = +5/3

This is not balanced by an effective charge of  $O^{2-}$  hence it O1b is under bonded and a site where hydrogen attaches readily.

Smyth (1994)



# Solubility of water: Temperature dependence

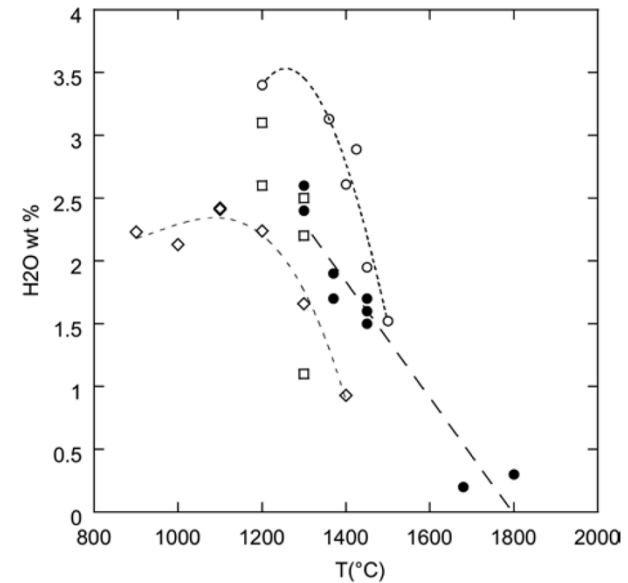
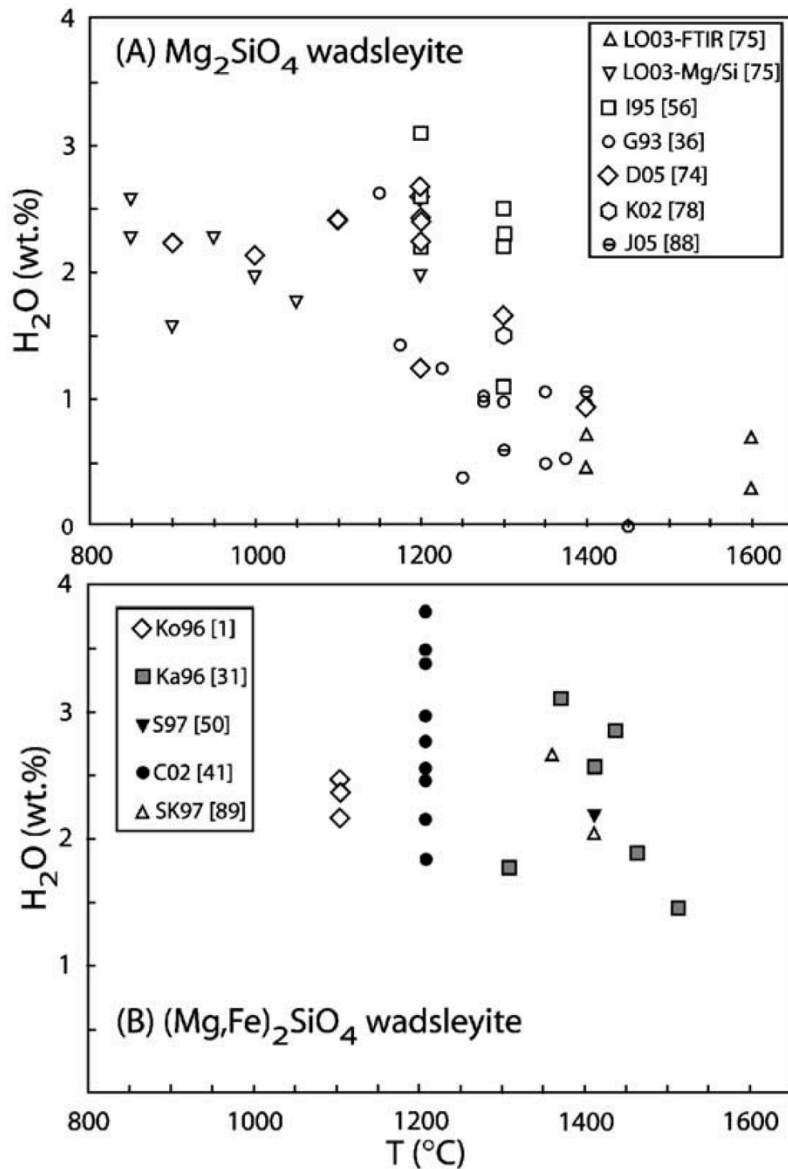


**Figure 15.** SIMS derived water contents as a function of temperature for pure  $Mg_2SiO_4$  wadsleyite (Inoue et al. 1995: open squares; Demouchy et al. 2005: open diamonds);  $(Mg,Fe)_2SiO_4$  wadsleyite in the KLB-1 system (Kawamoto et al. 1996: open circles); and pure  $Mg_2SiO_4$  ringwoodite (Ohtani et al. 2000: filled circles). The decrease in water solubility above 1200 °C is due to a reduced water activity in the melt. Curves are a guide for the eye only.

*Keppler and Bolfan-Casanova (2006)*

*Hirschmann (2005)*

# NAMs Transition Zone: Ringwoodite

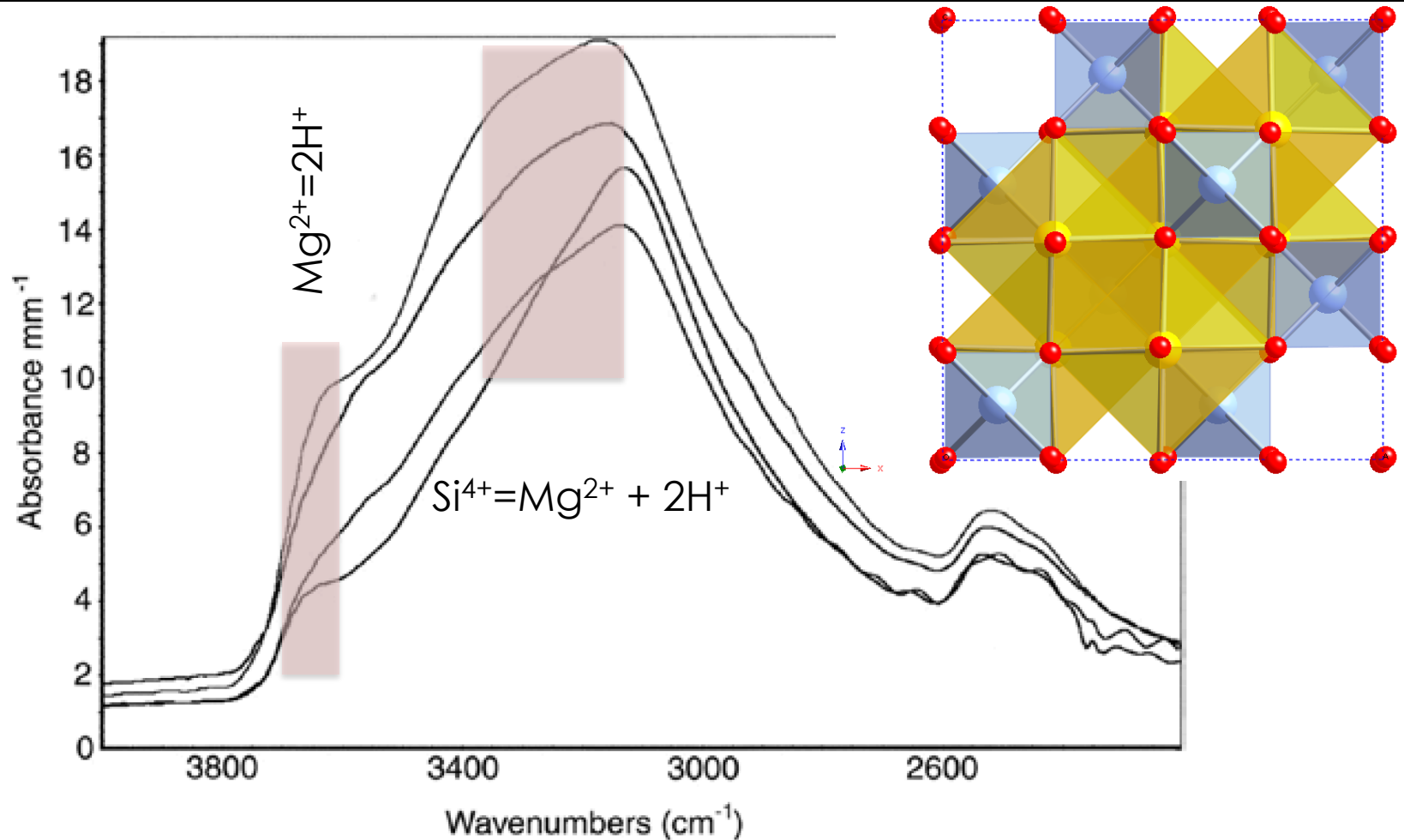


**Figure 16.** Infrared spectra of hydrous ringwoodite ( $\text{Fo}_{88-90}$ ) with up to 1 wt% water. The spectra shown here are characteristic for ringwoodite with low to moderate water content. At water contents of 2 wt% or above, there is a prominent band at  $3645 \text{ cm}^{-1}$  which is only present as a shoulder in the spectra shown here. From Smyth et al. (2003).  
*Keppler and Bolfan-Casanova (2006)*

# NAMs Transition Zone: Bridgemanite

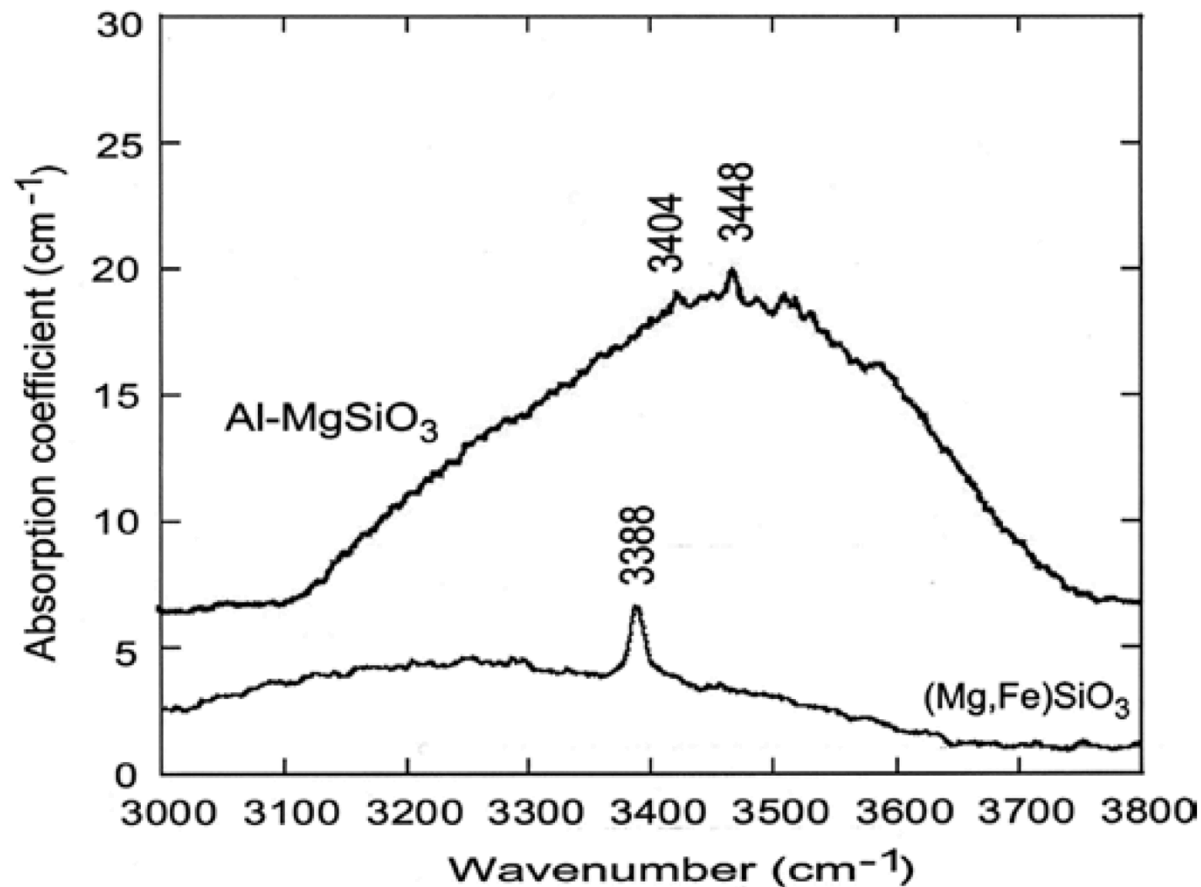
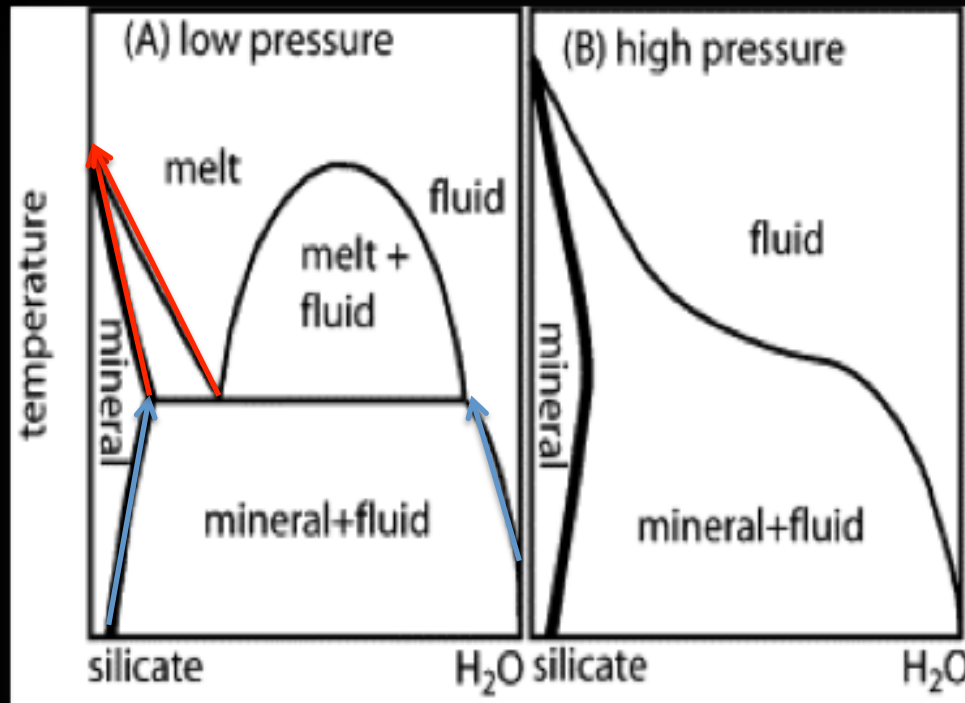


**Figure 19.** Infrared spectra showing the OH stretching region of perovskite ( $\text{Mg}_{0.98}\text{Fe}_{0.02}\text{SiO}_3$ ) after Bolfan-Casanova et al. (2003) and of  $(\text{Mg},\text{Si},\text{Al})\text{O}_3$  perovskite containing 4.4 wt%  $\text{Al}_2\text{O}_3$  after Litasov et al. (2003). Samples were synthesized at 25 GPa and 1400 and 1200 °C, respectively. The origin of the broad band is not fully understood, it may be related to inclusions of a separate phase.

# Solubility of water: Temperature dependence



*Hirschmann (2005)*



*HDAC experiments at Cornell  
Source: William A Bassett*

# Solubility of water: Estimates of Reservoir Sizes

$$C_{water}^{\alpha} = A_{\alpha} f_{H_2O}^{n\alpha} \times \exp \left[ -\frac{\Delta H_{\alpha} + P\Delta v_{\alpha}}{RT} \right]$$

$$C_{water}^{\beta} = A_{\beta} f_{H_2O}^{n\beta} \times \exp \left[ -\frac{\Delta H_{\beta} + P\Delta v_{\beta}}{RT} \right]$$

$$D_{water}^{\alpha/\beta} = \left( \frac{A_{\alpha}}{A_{\beta}} \right) \left( \frac{f_{H_2O}^{n\alpha}}{f_{H_2O}^{n\beta}} \right) \times \exp \left[ -\frac{(\Delta H_{\alpha} - \Delta H_{\beta}) + P(\Delta v_{\alpha} - \Delta v_{\beta})}{RT} \right]$$

Please recall  
Chrystle's talk

**Table 4.** A model for the equilibrium distribution of water in the mantle.

Reservoir	Mass fraction of the Earth	Water content (ppm by weight)	Mass of water ( $10^{20}$ kg H <sub>2</sub> O)	% of ocean mass
Upper mantle	0.103	~ 250	1.54	11
Transition zone	0.075	~ 1400	6.27	45
Lower mantle	0.492	~ 10	0.29	2

From Bolfan-Casanova (2000); mass of the Earth =  $5.97 \times 10^{23}$  kg, mass of the oceans =  $1.4 \times 10^{21}$  kg

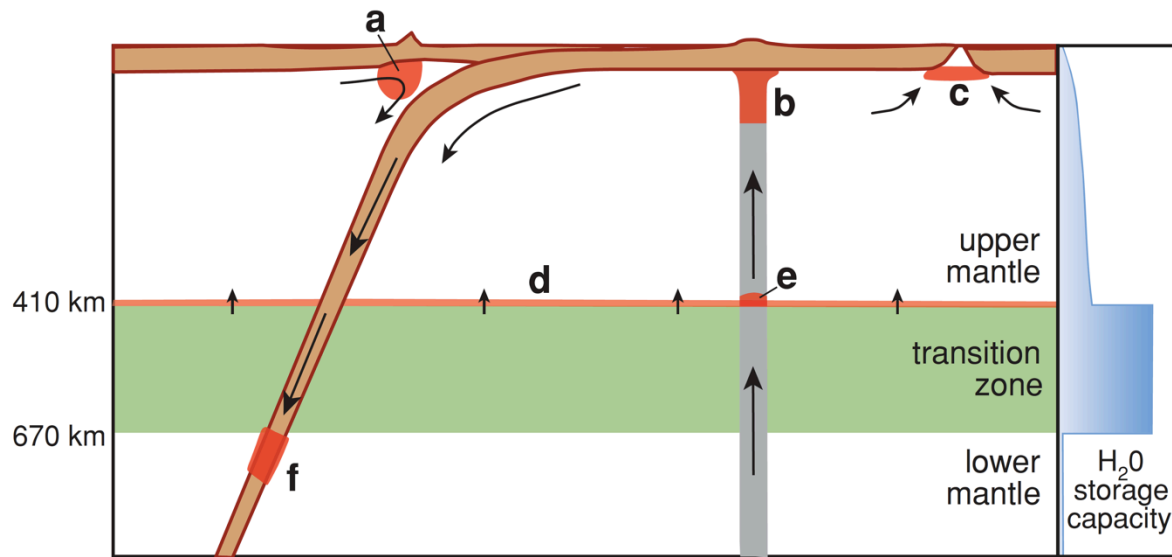
*Keppler and Bolfan-Casanova (2006)*

**Table 3.** Experimentally determined partition coefficients of water among minerals of the lower mantle and the transition zone.

<i>P</i> (GPa)	<i>T</i> (°C)	Phase assemblage	Partition coefficient
----- <i>System MgO – SiO<sub>2</sub> – H<sub>2</sub>O</i> -----			
15	1300	Wads + Cen + melt	$D^{\text{Wadsleyite/Clinoenstatite}} \sim 3.8$
15	1500	Cen + Stish + melt	$D^{\text{Clinoenstatite/Stishovite}} \sim 8.2$
17.5	1500	Maj + Stish + melt	$D^{\text{Majorite/Stishovite}} \sim 270$
19	1200	Ringw + Stish	$D^{\text{Ringwoodite/Stishovite}} \sim 521$
19	1300	Ringw + Akim + Stish + melt	$D^{\text{Ringwoodite/Akimotoite}} \sim 21$
21	1500	Akim + Stish + melt	$D^{\text{Akimotoite/Stishovite}} \sim 18$
24	1600	Perov + Akim + Stish + melt	$D^{\text{Akimotoite/Perovskite}} \gg 1$
24	1500	Pe + Perov + melt	$D^{\text{Periclase/Perovskite}} > 1$
----- <i>System MgO – FeO – SiO<sub>2</sub> – H<sub>2</sub>O</i> -----			
24	1400	Ringw + Perov	$D^{\text{Ringwoodite/Perovskite}} \sim 1050$
24	1400	Ringw + Perov + Fe-Pe + melt	$D^{\text{Ringwoodite/Perovskite}} \sim 1400$
			$D^{\text{Ferropericlase/Perovskite}} \sim 60$

Wads = wadsleyite, Cen = clinoenstatite, Stish = stishovite, Maj = majorite, Ring = ringwoodite, Akim = akimotoite, Perov = MgSiO<sub>3</sub> perovskite, Fe-Pe = ferropericlase. After Bolfan-Casanova et al. (2000) and Bolfan-Casanova et al. (2003).

# Water in NAMs: Lower Mantle (?)



## Melt410

(Bercovici & Karato, 2003;  
Matsukage et al., 2005;  
Sakamaki et al., 2006; Agee,  
2008; Mookherjee, Stixrude,  
Karki, 2008; Tauzin et al., 2010)

Melt660 (Hirschmann, 2006;  
Schmandt et al. 2014)

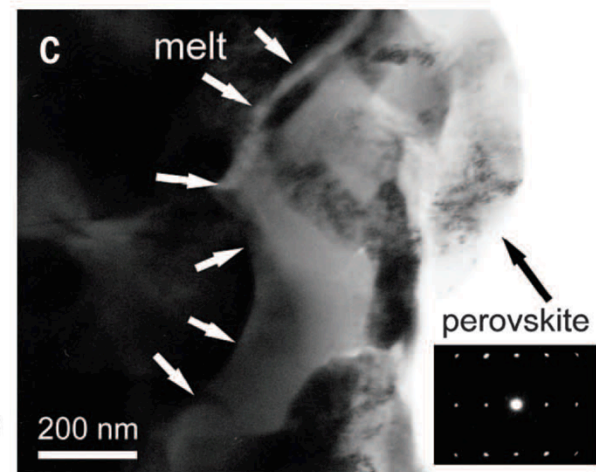
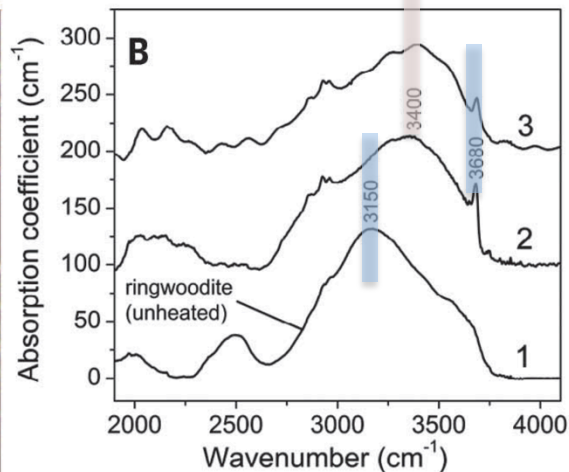
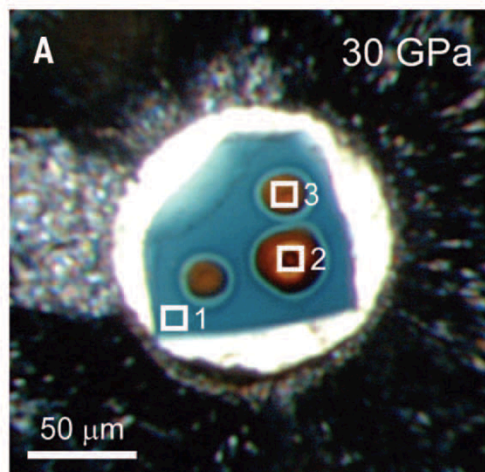
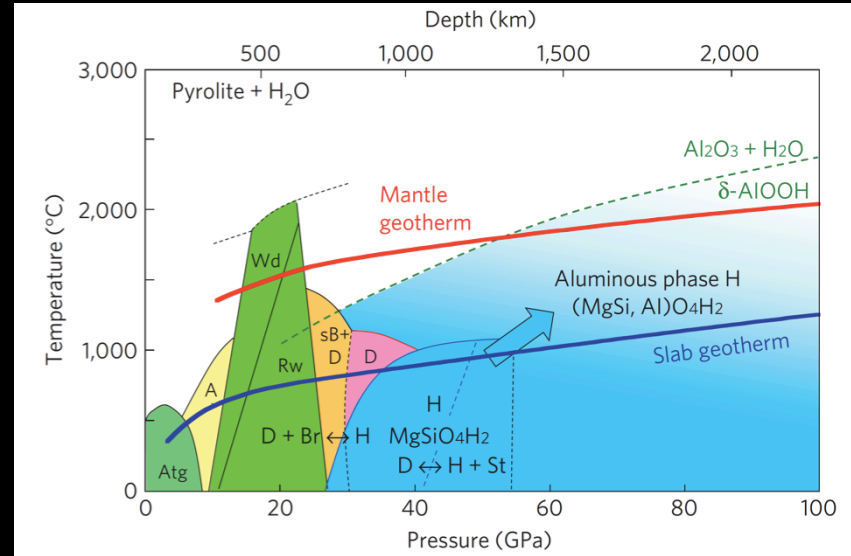
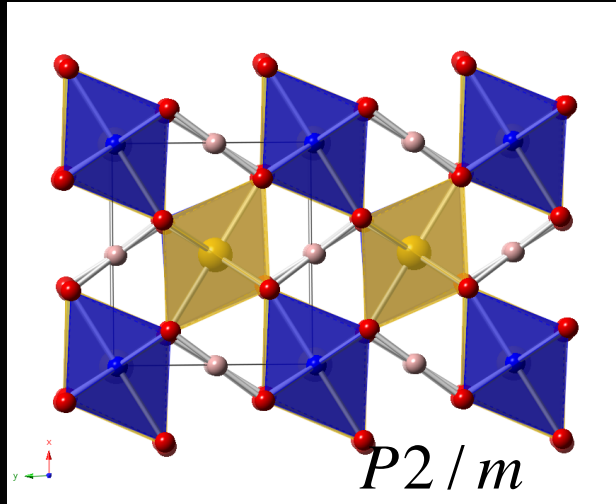
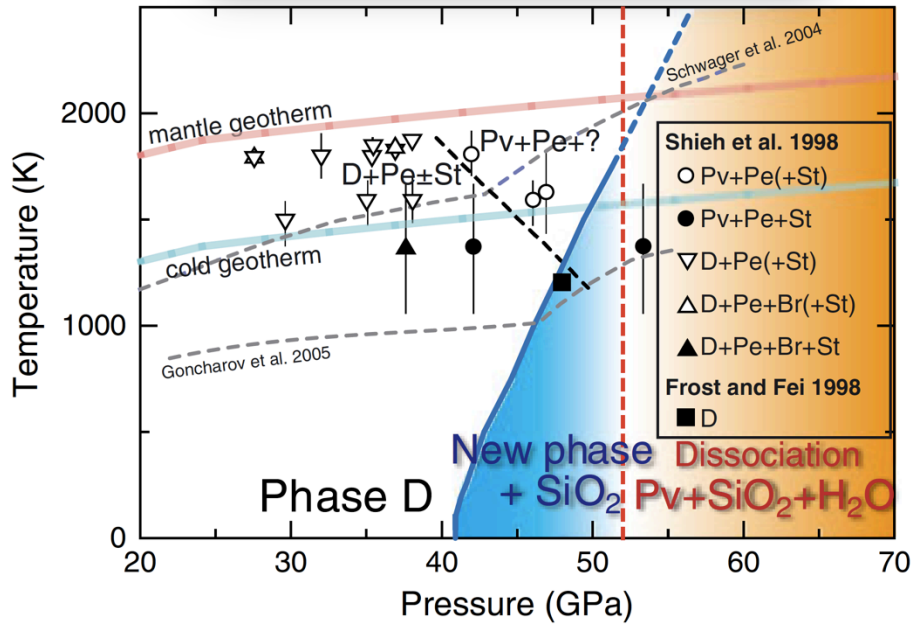


**Fig. 1. Laboratory experiments on hydrous ringwoodite.** (A) Single-crystal of hydrous ringwoodite (blue crystal) containing 1 wt % H<sub>2</sub>O inside a DAC at 30 GPa. The sample was laser heated to 1600°C in several spots (orange circles) to perform direct transformation to perovskite and (Mg,Fe)O. (B) Synchrotron-FTIR spectra of the recovered sample in three locations: an unheated part of the crystal (spectrum 1) and two locations within laser-heated spots (spectra 2 and 3). FTIR spectra were collected with a 10 μm by 10 μm aperture, illustrated and numbered by white boxes in (A). (C) TEM within a laser-heated spot (position 2) shows crystals of perovskite and intergranular amorphous quench (melt).

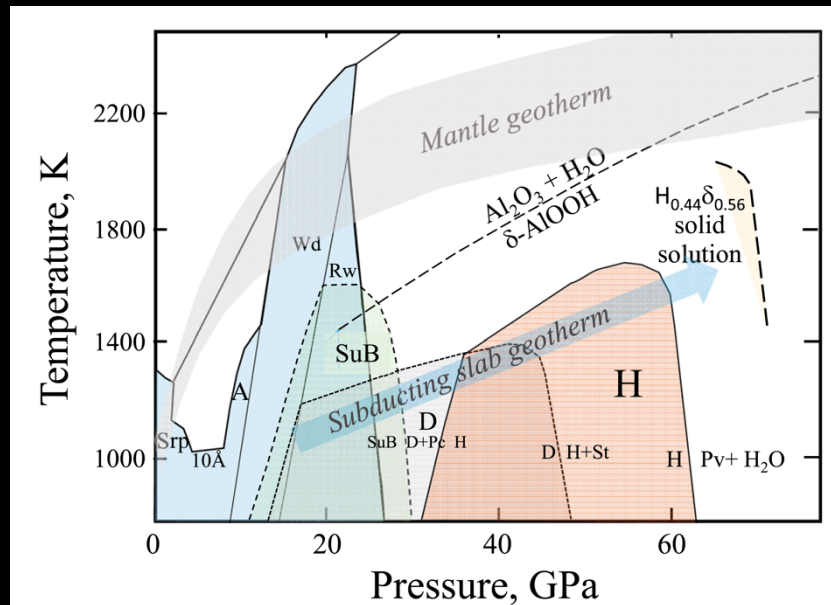
# Dense Hydrous Mineral: Phase H



Nishi et al (2014) Ohtani et al (2014)

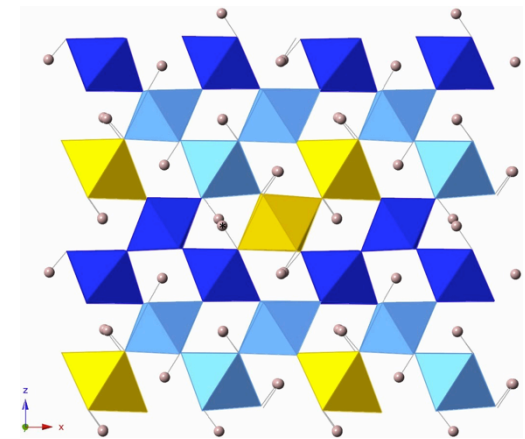
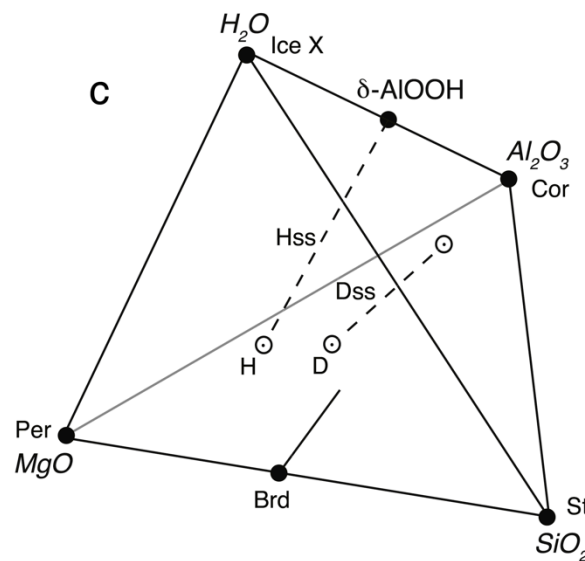
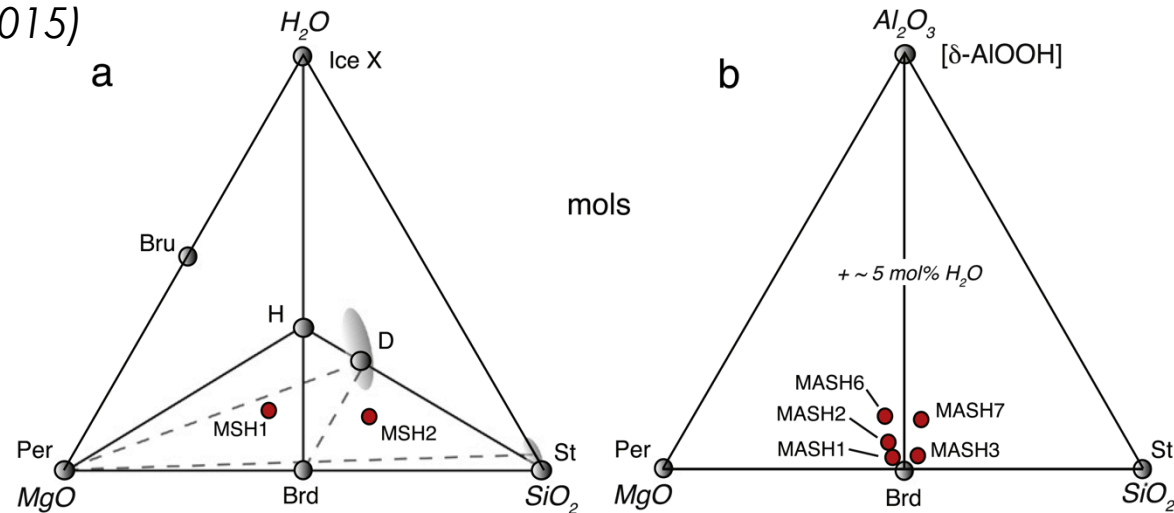


Tsuchiya (2013)



# High P-T stability: Phase H

Walter et al. (2015)



Panero & Caracas (2017)

**Fig. 1.** Starting compositions in the (a) MSH and (b) MASH systems used in this study. Compositions in the MASH system are projected from  $H_2O$ . Figure (c) shows the MASH quaternary with the compositions of hydrous and anhydrous phases relevant to the deep mantle. Per = periclase; Brd = bridgmanite; St = stishovite; Bru = brucite; D = phase D; Dss = phase D solid solution; H = phase H; Hss = phase H solid solution; IceX = high pressure form of water ice. Shown on (a) are some possible relevant tie lines between phases in the MSH system.

# High P-T stability: Phase H

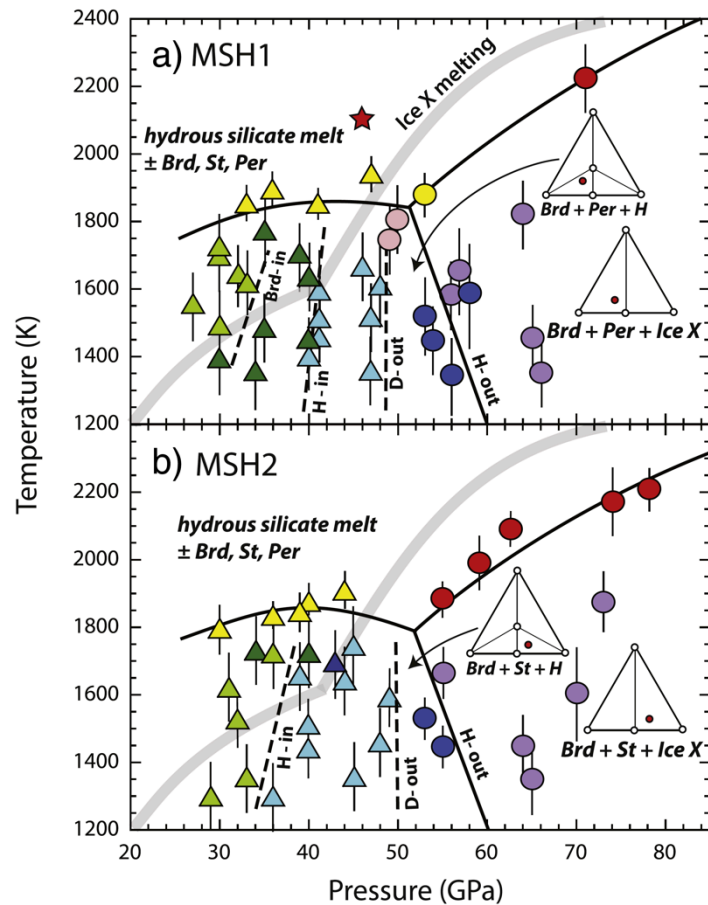


**Fig. 4.** Pressure–temperature diagram showing the experimental phase relations observed for compositions MSH1 (a) and MSH2 (b). Triangles represent experiments containing phase D and circles are phase D absent. Light green = D + Per + St; dark green = D + Brd + Per + St; light blue = H + D + Brd ± Per, St; dark blue = Brd + H ± St, Per; purple = Brd ± Per, St + IceX (inferred); light yellow = ramp experiments containing phase D and/or phase H; red = ramp experiments with no observable hydrous phase; pink = Brd + St + Per. The red star is a supra-liquidus experiment heated above the temperature plateau. The IceX melting curve is from Schwager and Boehler (2008). Insets show three-phase triangles in MSH as labeled in Fig. 1.

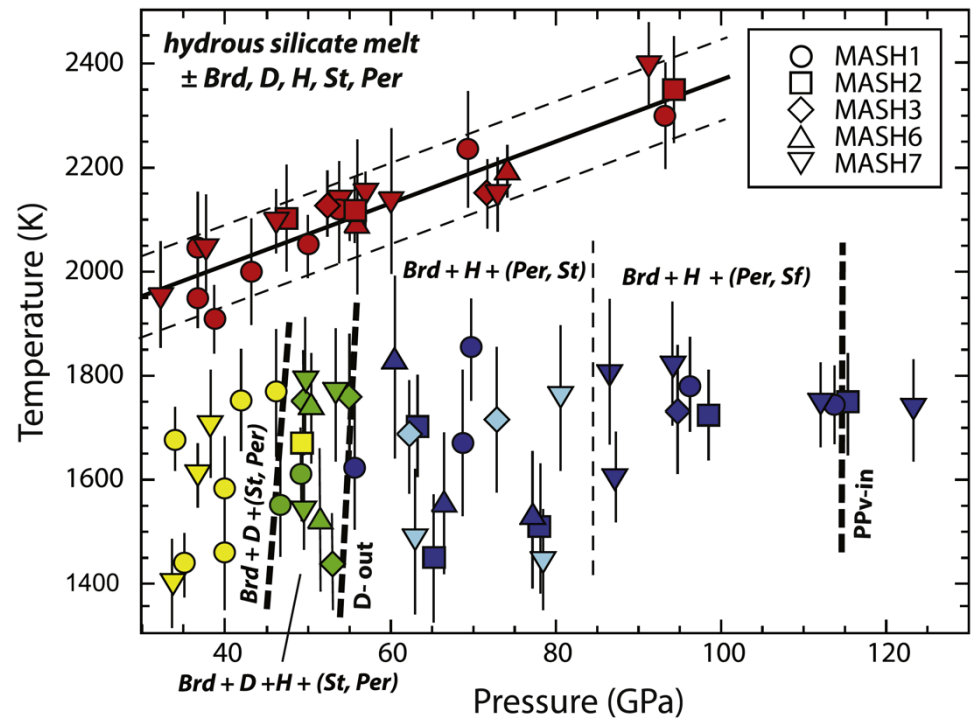


**Fig. 7.** Pressure–temperature diagram showing the experimental phase relations observed for compositions in the MASH system. Symbol shapes correspond to different bulk compositions as shown in the legend. Symbol colors are as follows: yellow = phase D-bearing but phase H absent; light green = phase D and H coexisting in the assemblage; light blue = Brd + H + St; dark blue = Brd + H ± Per; red = ramped experiments. The melting curve is defined as a linear fit to the data, with a slope of 6.1 K/GPa, and the thin dashed lines show  $2\sigma$  uncertainty on the fit. Phase labels as in Fig. 1.

Walter et al. (2015)

# 4. Physical Properties

# Seismic Velocity ( $V_P$ )

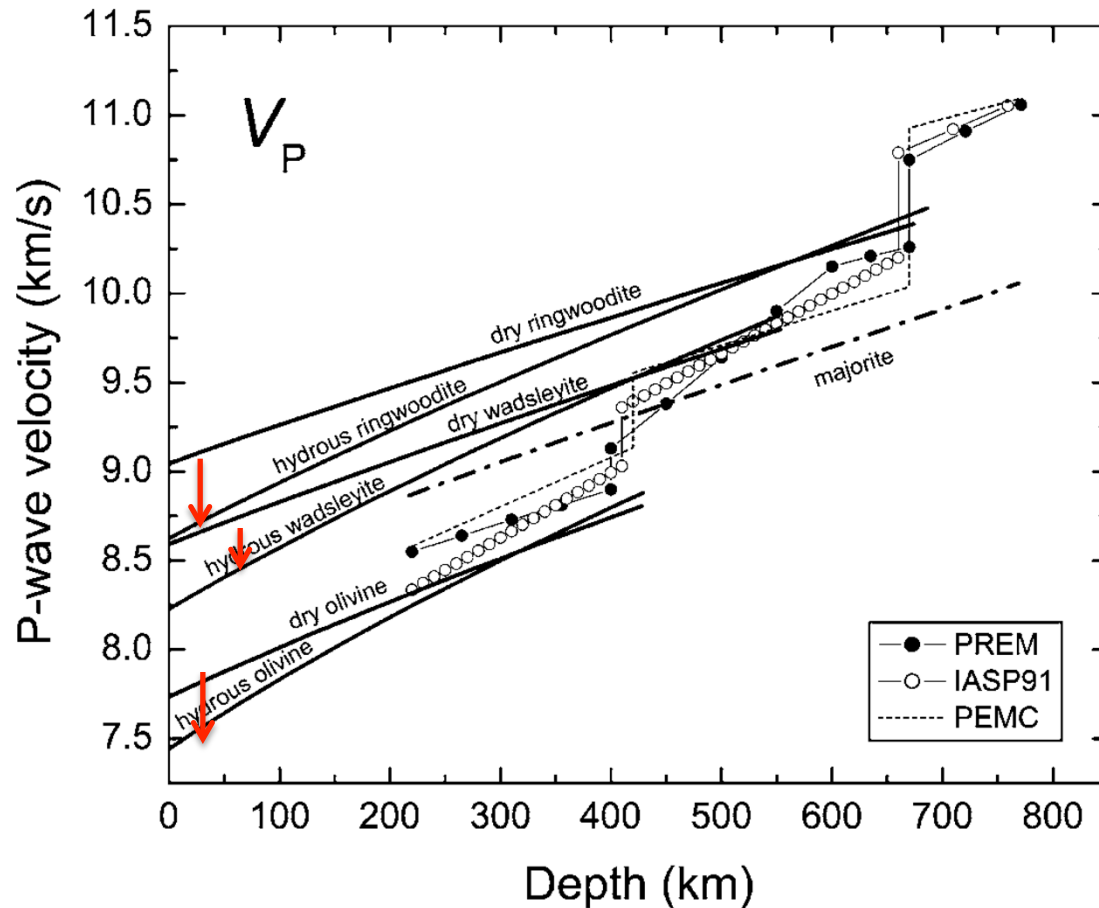


**Figure 4.** Monomineralic P-wave velocities for anhydrous (black lines) and hydrous ( $\sim 1$  wt%  $H_2O$ , grey lines) phases calculated along a 1673 K (foot) adiabat using finite strain equations of state and model parameters presented in Table 6. Also shown are estimated S-velocities for anhydrous majorite (dash-dotted line). See text for details.

Jacobsen (2006)

# Seismic Velocity ( $V_s$ )

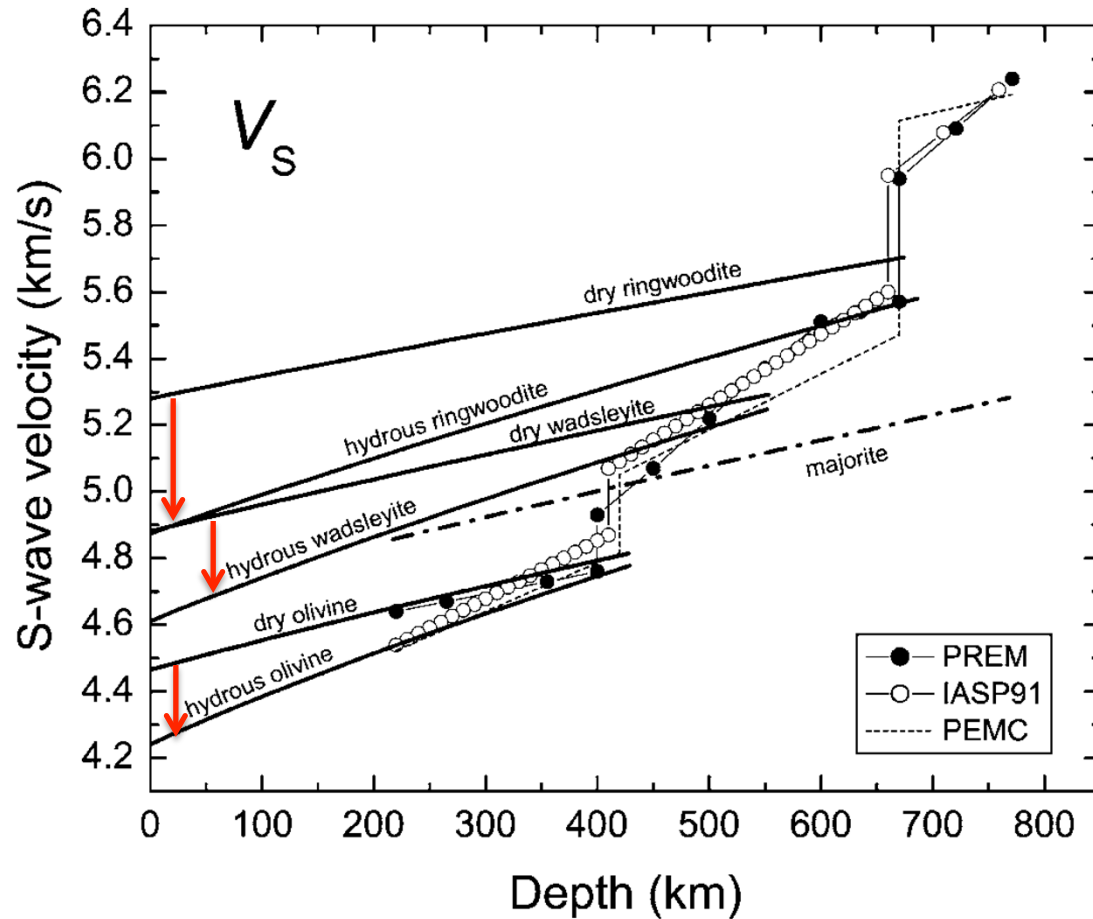


**Figure 5.** Monomineralic S-wave velocities for anhydrous (black lines) and hydrous (~1 wt% H<sub>2</sub>O, grey lines) phases calculated along a 1673 K (foot) adiabat using finite strain equations of state and model parameters presented in Table 6. Also shown are estimated S-velocities for anhydrous majorite (dash-dotted line) See text for details.

Jacobsen (2006)

# Effect of water: $V_P$ & $V_S$ of olivine

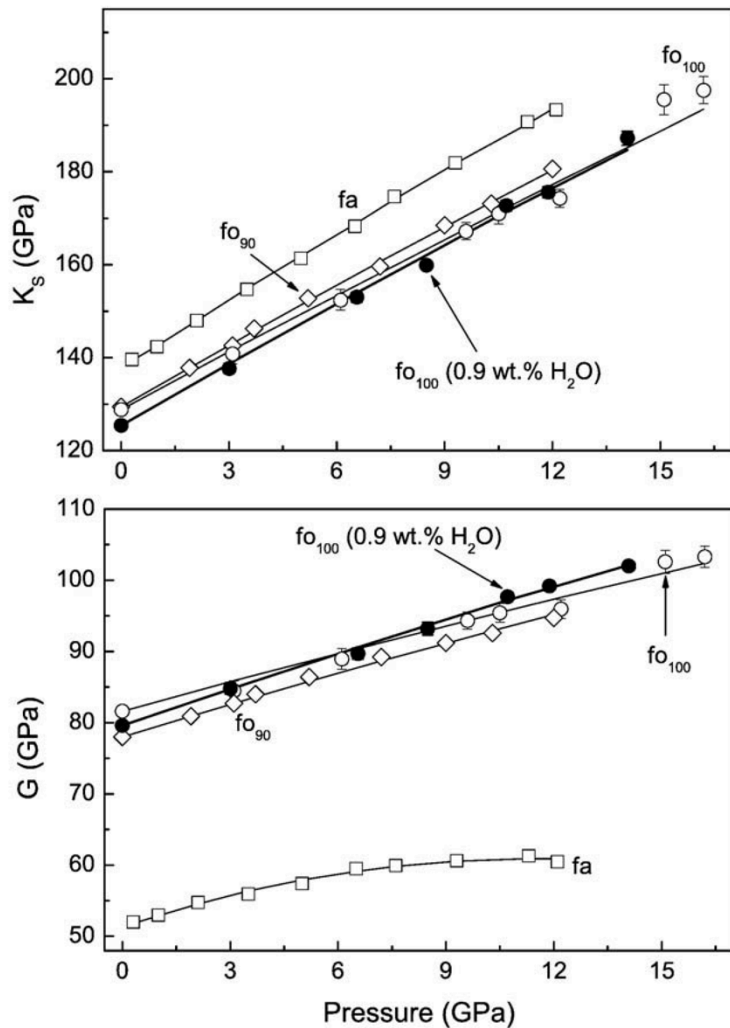


Fig. 3. Aggregate elastic moduli of forsterite as a function of pressure. Solid circle: hydrous forsterite ( $fo_{100}$ ,  $Mg_2SiO_4$ ), this study; open circle: anhydrous forsterite (Zha et al., 1996); diamond: Fe-bearing anhydrous forsterite ( $fo_{90}$ ,  $(Mg_{0.9}Fe_{0.1})_2SiO_4$ ) (Abramson et al., 1997); square: fayalite (fa,  $Fe_2SiO_4$ ) (Speziale et al., 2004).

Mao et al. (2010)

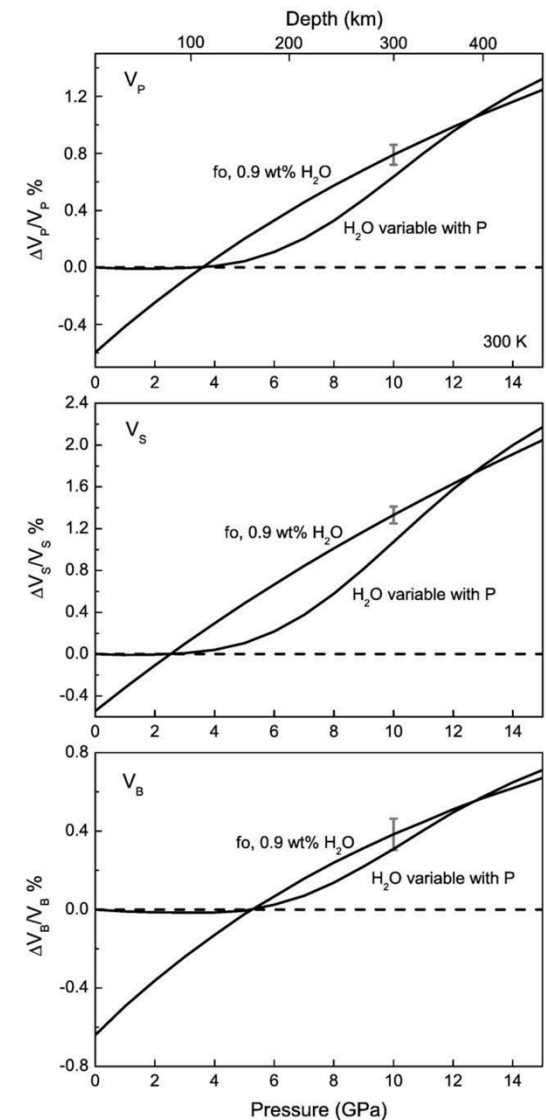
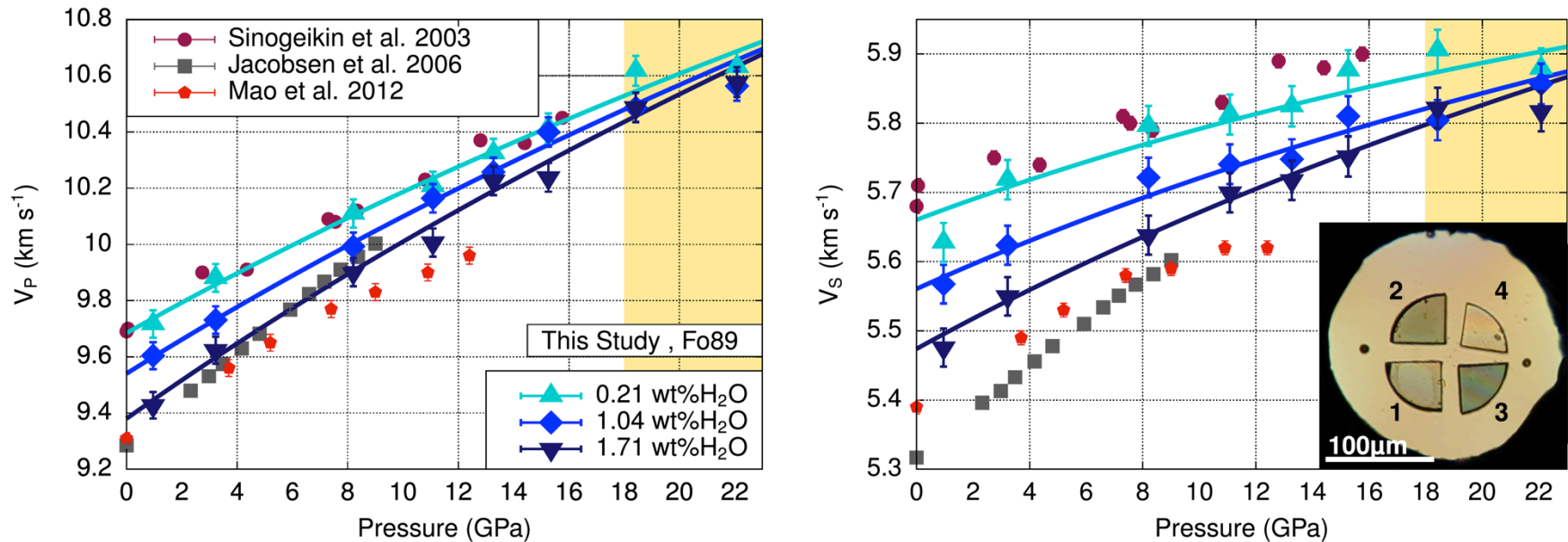


Fig. 5. Velocity change of forsterite caused by hydration relative to dry forsterite with pressure.  $\Delta V_x/V_x$  is  $(V_x^{hy} - V_x^{dry})/V_x^{dry}$ , where X is P, S or B for compressional, shear and bulk velocity, respectively. Dashed line is for 0 reference. fo, 0.9 wt.%  $H_2O$ : hydrous forsterite containing 0.9 wt.%  $H_2O$ , and the constant water content with pressure; H<sub>2</sub>O variable with P: water content in forsterite varies with pressure according to (Hauri et al., 2006). Representative uncertainties ( $1\sigma$ ) are shown.

# Effect of water: $V_P$ & $V_S$ of wadsleyite



**Fig. 1.** Measured high-pressure acoustic wave velocities of  $(\text{Mg}_{0.89}\text{Fe}_{0.11})_2\text{SiO}_4$  ringwoodite in comparison to previously published work (Mao et al., 2012; Jacobsen and Smyth, 2006; Sinogeikin et al., 2003). The inset shows our experimental setup where we simultaneously measured three single-crystal samples of Fe-bearing ringwoodite and one Mg-ringwoodite to high pressures. Samples 1–3: Fe-bearing ringwoodites with 0.21(3), 1.04(11) and 1.71(18) wt.%  $\text{H}_2\text{O}$ . Sample 4:  $\text{Mg}_2\text{SiO}_4$  ringwoodite with 0.42(5) wt.%  $\text{H}_2\text{O}$  (Table 4 in supplementary material).

# Effect of water: $V_P$ & $V_S$ of wadsleyite

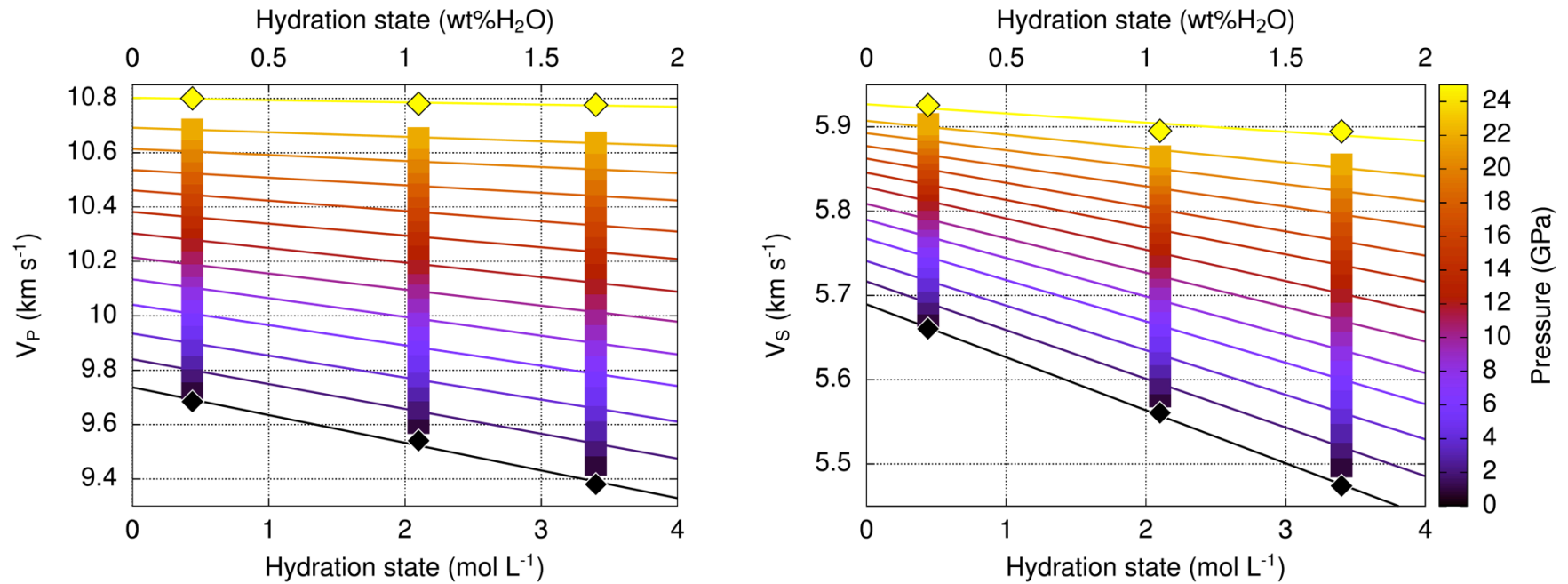


**Fig. 4.** Dependency of elastic wave velocities of  $(\text{Mg}_{0.89}\text{Fe}_{0.11})_2\text{SiO}_4$  ringwoodite on hydration state determined from our high-pressure measurements using the multi-sample approach. Experimental data points have been interpolated (squares) and extrapolated (diamonds) based on a finite strain formalism. A linear decrease of velocities with hydration is assumed. (For interpretation of the colours in the figure(s), the reader is referred to the web version of this article.)

# Effect of water: 410 Km

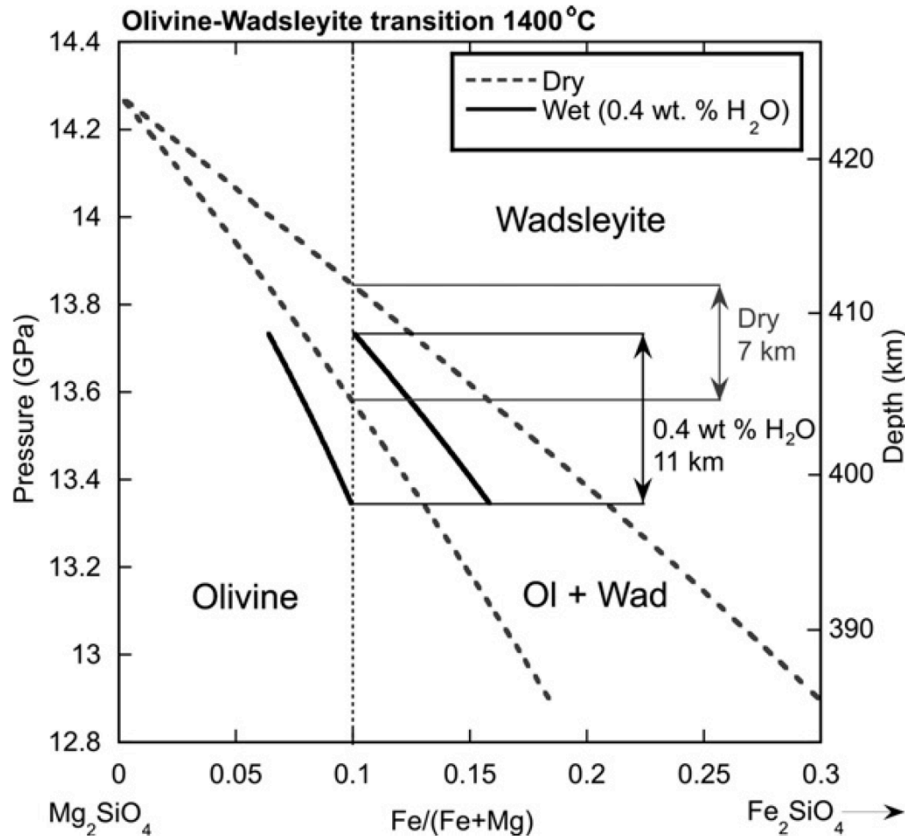
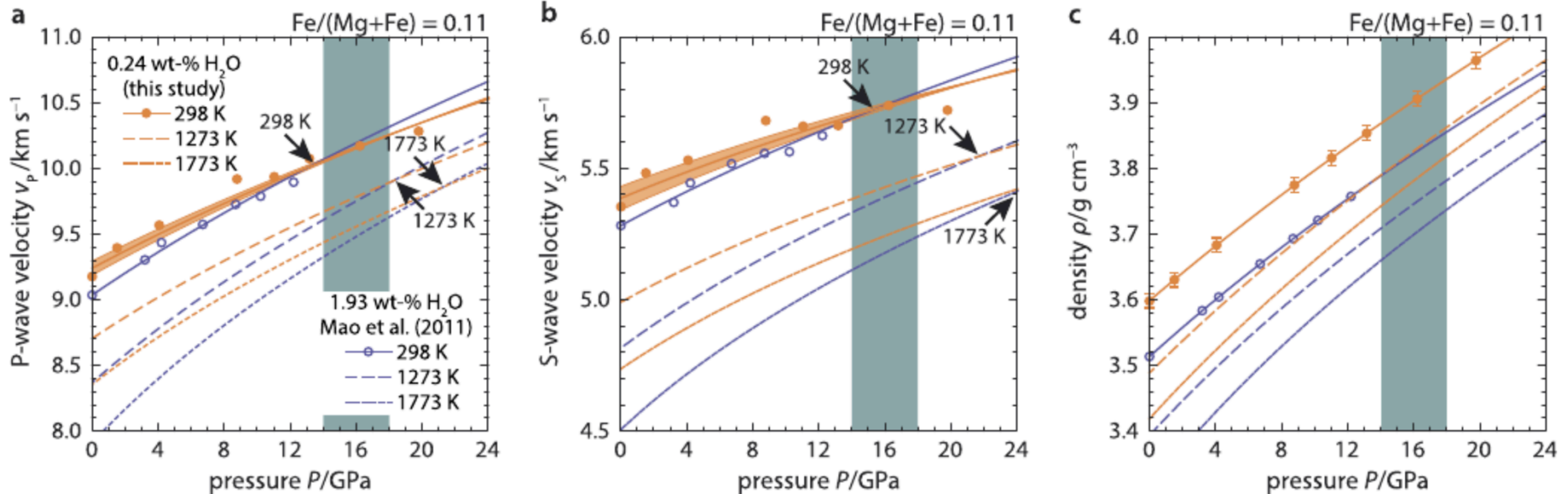


Fig. 6. The olivine–wadsleyite transformation in the  $Mg_2SiO_4$ – $Fe_2SiO_4$  system calculated at 1400 °C under anhydrous conditions and with 0.4 wt.%  $H_2O$ , which results in the broadest possible transition at this temperature. The vertical dashed line shows a typical mantle Fe/(Fe+Mg) ratio of 0.1. The addition of  $H_2O$  lowers the transition pressure, broadens the pressure interval of the transition and causes slight downward curvature of the two-phase region.

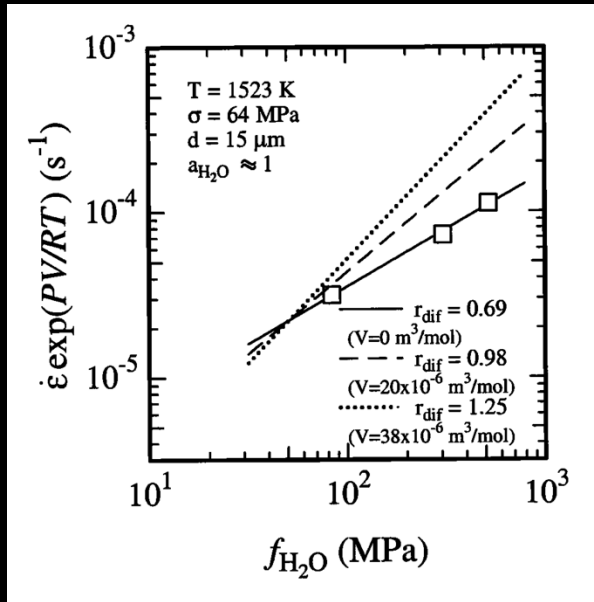
# Effect of water: $V_P$ & $V_S$ of Ringwoodite



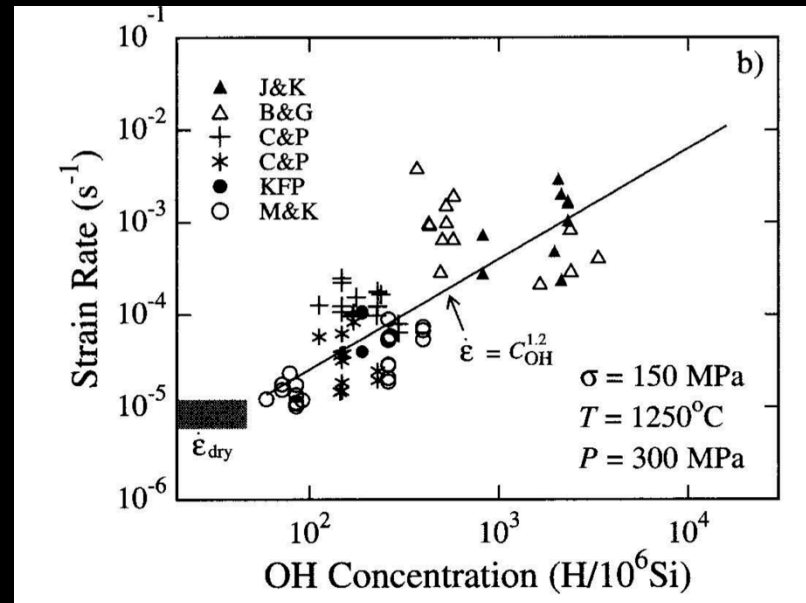
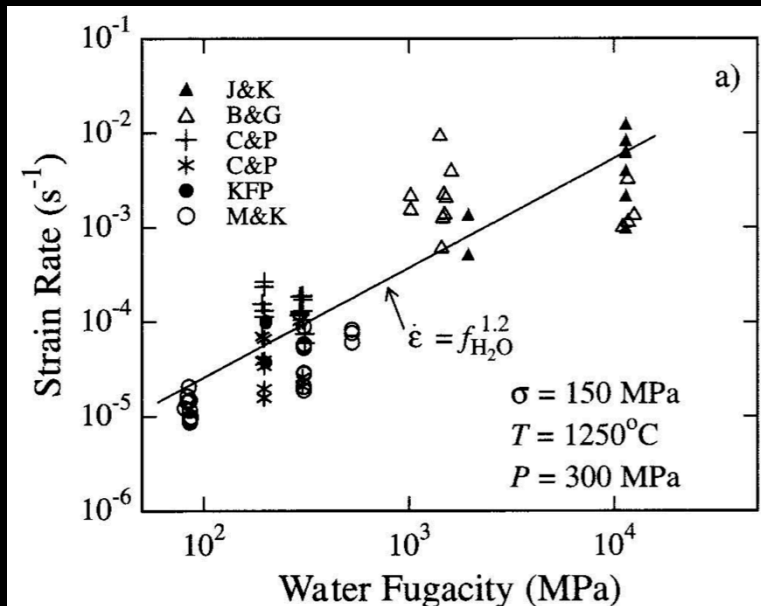
**Fig. 3.** Sound wave velocities for isotropic aggregates and densities of iron-bearing wadsleyite with  $\text{Fe}/(\text{Mg} + \text{Fe}) = 0.11$ . a) P-wave velocities, b) S-wave velocities, and c) densities of iron-bearing wadsleyite as a function of pressure at different temperatures. Black arrows mark the velocity cross-over points between less hydrous (0.24 wt-%  $\text{H}_2\text{O}$ , this study) and strongly hydrous (1.93 wt-%  $\text{H}_2\text{O}$ , Mao et al., 2011) iron-bearing wadsleyite at the indicated temperatures. Note the shift of velocity cross-over points to higher pressures with increasing temperature. Orange shading in a) and b) indicates the Voigt and Reuss bounds on the results of the present study. Green shaded regions mark the pressure range of wadsleyite stability in the transition zone. (For interpretation of the colors in the figure(s), the reader is referred to the web version of this article.)

# Effect of water: Transport Properties (NAMs)

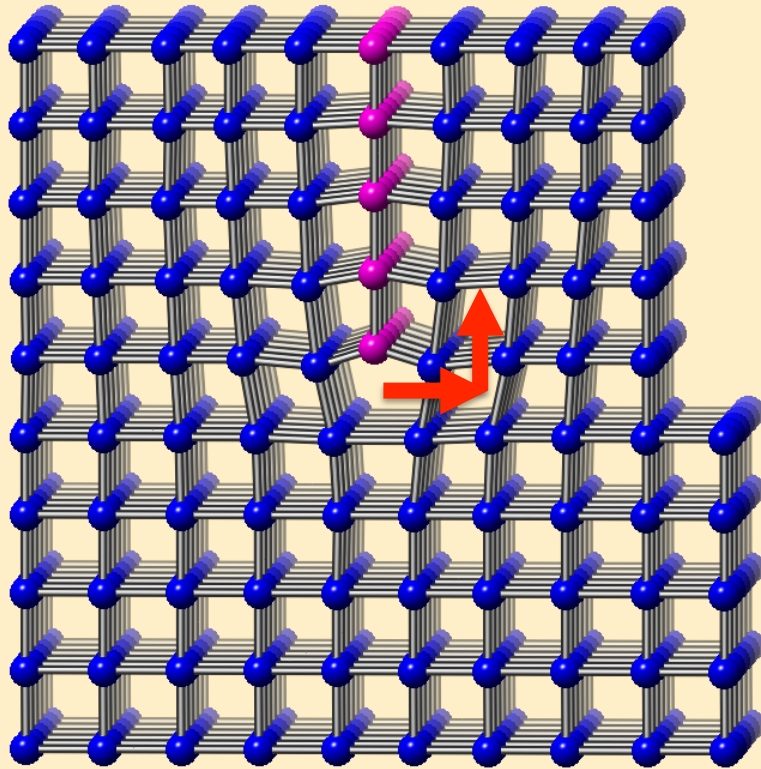
# Effect of Water on Rheology



Mei & Kohlstedt (2000a,b)  
 Karato and Jung (2003)  
 Hirth and Kohlstedt (2003)  
 Kohlstedt (2006)  
 Karato (2008)  
 Kohlstedt (2009)  
 Karato (2015)



# Effect of Water on Rheology



- Motion of dislocation planes + climb/jog
- Climb is facilitated by diffusion
- Diffusion
  - frequency of jumps/  
probability of finding a defect
  - the defect concentrations

Mei & Kohlstedt (2000a,b)  
Karato and Jung (2003)  
Hirth and Kohlstedt (2003)  
Kohlstedt (2006)  
Karato (2008)  
Kohlstedt (2009)  
Karato (2015)

# Electrical Conductivity

- Low electrical conductivity at asthenosphere
- Is this due to melting?
- Melt + basalt experiments: melt does not wet the grains.
- Dry electrical conductivity of olivine will require temperatures higher than what is expected.
- Hydrogen diffusion is fast
- Could hydrogen diffusion, i.e., motion of ionic charge (electrical conductivity) explain high EC?

*Karato (1990)*

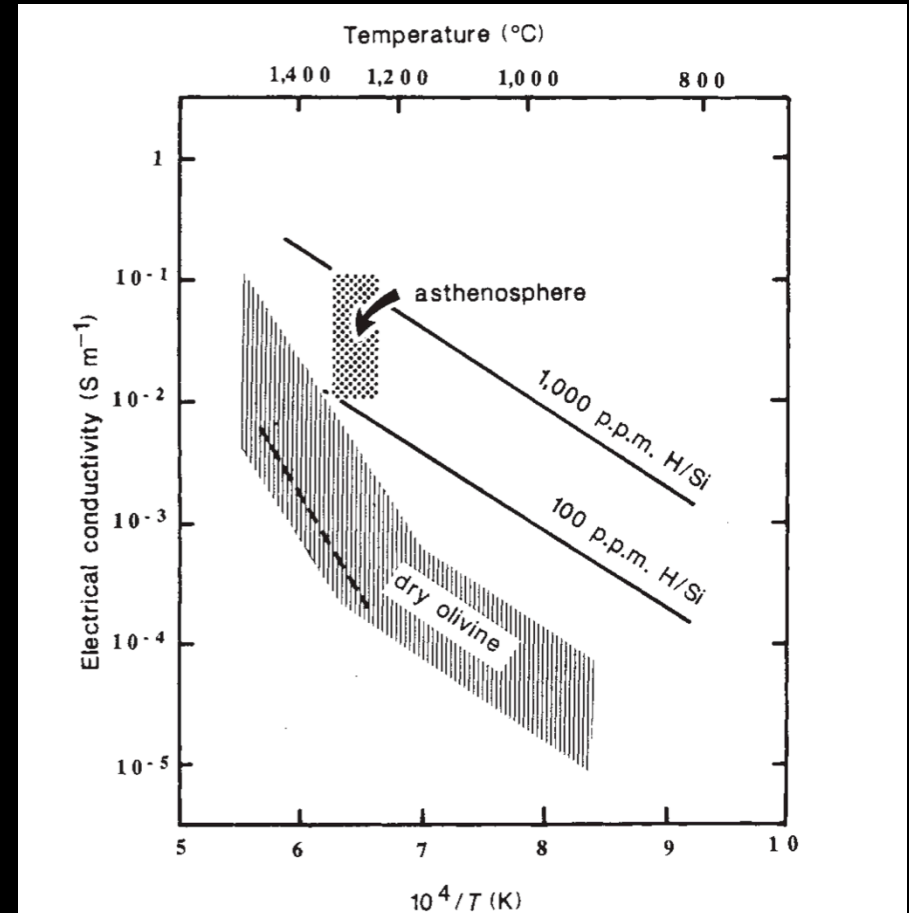
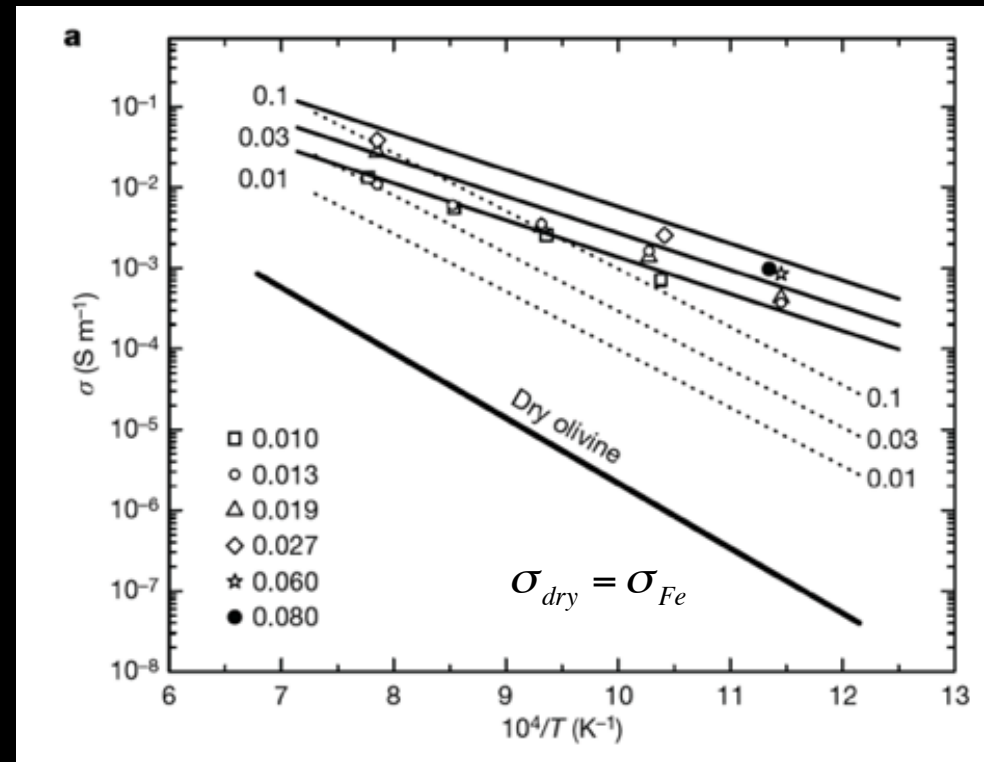


FIG. 1 Electrical conductivity in olivine as a function of temperature and hydrogen content. Data for dry olivine correspond to the hatched region<sup>1,8</sup>. The dashed line shows the electrical conductivity calculated from the diffusion coefficients of  $\text{Mg}^{2+}$  (or  $\text{Fe}^{2+}$ ) under dry conditions. Solid lines show the electrical conductivity calculated from experimental<sup>7</sup> diffusivity of hydrogen. The dotted region indicates the range of conductivity estimated from geomagnetic soundings and the estimated temperature of the asthenosphere. This region coincides with the estimated conductivity for a hydrogen content of  $\sim 200$ – $2,000$  p.p.m. H/Si.

# Electrical Conductivity

- Low electrical conductivity at asthenosphere
- Is this due to melting?
- Melt + basalt experiments: melt does not wet the grains.
- Dry electrical conductivity of olivine will require temperatures higher than what is expected.
- Hydrogen diffusion is fast
- Could hydrogen diffusion, i.e., motion of ionic charge (electrical conductivity) explain high EC?



$$\sigma_H = AC_{\text{H}_2\text{O}}^r \exp\left(-\frac{H}{RT}\right)$$

# Electrical Conductivity

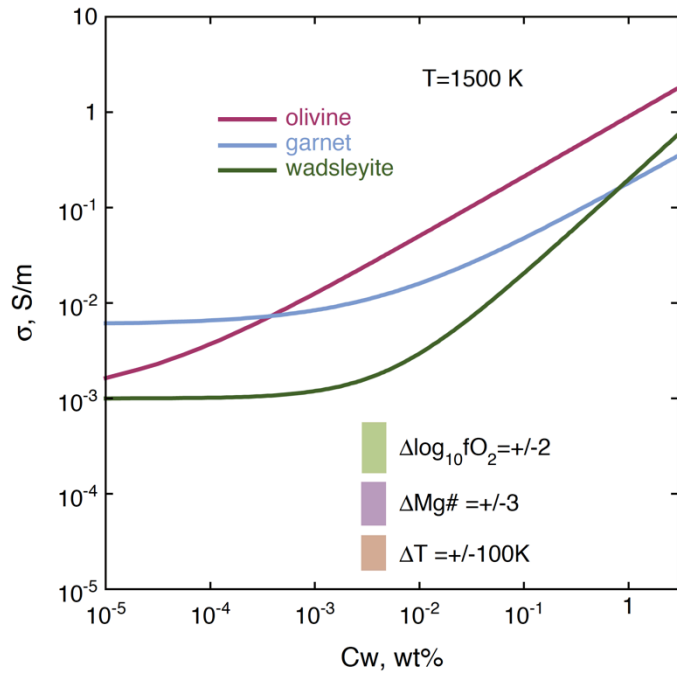
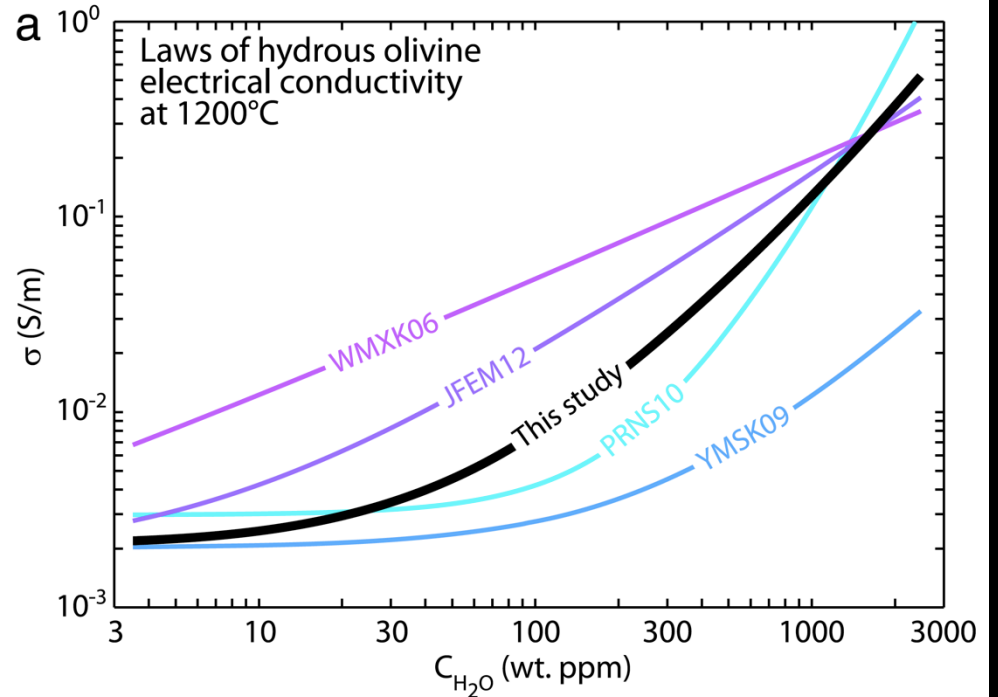


**Fig. 2.** Influence of water content ( $C_w$ ) on electrical conductivity ( $\sigma$ ) at 1500 K in olivine (4 GPa), garnet (4 GPa), and wadsleyite (15 GPa) at  $f_{O_2}$  (oxygen fugacity) corresponding to the Mo–MoO<sub>2</sub> buffer (data see Table 2). Shown together are the influence of other factors including the variation in temperature (T), Mg# and  $f_{O_2}$  (the height of each bar corresponds to the influence of each factor). The influence of mineralogy, such as pyrolite versus harzburgite can also be estimated from this figure.



$$\sigma = A_1 \cdot f_{O_2}^{q_1}(P, T) \cdot \exp\left(-\frac{H_1^*}{RT}\right) + A_2 \cdot f_{O_2}^{q_2}(P, T) \cdot C_w^r \cdot \exp\left(-\frac{H_2^*(C_w)}{RT}\right)$$

Garde (2014)

Karato (2011)

# Electrical Conductivity: Water in Deep Earth

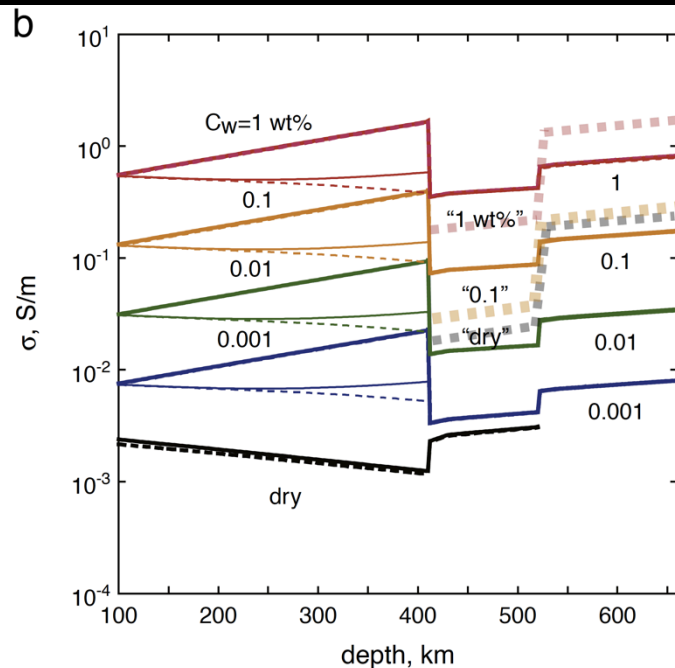


**Fig. 3.** (a) Temperature–depth profile used in the calculation of conductivity–depth profile (Ito and Katsura, 1989). (b) Electrical conductivity ( $\sigma$ ) versus depth relationships for the upper mantle and the MTZ calculated for the pyrolite mantle model with various water contents. Solid lines correspond to the Hashin–Shtrikman upper bounds, and broken lines to the lower bound (differences are small in most cases). Thick lines are for models without pressure effects for “wet” olivine, thin lines are for the model with pressure effects. For comparison, results from Yoshino’s group for the MTZ are also shown by thick broken half-tone curves (Yoshino, 2010). These are based on low, one-frequency measurements and the “dry” samples in these studies contain substantial amounts of water ( $\sim 0.01$  wt.% or higher). No data for pyrope nor orthopyroxene was published from Yoshino’s group, and therefore results for the upper mantle from their lab are not shown. For the data source see Tables 2 and 3, and the details of method of calculation of conductivity–profiles are given in Supplemental Material 2.

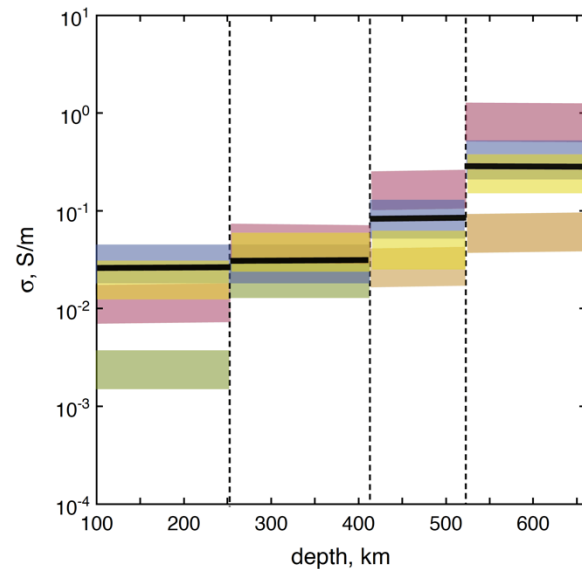


**Fig. 4.** Geophysically inferred conductivity ( $\sigma$ )–depth profiles. A piece-wise conductivity model is used. An “average” model shows a small increase in conductivity in the upper mantle followed by an increase in conductivity in MTZ. A constant water content model shown in Figure 3 is not consistent with this observation. In order to explain the increase in conductivity at 410-km discontinuity, an increase in water content at this depth is necessary. An “average model” can be attributed to  $\sim 0.01$  wt.% water in the upper mantle and  $\sim 0.1$  wt.% in the MTZ. However, a large lateral (regional) variation in conductivity is also observed suggesting a large regional variation in water content. For the data source see Table 4.

Karato (2011)

Early Earth:  $H_2$  solubility

# Hydrogen in Minerals (Reduced $fO_2$ )

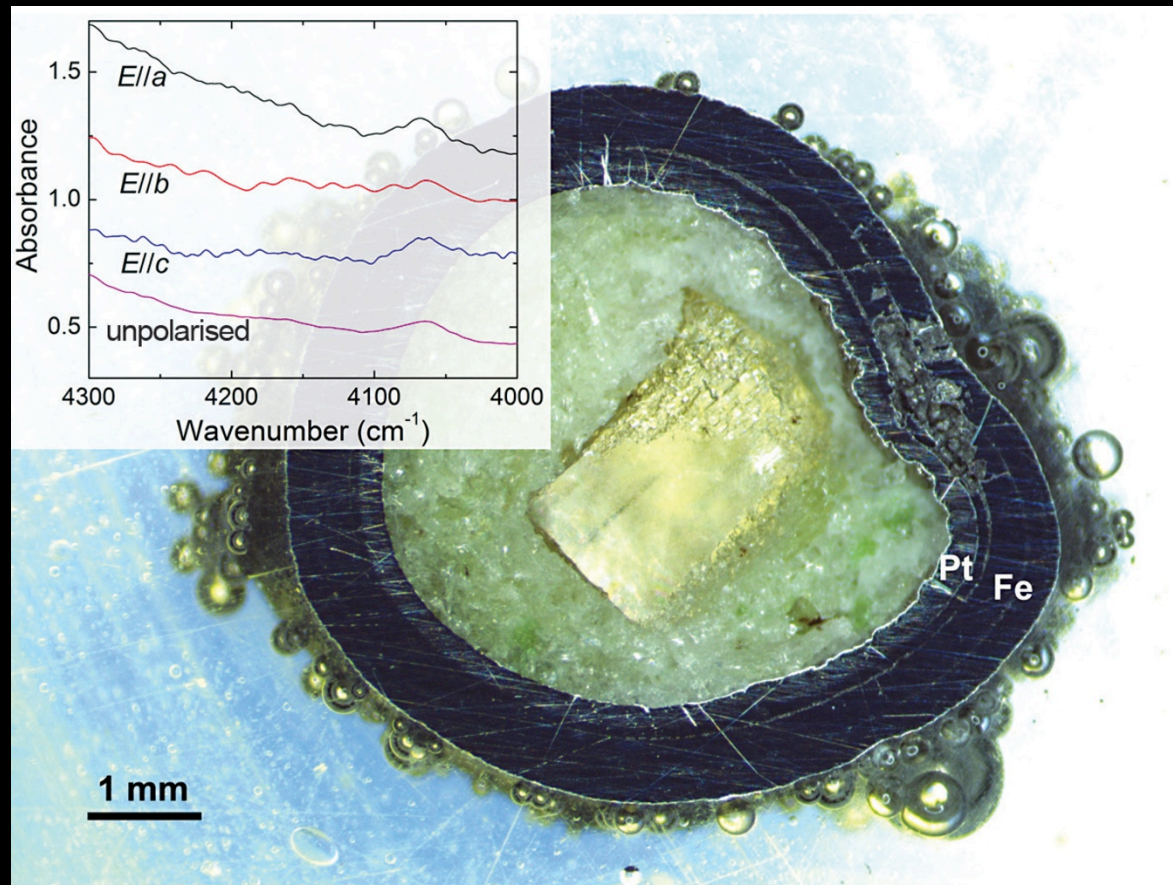


**Figure 1** Recovered orthopyroxene crystal annealed at 2 GPa and 1100 °C and polarised and unpolarised FTIR spectra of the crystal containing molecular H<sub>2</sub>. The spectra were normalised to 1 cm thickness and vertically offset. The crystal was surrounded by fine powder of a spinel peridotite of broadly equilibrium composition (e.g., with similar composition between the crystal and orthopyroxene in the peridotite). The capsule was embedded in epoxy resin, and the crystal remained nearly intact after the run.

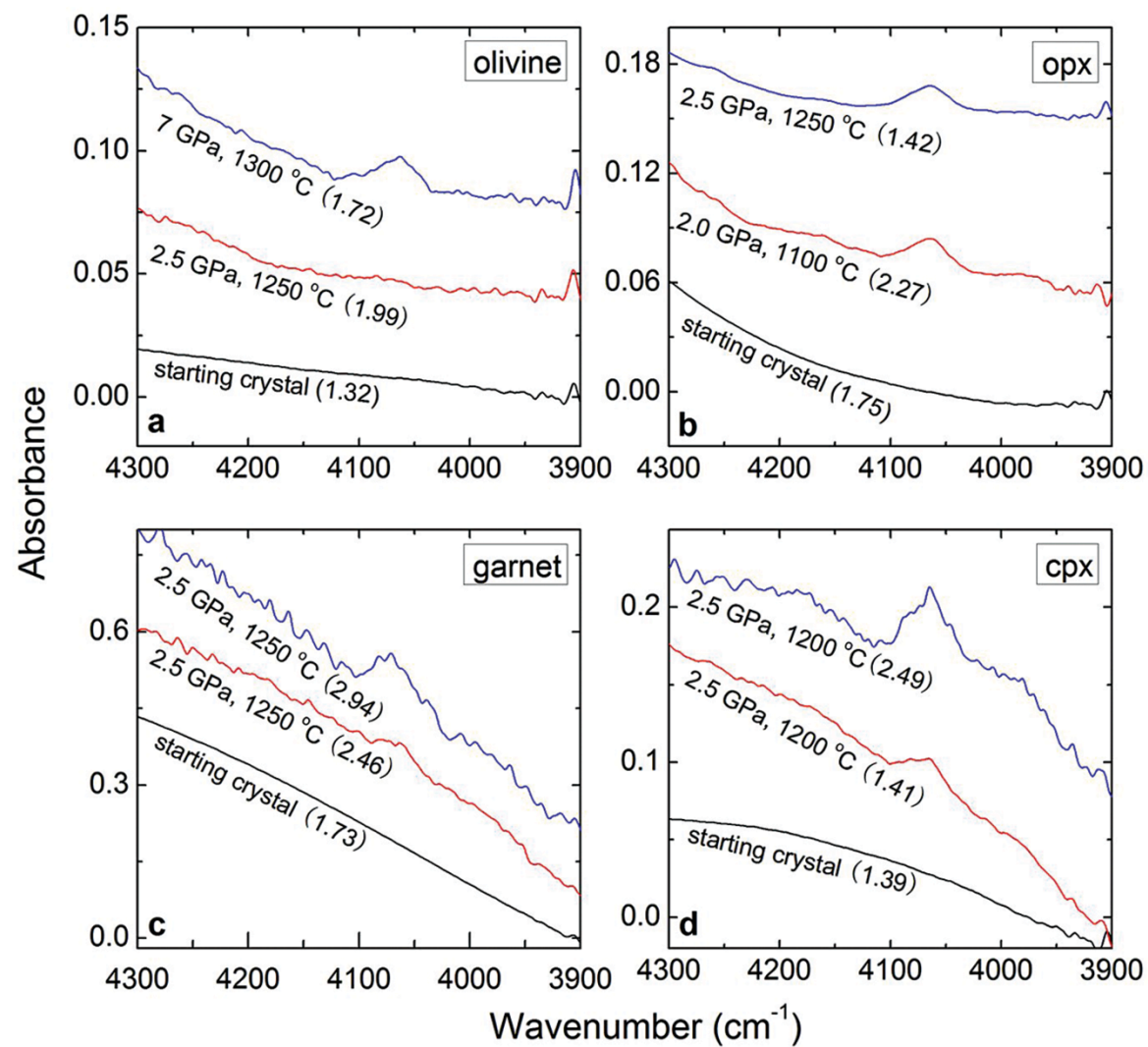
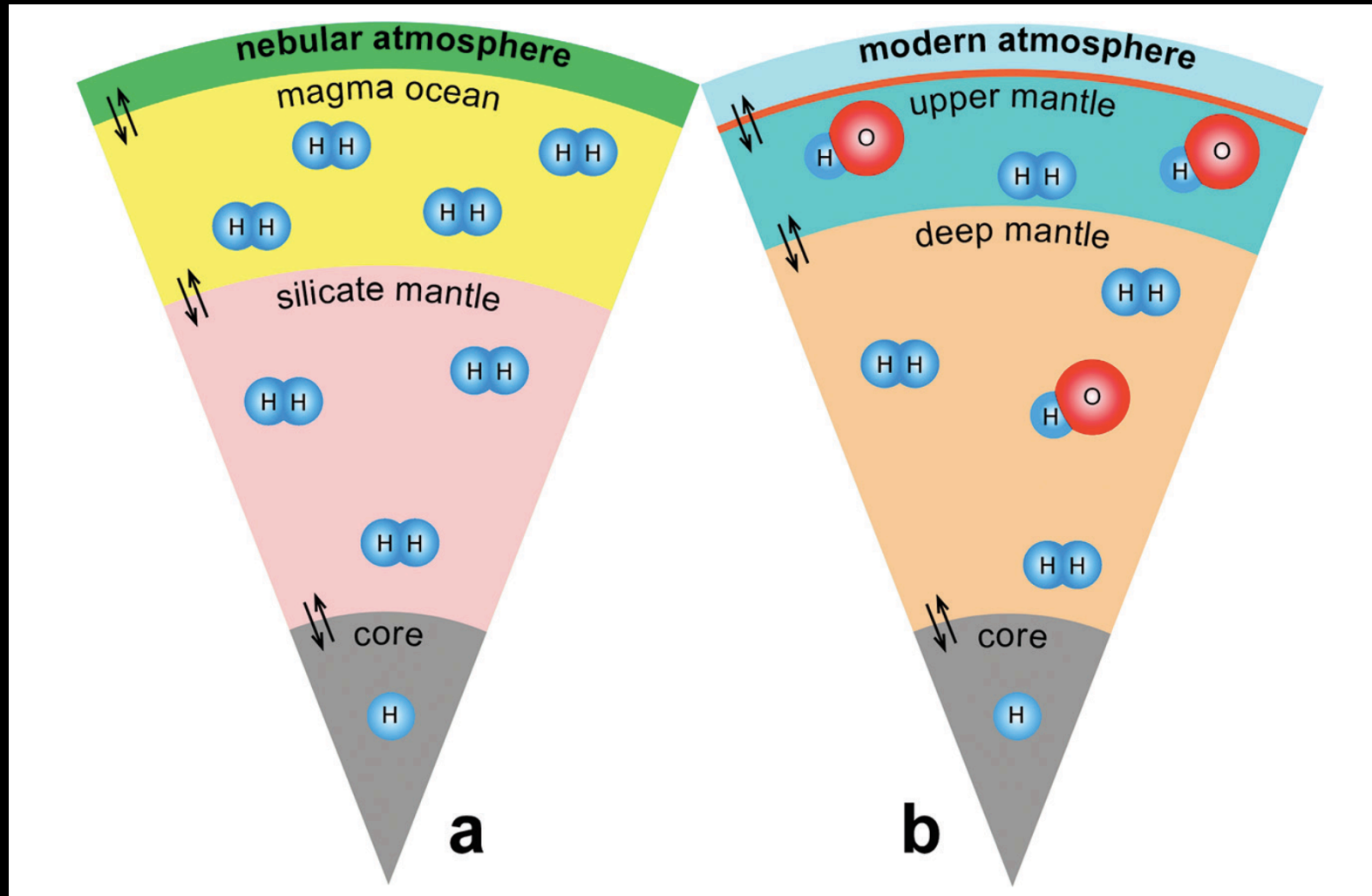


**Figure 2** Unpolarised FTIR spectra of (a) olivine, (b) orthopyroxene, (c) garnet, and (d) clinopyroxene containing dissolved molecular H<sub>2</sub>. Experimental conditions are given below each spectrum; numbers in parentheses are the thickness (mm) of the polished crystal. The spectra were not normalised to constant thickness, but vertically offset. The two spectra for either the annealed (c) garnet or (d) clinopyroxene were measured on the same recovered crystal after polishing to different thickness.

# Molecular H<sub>2</sub> vs OH



Yang et al. (2016)

# Summary

1. Natural Observations
2. Thermodynamic Model
3. Water Solubility Experiments
4. Physical Properties

Effect of water on velocity & sharpness (not that sensitive)

Effect of water on transport properties-

(exponential with defect concentration i.e., fugacity terms)